University of New Mexico
UNM Digital Repository

Mechanical Engineering ETDs | Engineering ETDs

2-1-2016

THEORY, FABRICATION, AND EXPERIMENTATION OF PHONONIC CRYSTALS IN MEMS AT MICRO/NANO SCALE: ENGINEERING OF THERMAL AND RF PHONONS TO APPLICATIONS IN THERMOELECTRICS AND MICRORESONATORS

Seyedhamidreza Alaie

Follow this and additional works at: https://digitalrepository.unm.edu/me_etds

 Part of the Mechanical Engineering Commons

Recommended Citation
Alaie, Seyedhamidreza. "THEORY, FABRICATION, AND EXPERIMENTATION OF PHONONIC CRYSTALS IN MEMS AT MICRO/NANO SCALE: ENGINEERING OF THERMAL AND RF PHONONS TO APPLICATIONS IN THERMOELECTRICS AND MICRORESONATORS." (2016). https://digitalrepository.unm.edu/me_etds/24

This Dissertation is brought to you for free and open access by the Engineering ETDs at UNM Digital Repository. It has been accepted for inclusion in Mechanical Engineering ETDs by an authorized administrator of UNM Digital Repository. For more information, please contact disc@unm.edu.

Seyedhamidreza Alaie
Candidate

Mechanical Engineering
Department

This dissertation is approved, and it is acceptable in quality and form for publication:

Approved by the Dissertation Committee:

Proferssor Zayd C. Leseman , Chairperson

Professor Yu-Lin Shen

Professor Mansoor Sheik-Bahae

Professor Payman Zarkesh-Ha

THEORY, FABRICATION, AND EXPERIMENTATION OF PHONONIC CRYSTALS IN MEMS AT MICRO/NANO SCALE
:
ENGINEERING OF THERMAL AND RF PHONONS TO APPLICATIONS IN THERMOELECTRICS AND MICRORESONATORS

by

SEYEDHAMIDREZA ALAIE

B.S., Mechanical Engineering, University of Tehran, 2004
M.S., Mechanical Engineering, University of Tarbiat Modares, 2007
M.S., Optical Science and Engineering, University of New Mexico, 2014

DISSERTATION

Submitted in Partial Fulfillment of the
Requirements for the Degree of

Doctor of Philosophy

Engineering

The University of New Mexico
Albuquerque, New Mexico

Dec 2015

Dedicated to my parents and siblings to whom I owe my sole life, because of their lifelong support and **unconditional love**.

Dedicated to the memory of Rene Descartes and Bertrand Russel through enlightening words of whom I have my **perception of life**.

Dedicated to my loyal friends from whom I learned how to be hardworking, and **self-esteemed** in life.

And

Dedicated to the dear one because of generosity of whom I realized the meaning of **love**, kindness, and beauties of moonlight.

ACKNOWLEDGMENTS

I heartily acknowledge Professor Leseman, my advisor and dissertation chair, for his trust in me, his support for my research, and instructing me how to learn. His guidance and professional style will remain with me as I continue my career.

I wish to thank Dr. Ihab El-Kadi, and Prof. Mani Hossein-Zadeh for their guidance and invaluable role in promotion of my research carrier.

I also thank Dr. Charles C. Reinke, Dr. Drew F. Goettler, Dr. Khawar Abbas, and Mr. Alireza Kazemi for their contributions to my research.

To Professor Arsalan Razani, and David H. Dunlap, thank you for your devotion to teaching me. I also appreciate the help of my coworkers Dr. Arash K. Mousavi, M. G. Baboli, Mirza M. Mahbube Elahi, Adnan Raza, and Mohammad R. Zamani in our research group.

To Ying-Bing I highly appreciate your help at the TEM Laboratory.

Thank you my friends Dr. Mohsen Daghooghi and Prof. Tehrani, I was truly gifted with your advice and support.

Last but not least, I wish to thank Dr. Sheikh Bahae, Zarkesh-Ha and Shen my dissertation committee members for their advice.

THEORY, FABRICATION, AND EXPERIMENTATION OF PHONONIC CRYSTALS IN MEMS AT MICRO/NANO SCALE:

ENGINEERING OF THERMAL AND RF PHONONS TO APPLICATIONS IN THERMOELECTRICS AND MICRORESONATORS

by

Seyedhamidreza Alaie

B.S., Mechanical Engineering, University of Tehran, 2004
M.S., Mechanical Engineering, University of Tarbiat Modares, 2007
M.S., Optical Science and Engineering, University of New Mexico, 2014

ABSTRACT

Phononic Crystals (PnCs) are novel materials comprised of a periodic structure of inclusions in a matrix. This periodic arrangement creates phononic bandgaps, and modifies phononic bandstructures of a material. Such a property offers promising applications at the micro and nano scales to engineer acoustic filters, high Q-factor resonators, and thermoelectric properties of materials. Studying PnCs at the micro/nano scale requires specific characterization techniques, which rely on Micro Electro Mechanical Structures (MEMS). This work focuses on the study, and characterization of PnCs using MEMS in view of their prospective applications in thermoelectric materials, microresonators and acoustic filters, and also the prospective applications of PnCs in MEMS.

Table of Contents

List of Figures

List of Tables

1 Introduction

1-1 Phononic Crystals

Phononic Crystals (PnCs) are novel materials comprised of a periodic structure of inclusions in a matrix. This periodic arrangement creates acoustic bandgaps in the elastic wave response of the PnC [1, 2]. During the last decade, PnCs have attracted much attention due to their promising applications in filtering elastic waves and as waveguides [3-9]. More recently their applications in manipulation of thermal conductivity at the micro-scale have investigated [10-13]. Phononic crystals are typically comprised of a matrix and embedded periodic inclusions. Fig. 1—1 shows different PnCs with air, Pt and Pt/air inclusions. In this work the phononic crystals with different applications are studied in different scales from hundreds of microns to sub microns.

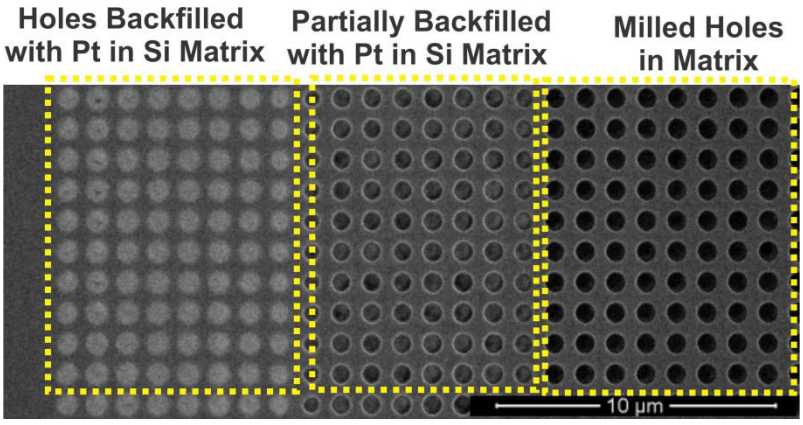

Figure 1—1: PnCs made from Si matrix with Pt, Pt/air, or air inclusions.

1-2 Acoustic Properties of Phononic Crystals

One of the interesting features of the PnCs is their acoustic bandgap [3, 8, 14, 15]. An acoustic bandgap defines a certain range of frequencies at which elastic wave propagation is forbidden. This property relates to the lattice of the PnCs, the acoustic impedance mismatch between the inclusions and matric, and filling fraction [5]. Such an interesting property technologically contributes to fabrication of high quality factor resonators [16], filters, and waveguides [5, 6] in a very confined space. In Fig. 1—2, a typical bandgap of a PnC is depicted. This plot shows the measured transmission of acoustic waves from transmitter on the left to the receiver on the right (See also Fig. 1—3). It also shows the simulations of transmission spectra using different methods such as Finite Element Analysis (FEA)[15], and Finite Domain Time Domain (FTDT) [8]. In a typical measurement device, both the receiver and transmitter comprise a set of Inter-digitated fingers, which converts acoustic energy to the electrical energy and vice versa. The PnC is located between the two sets of the Inter-digitated fingers and depending on the frequency of the waves the transmission of energy changes [8, 14, 15]. In Fig. 1—2, some regions are shown, which feature a very low transmission, *e.g.* less than -10 dB of transmission. This range of frequency is called the acoustic bandgap. The acoustic bandgap can be observed by studying the acoustic dispersion diagram of the PnC. Fig. 1—3 shows the acoustic dispersion in a typical PnC. It describes the normalized frequency of waves versus the wave vector. It is evident that for some certain

frequencies there is no solution for the acoustic wave propagation. This property combining with piezo-electric materials can be employed to fabricate new class of RF devices [4, 5]. Another application is achieving very high quality factor resonators [16].

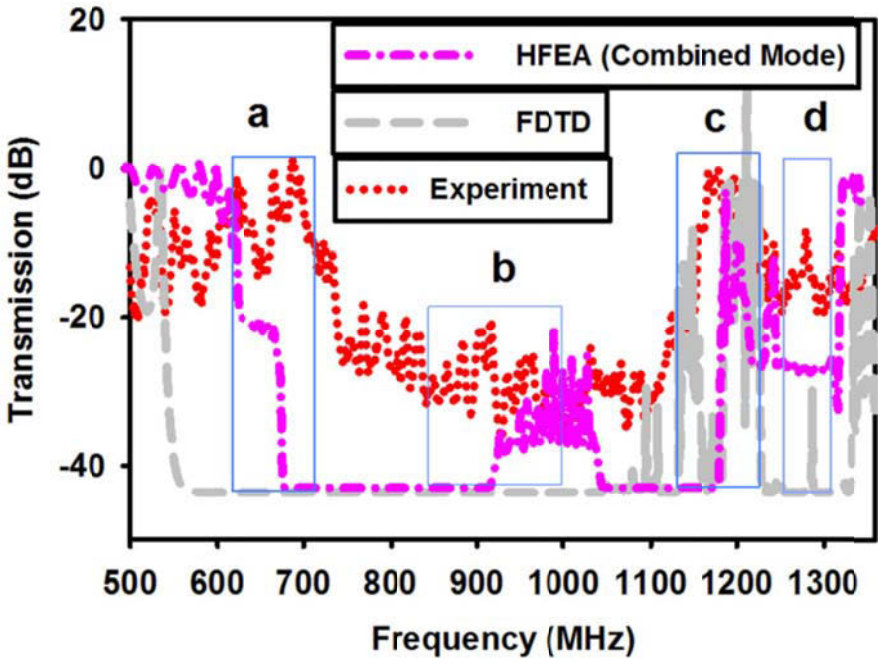

Figure 1—2: A typical measured bandgap is simulated by FEM and FTDT. Boxes a, b, c, and d show different regions of bandgap beginning, middle of bandgap end of the bandgap and the middle of the secondary bandgap respectively. The figure is reproduced with permission from Ref. [15]. © 2013 AIP Publishing LLC.

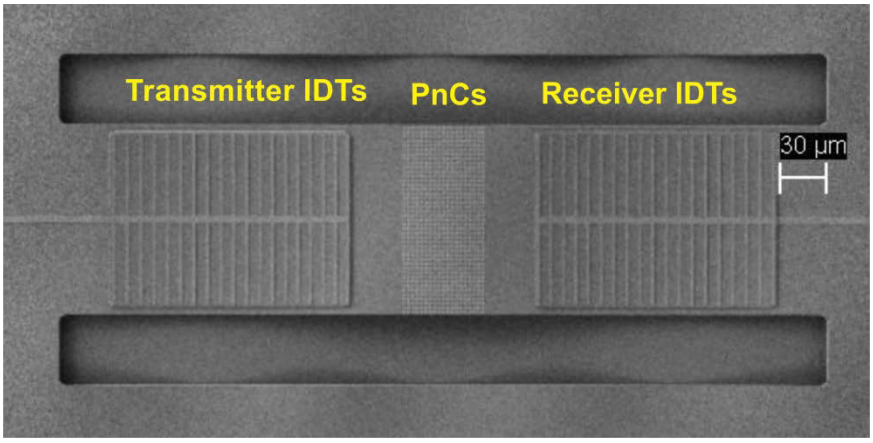

Figure 1—3: A typical MEMS device for measurement of PnCs transmission. The figure is reproduced with permission from Ref. [15]. ©2013 AIP Publishing LLC.

1-3 Phononic Band Structure and Thermal conductivity

Phononic crystals at nano-scale can manipulate the phononic dispersion [11, 17]. Here the term phonon refers to the quantized vibrational mechanical waves propagated in matter. When the wavelength corresponding to these waves is in order of several microns, the term acoustic is preferred, while the term phonons is more common when the wavelength of mechanical waves is in order of nm. At nano-scale the lattice and type of atoms define phononic bad structure. The dispersion is related to the thermal conductivity of matter according to Callaway Holland formulation [17, 18]:

$$\kappa = \frac{1}{6\pi^2}\sum_j \int_q \frac{\hbar^2 \omega_j^2(q)}{k_B T^2} \frac{\exp\left[\frac{\hbar\omega_j(q)}{k_B T}\right]}{\left(\exp\left[\frac{\hbar\omega_j(q)}{k_B T}\right]-1\right)^2} v_j^2(q)\tau_j(q)q^2 dq \qquad (1-1)$$

where $\hbar$ is the reduced Planck constant, $\omega(q)$ is the phonon dispersion, k_B is the Boltzmann constant, T is the phonon temperature, $v(q) = \partial\omega(q)/\partial q$ is the phonon group velocity, $\tau(q)$ is the scattering lifetime of the phonons, q is the wave vector, and the summation is over all phonon modes. Since possibly phononic crystals can change the band structure materials based upon Eq. (1-1) it is possible to change the thermal conductivity of matter by engineering of PnCs [13, 17]. Even though, successful engineering of thermal conductivity at atomic level using PnCs have been realized [19], similar physics for change in thermal conductivity at higher scales have not been proven yet . Larger sub-micron PnCs requires much larger numerical space for simulation, which is very challenging at this point. Moreover, if submicron PnCs are employed to engineer the band structure the periodicity of a supper lattice will become submicron as well. This introduces more complicated parameters such as coherence lengths of phonons that need to be considered numerically. Engineering of thermal conductivity of PnCs has applications in engineering of thermoelectric materials, where manipulation of thermal conductivity without changing the electrical conductivity is desired. Recently the challenge with calculation of bandstructures suitable for Eq (1-1) was met [17].

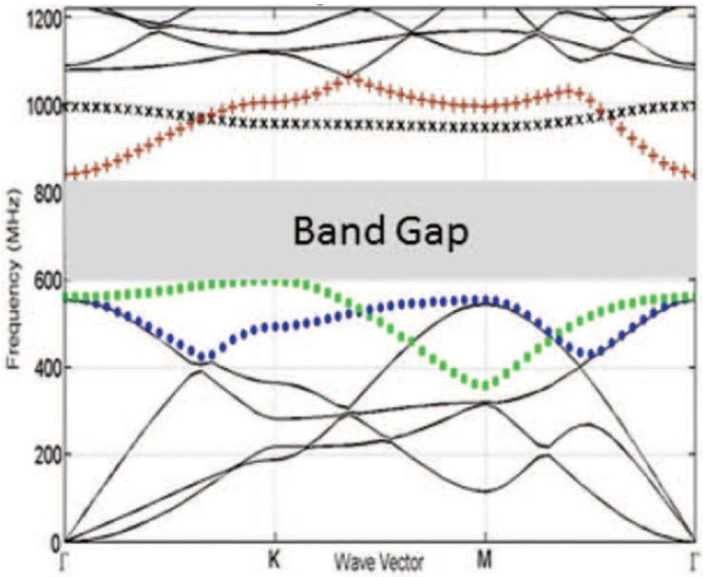

Figure 1—4: A typical band structure of PnC with a bandgap. The figure is reproduced with permission from another report [20].

1-4 Applications in Oscillators

Phononic Crystals can feature very high reflectance of acoustic waves using only 3 to 5 periods [16]. Accordingly, they are very promising for fabrication of high quality oscillators. They have also applications in enhancing the mechanical quality factor of cavities. Such an application of these structures has been numerically [21-23] and experimentally verified [16, 23, 24]. In particular, they are promising to enhance the mechanical Q-factor of Opto-mechanical resonators [25]. Figs. 1—5 a, b show such a resonator.

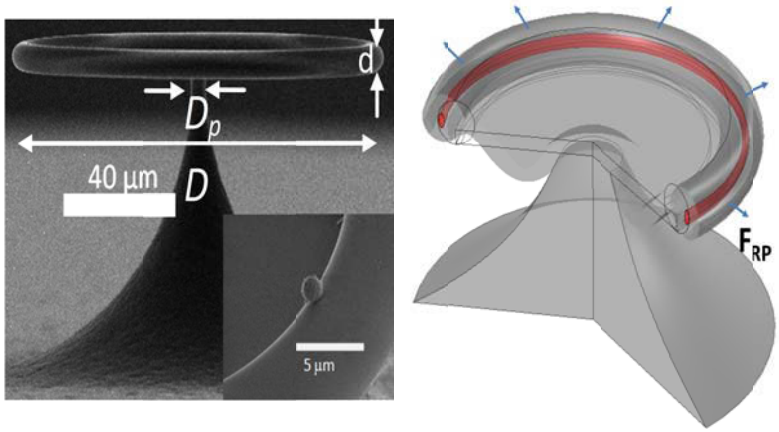

(a) (b)

Figure 1—5: (a) SEM image of a silica microtoroid. (b) Schematic diagram showing the cross–section of a microtoroid, and mechanical deformation of the silica membrane. The figure is reproduced with permission from another report [26]. © 2013 OSA.

1-5 Characterization

Characterization of PnC is achieved by Electromechanically Structures (MEMS). Such devices offer very sensitive characterization of force [27, 28], stiction [29], mass [25], acoustic waves [6], or temperature [30]. Transmission of mechanical waves is performed using piezo-electric transducers at lower frequencies [6, 8, 9]. Currently the operating frequency of piezo-materials is limited to below 10 GHz and direct characterization at higher frequencies is not possible using the current technology. However, the phonons responsible for heat transfer are mostly at THz frequency at room temperature. Accordingly, for thermal applications direct measurement of the phononic transmission is not possible currently. However one can measure the thermal conductivity of PnCs

[13, 31, 32], and indirectly study the effects of PnCs on the band structure of matter and their relationship with thermal conductivity.

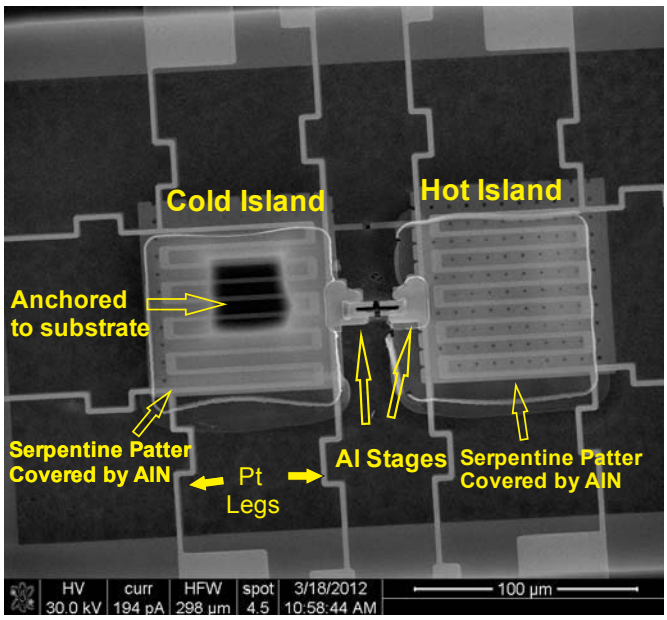

Figure 1—6: A MEMS device fabricated for characterization of thermal conductivity of micro samples. The figure is reproduced with permission from another report [30].© 2013 IOP Publishing Ltd.

1-6 Objectives of This Work

Fabrication of Phononic Crystals

Study of fabrication of phononic crystals at different scales with different methods is intended. The goal is fabrication of PnCs on Si thin films. Focused Ion Beam (FIB), and optical lithography are

employed to fabricate the PnCs at submicron and micron scale. Each technique is ideal for a certain scale. In photolithography, a photo-resist is patterned and used as a mask for etching PnCs using RIE process. To fabricate PnCs using FIB a titanium layer is used as a mask for etching Si with FIB. The phononic crystals fabricated here are to be characterized thermally to study the coherent scattering of phonons in PnCs.

Characterization and Engineering of PnC Band-Gap

Study of acoustic band gap of PnCs is aimed by Harmonic Finite Element Analysis (HFEA) to understand the experimental results for the transmission of PnCs. The goal is developing both experimental (See Fig. 1—3) and theoretical capability to employ PnCs for RF applications. In particular, acoustic transmission of PnCs is to be studied in harmonic domain using ANSYS. Different boundary conditions are employed to predict the acoustic bandgap as accurately as possible (See Fig. 1—2).

Thermal Characterization of Micro/Nano Samples using MEMS

Thermal conductivity of thin films is to characterize using a noel MEMS device. In the first stage, the results are verified using unknown samples. A typical MEMS device is shown in Fig 1—5. Such a device comprises of two Pt patterns, which measure the temperatures and apply heat. In addition, a sample is mounted between the two sensors. Using this setup, one measures thermal conductivity of

micro/nano samples [30]. After verification of the technique, it can be extended for the measurement of Seebeck Coefficient and electrical resistance of samples for a full ZT characterization.

Characterization and Understanding of Coherent Scattering of Phonons at Room Temperature

Using a MEMS device, thermal conductivity of Silicon Phononic Crystals with different lattices (See Fig. 1—6) is to be measured. Using the measured values the thermal conductivity is revisited by Eq. (1-1). The comparison shows the strength of coherent scattering of phonons at room temperature. Different super cells have the same critical dimensions, and very close porosity. However, the super cell sizes are different and the change in thermal conductivities can be studied to assess existence of a coherent effect of phonons' scattering.

2 Fabrication of PnCs

All the materials in this chapter are reproduced with permission from another report [33]. This chapter is a modified version of the supplementary information of that article. © 2015 Mcmillan Publishers Limited. For more details, the readers are encouraged to refer to other reports [10, 33, 34].

2-1 FIB

The phononic crystals (PnCs) in this work are by focused ion beam (FIB) milling using gallium ions (Ga^+). To protect the samples from Ga contamination during fabrication, a process utilizing a sacrificial layer was developed [11]. Fig. 2—1 depicts the process as used in this work. This process starts with a silicon-on-insulator (SOI) wafer, which is covered with a 100nm sacrificial layer of titanium; after milling the samples, the sacrificial layer is removed and the device is released. The titanium film serves two functions: (1) to protect of the Si from Ga contamination hitting the sample on the top [11], and (2) ensuring vertical sidewalls for the PnC holes. Ti has a lower sputtering yield than Si, thus the Ti deposited on top of the Si creates a barrier through which nearly vertical sidewalls can be created in Si [10, 33], which shows the sidewalls of PnCs after milling. After patterning the PnC with FIB, the sample is immersed in a buffered hydrofluoric acid (BHF) solution for 4 minutes to remove the Ti [35] and also partially etch the silicon dioxide layer. This process also removes the amorphous silicon layer [36] formed on the sidewalls of the PnC holes from the milling by FIB [37]. After fully removing the Ti sacrificial layer by wet etching, the PnC is fully released by vapor-phase hydrofluoric acid (HF). The vapor HF etch removes the buried

oxide (BOX) layer under the PnCs, which minimizes the possibility of stiction failure [38, 39] of the samples.

Even though the surface of Si is completely protected by the Ti layer, milling through the Si by FIB or any other etching method will result in an amorphous layer of Si (a-Si) combined with elements of the plasma utilized on the sidewalls. For the Ga^+ FIB process, it was previously reported that a layer of a-Si with a thickness from 13nm [40] to 24nm [41] may exist in the via after milling. The lateral spread of Ga into the a-Si can be as much as 6.3nm, indicating that the Ga is contained within the a-Si. However, the PnC samples are processed in a buffered HF solution after FIB milling, which etches the native oxide on the surface of the Si as well as the a-Si silicon layer [42]. According to previous reports [42], such etching leaves the top surface with very low concentrations of O, C, and F. After releasing the PnCs, an Energy Dispersion Spectroscopy (EDS) analysis was performed at various energy levels in the PnC vias that showed the same elements as the previous reports (Fig. 2—2). In this figure, the O signal is the strongest, and smaller amounts of F, Ga, and C are also present. Based on the process flow and EDS analysis, it is clear that a native layer of oxide is present in addition to a trace amount of F, C, and Ga. All of these trace elements are confined to the interior surfaces of the PnC vias.

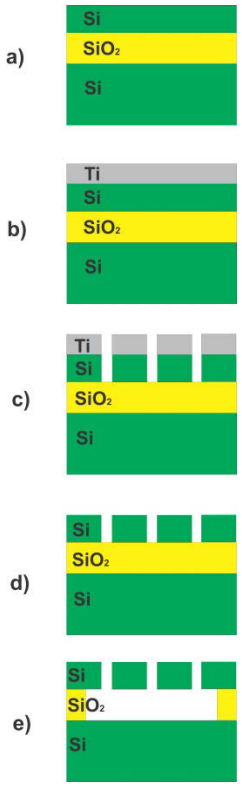

Figure 2—1: a) the SOI wafer, b) a sacrificial layer of titanium is sputtered, c) the PnC is patterned by FIB, d) the Ti film is etched by BHF, e) the PnC is released in vapor HF. The figure is reproduced with permission from another report. This figure is reproduced with permission from another report[33]. © 2015 Mcmillan Publishers Limited.

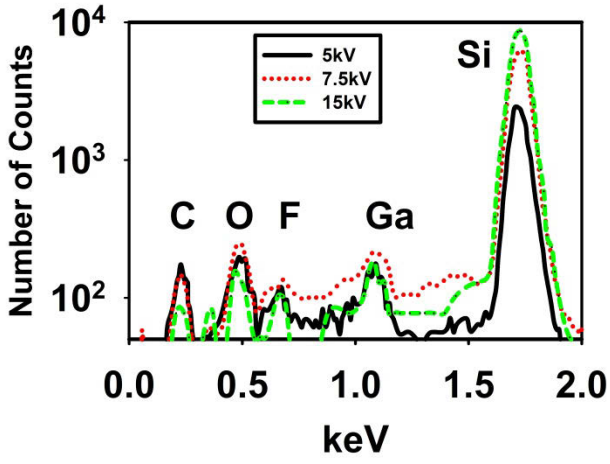

Figure 2—2: EDS analysis of the freestanding PnCs after fabrication at 3 different energy levels indicating small amounts of F, Ga, O, and C This figure is reproduced with permission from supplementary information of another report[33]. © 2015 Mcmillan Publishers Limited.

2-2 Sidewall Characterization

The roughness of sidewalls is an important parameter because they determine diffuse or specular scattering of phonons from boundaries. To characterize the sidewall roughness of the PnC holes, the transmission electron microscopy (TEM) technique was used. The fabrication process is illustrated in Fig. 2—3. Initially, a thin layer of Ti is sputtered on an SOI wafer. As shown in Fig. 2—3.3, the array of PnC air holes is patterned with FIB. An amorphous layer of Si several nanometer thick forms on the sidewall surfaces. In the actual process of fabricating these PnCs, this layer is etched in BHF. However, to preserve this layer for use in the roughness study via image contrast between Si and a-Si, a second layer of Ti, Ti(2) is deposited (Figure 2—3.4) to avoid its alteration during the TEM sample preparation. Next, several microns of Pt are deposited (Fig. 2—3.5) to protect the sample during the lift-off process [43]. After extraction, the sample is mounted on a TEM grid and the areas of interest are thinned down to between 20nm and 40nm, as shown in Fig. 2—4.6. At this stage, a very thin sample is ready for a TEM study, where the interface between Si and a-Si is of interest. This interface has been protected with Ti and Pt on the right, Si on the left, and Ti and Pt from the top. The cross-section of the TEM sample has been also milled with 1.5 pA, which is the lowest current/damage possible. Therefore, this process is designed to study only the original form of the roughness imposed the PnC fabrication rather than the damage due to the TEM sample processing.

The process of TEM sample preparation is shown in Fig. 2—4. Initially the SOI wafer is patterned by FIB and covered by Pt after the sputtering of Ti, as shown in Fig. 2—4.1. To extract the TEM sample, all the areas around the protected holes are milled using FIB (see Fig. 2—4.2), and the sample is mounted on a TEM grid (Fig. 2—4.3). After attaching the sample to the TEM grid, a row of PnC holes are thinned (Fig. 2—4.4) and the thinnest areas were studied by TEM. Prior to the TEM study, a diffraction pattern was observed for the Si to ensure that the thinning process did not damage its crystalline structure. EDS analyses were also performed on the different layers: Si, a-Si, Ti, and Pt, which confirmed the composition.

Bright field contrast images were then obtained for the interfaces. Two sidewalls of a thinned down sample are shown in Supplementary Figure 2—5. Here, the amorphous Si contains a high amount of Ga, which looks darker than Si. The maximum roughness step height was observed to be about 2.6nm. The RMS roughness (defined as root mean square of the deviation from average height) was found to be ~1 nm. This roughness is in agreement with another report demonstrated an RMS roughness about 1.6 nm [44] on Si sidewalls after FIB patterning under the condition of a higher current over larger area which is more unfavorable for a smooth surface .

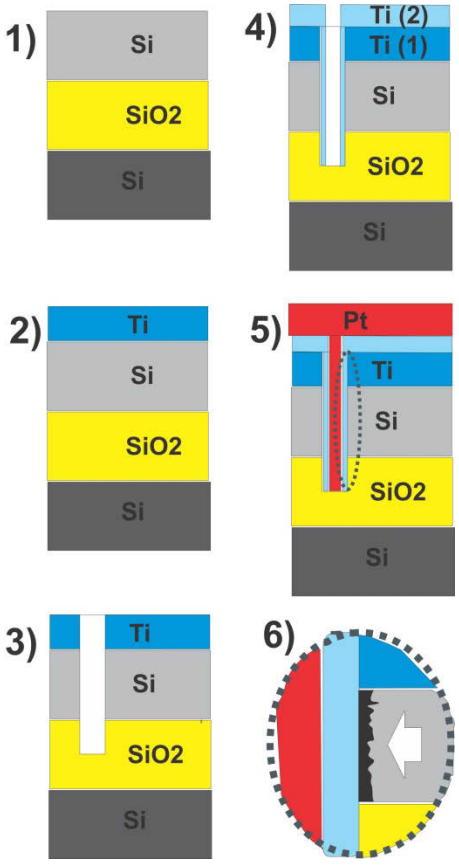

Figure 2—3: The processing flow used for charecterization of vertical side walls of the pores shown as : 1) Cross-section of an SOI wafer, 2) deposition of a protective layer of Ti, 3) milling PnCs with FIB, 4) a second Ti layer for preserving the sidewalles (to be charecterized) in the process of TEM sample preparation, 5) deposition of Pt by e-beam and FIB for preparing a TEM lamela, 6) thinning the sample and charecterization of sidewalls in a TEM by observing the interfaces of the different materials. This figure is reproduced with permission from supplementary information of another report[33]. © 2015 Mcmillan Publishers Limited.

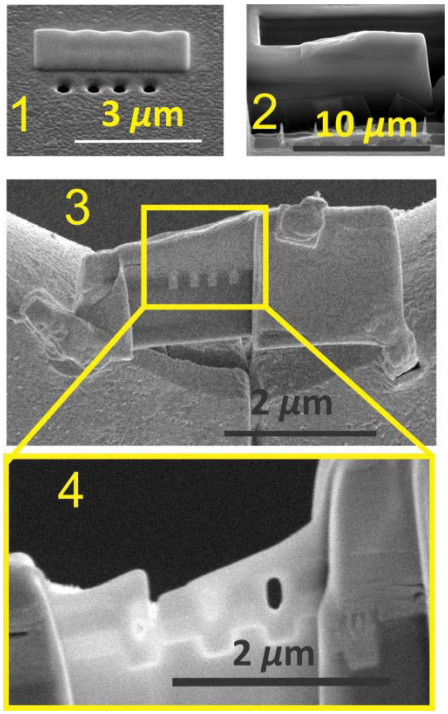

Figure 2—4: SEM images of the process of 1) deposition of PT on the Ti/Si/SiO2 layers after FIB milling. 2) Extraction of a row of PnC holes. 3)Attaching the sample to the TEM grid and thinning down a lamella of the cross section of the PnCs. 4) A lamella of the cross section of PnCs ready for TEM study. This figure is reproduced with permission from supplementary information of another report[33]. © 2015 Mcmillan Publishers Limited.

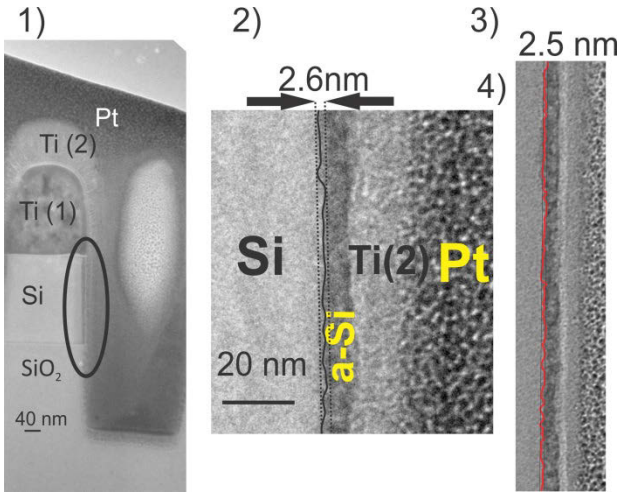

Figure 2—5: TEM study of the PnC hole sidewalls. 1) A low magnification image of a hole cross-section. 2) The interface of Si-a-Si/Ga-Ti-Pt. 2) One interface of Si-a-Si/Ga-Ti-Pt and its corresponding roughness height of about 2.6nm. 4) Another Si-a-Si/Ga-Ti-Pt with a roughness height of around 2.5nm. This figure is reproduced with permission from supplementary information of another report[33]. © 2015 Mcmillan Publishers Limited.

3 Simulation of Acoustic Bandgap

All the materials in this chapter are reproduced with permission from other work [15]. The chapter is a modified version of that report. © 2013, AIP Publishing LLC.

Phononic Crystals (PnCs) are a class of metamaterials that are capable of manipulating elastodynamic waves. Much of the research on PnCs, both theoretical and experimental, focus on studying the transmission spectrum of PnCs in an effort to characterize and engineer their phononic band gaps. Although most studies have shown acceptable agreement between the theoretical and experimental bandgaps perfect matches are elusive. A framework is presented wherein two and three dimensional harmonic finite element analyses are utilized to study their mechanical behavior for the purpose of more accurately predicting the spectral properties of PnCs. Discussions on a Harmonic Finite Elements Analysis (HFEA) formulation of a perfectly matched layer absorbing boundary and how reflections from absorbing boundaries can be inferred via standing wave ratios are provided. Comparisons between 2D and 3D analyses are presented that show the 2D models are equally accurate under certain conditions, but a less computationally intensive alternative for 3D models. Finally, it is shown that a surface excitation boundary condition in a three dimensional model can significantly improve understanding of the experimental results for PnCs excited by surface mounted excitation sources.

3-1 Introduction

Phononic Crystals (PnCs) are materials comprised of a periodic structure of inclusions in a background matrix. This periodic arrangement creates bandgaps in the elastic wave response of PnCs [1, 2, 5, 45]. Considerable attention has been given to the PnCs in the last decade due to their promising applications in filtering of elastic waves and as waveguides [4, 5, 46-48]. To understand the nature of PnCs, many researchers have studied PnC induced bandgaps, and their dependence on different parameters such as arrangement of inclusions and their dimensions [49], filling fraction of inclusion material, and acoustic impedance mismatch between the matrix and inclusion materials [4, 48]. Finite Difference Time Domain (FDTD) [8, 50, 51], and Finite Element Analysis (FEA) [49, 52, 53] are two numerical approaches widely employed to predict and explain the bandgap in PnCs. In these methods, governing equations of continuous elastic media are solved. Although most studies have shown relative agreement between the theoretical and experimental bandgaps [46, 51, 52], perfect matches of the frequency ranges and bandgap depths are elusive, e.g. see references [8, 50].

In order to attain a relatively fast estimation of the bandgap in PnCs, simulations of a 2D infinitely thick model is an alternative to more computationally intensive finite-thickness (3D) model [4]. For FDTD a common approximation is to apply periodic boundary conditions on opposing surfaces while in FEA it is common to assume plane strain or plane stress conditions [54]. Both assumptions

have the effect of turning a 3D model into a 2D model. Estimations from these 2D models for the bandgap frequencies have been widely used instead of the more accurate and computationally expensive three dimensional analyses for PnCs with finite thickness [4, 8, 16]. However these assumptions lead to neglecting surface modes in PnCs.

The FDTD approach solves the governing equations for elastic wave propagation in the time domain. This consists of a time domain simulation energized by an energy source such as an initial Gaussian wave packet of longitudinal waves. The solutions obtained are functions of the discretized simulation time. Then frequency-dependent results are obtained via Fourier transforms. Alternatively, some investigators have used Harmonic FEA (HFEA) to study the behavior of PnCs in terms of either absolute band gap [52, 55] or transmission spectrum [49]. In harmonic analysis, as contrasted with FDTD, the governing equations are solved in the frequency domain and the steady state solution is attained without time discretization [49, 56]. Here, instead of launching a Gaussian wave packet, a set of nodes are harmonically excited at a discrete frequency. Consequently, the transmission spectrum of a PnC is achieved using the steady state solution to the PnC model under line or surface excitations with different frequencies. Even though both FDTD and HFEA are solving the same governing equations, their methods for launching waves are not the same. In HFEA, boundary conditions are employed in the form of an applied force thereby automatically generating different polarizations of waves depending on the frequency of force application,

material properties of system, and geometry of the numerical space. In contrast to HFEA, FDTD launches waves by utilizing an initial condition on displacement. Therefore the polarization of launched waves in FDTD has then implicitly been predefined by the imposed initial conditions in the numerical space. Many researchers have investigated the transmission spectra and band structures of freestanding PnCs subjected to purely longitudinal waves [16, 49]. However for thin plates under piezoelectric excitation, the propagation of Lamb Waves are predominantly observed [55, 57]. Accordingly, some work is devoted to the band structures created by the propagation of Lamb Waves [55, 58, 59]. Additionally, some attention has also been given to propagation of the surface acoustic waves [57, 59, 60] (SAWs). However, to the best knowledge of the authors, there are no studies that have been performed to understand the effects of different modes of Lamb Waves (flexural and extensional modes) or SAW on the transmission spectra of freestanding PnCs.

In this paper, a PnC consisting of a silicon dioxide slab and tungsten inclusions is studied using 3D and 2D HFEA. Results of the current analyses are compared to experimental results and FDTD solutions [8] to study the effectiveness and accuracy of these methods for predicting PnC transmission characteristics and understanding the vibrational behavior of PnCs. Effects of the boundary conditions for launching waves are studied; both extensional and flexural modes are employed. It is shown that the actual transmission spectrum of the PnC under study can be

explained only by considering both flexural and extensional modes, which are present due to the surface-mounted transducers used in experiments.

3-2 Theory

Governing Equation

Equilibrium in a continuous medium can be written as:

$$\sigma_{ij,j} + f_i = \rho \ddot{u}_i \tag{3-1}$$

where, σ , f , u are the stress tensor, body forces, and displacement vectors, respectively. A comma in the subscript denotes a spatial derivative. Subscript letters denote spatial coordinates, which run between 1 and 3, and a dot over a symbol denotes a time derivative. According to Hooke's Law, in an elastic medium:

$$\sigma_{ij} = c_{ijkl}\varepsilon_{kl} \tag{3-2}$$

where c is the fourth order elasticity tensor, and ε is the strain tensor. In a linear analysis, with the infinitesimal strain assumption:

$$\varepsilon_{ij} = \frac{1}{2}(u_{i,j} + u_{j,i}) \tag{3-3}$$

In isotropic media the elasticity tensor depends on the Lame´ parameters λ and μ:

$$c_{ijkl} = \lambda\delta_{ij}\delta_{kl} + \mu(\delta_{ik}\delta_{jl} + \delta_{il}\delta_{jk}) \tag{3-4}$$

Where δ_{ij} is the Kronecker delta and the Lame´ parameters are obtained from Young's Modulus E and Poisson's Ratio ν via:

$$\lambda = \frac{\nu E}{2(1+\nu)(1-2\nu)} \tag{3-5-a}$$

$$\mu = \frac{E}{2(1+\nu)} \tag{3-5-b}$$

Furthermore, substituting Eqs. (3-2 to 3-4) into Eq. (3-1) to leads to [61]:

$$(c_{ijkl}u_{k,l})_{,j} - f_i = \rho\ddot{u}_i \tag{3-6}$$

Eq. (3-6) is the governing equation for a lossless domain used by both FEA and FDTD. Thorough discussions of Perfectly Matched Layers (PML), and absorbing boundaries for FEA and FDTD can be found elsewhere [62-64]. The two-dimensional FEA implementation in this work assumes a plane stress formulation.

FEA implementation

Discretizing Eq. (3-6) into an assemblage of finite elements yields [65]:

$$\mathbf{M}\ddot{\mathbf{u}} + \mathbf{K}\mathbf{u} = \mathbf{F} \tag{3-7-a}$$

where:

$$\mathbf{M} = M_{ij}^{I} = \int_{\Omega} \rho N^{I} N^{J} \delta_{ij} d\Omega \tag{3-7-b}$$

$$\mathbf{K} = K_{ij}^{I} = \int_{\Omega} N_{,k}^{I} c_{ijkl} N_{,l}^{J} d\Omega \tag{3-7-c}$$

$$\mathbf{F} = F_{i}^{I} = \int_{\Omega} N^{I} f_{i} d\Omega + \int_{\Gamma_{\sigma}} N^{I} \bar{t}_{i} d\Gamma \tag{3-7-d}$$

$$\mathbf{u} = u_{j}^{I} \tag{3-7-e}$$

where **M**, **K** and **F** are the mass, stiffness and force matrices, respectively. The capital superscripts in the above equations stand for the node number running from 1 to the number of nodes, the subscript letters denote spatial coordinates, N stands for the shape functions, and $\bar{t}$ is the traction vector. Moreover, Ω is the element domain, Γ is the boundary, and Γ_{σ} is the boundary on which the traction vector is given.

In harmonic analysis, the assumption is that only harmonic forces are applied and body forces are much smaller than other external forces. Then Eq. (3-7-d) becomes [66]:

$$\mathbf{F} = \int_{\Gamma_\sigma} N^I \bar{t}_i(x) \sin(wt + \psi_i(x)) d\Gamma \tag{3-8}$$

Or:

$$\mathbf{F} = \mathrm{Re}(\hat{F}_i^I e^{i(\omega t + \psi_i^I)}) \quad \text{no sum on I and i} \tag{3-9}$$

The harmonic steady state response of the system can be expressed in terms of complex functions as well:

$$\mathbf{u} = \mathrm{Re}(\hat{u}_j^I e^{i(\omega t + \varphi_j^I)}) \quad \text{no sum on I and i} \tag{3-10}$$

where $\hat{u}_j^I$ and $\hat{F}_j^I$ are amplitudes of displacement and force vectors at node I, φ^I and ψ^I represent the phase components. Substituting Eqs. (3-8 to 3-10) into Eqs. (3-7a to 3-7d) and simplifying leads to:

$$(-\mathbf{M}\,\omega^2 + \mathbf{K})(\mathbf{u}' + i\mathbf{u}'') = (\mathbf{F}' + i\mathbf{F}'') \tag{3-11}$$

where ω is the excitation frequency, $\mathbf{u}'$ and $\mathbf{u}''$ are real and imaginary displacements, respectively. Similarly, $\mathbf{F}'$ and $\mathbf{F}''$ are real and imaginary forces. These are usually combined by adopting a complex formulation. Results are obtained by solving the linear system prescribed in Eq. (3-11).

FDTD Implementation:

FDTD starts with the governing equation, Eq. (3-6). Simply stated, temporal and spatial derivatives in Eq. (3-6) are replaced with finite differences of discretized space and time dimensions and the equation is rearranged to provide explicit time-dependent solutions of the dependent variables, themselves defined on a grid of the discretized spatial dimensions. In this article, the HFEA results are compared with the FDTD attained elsewhere [8], which itself follows the displacement/stress formulation from other references [64]. In this paper, the common technique of launching an initial Gaussian pulse of longitudinal waves is employed in the time domain, which includes different frequencies in Fourier space. This technique of launching waves is one of the main inherent differences between HFEA and FDTD.

3-3 Simulations and Device for Experiment

FDTD Simulation

FDTD simulations implemented a displacement-stress formulation with a staggered grid. The phononic crystal consisted of one row of five tungsten inclusions inside a silicon dioxide matrix. The lattice constant was 2.5 μm and the rod radii were 0.6 μm. The PnC thickness was 1.85 μm. The numerical space was terminated in the propagation direction (equivalent to the z-direction in Fig.

3—1) with Mur absorbing boundary conditions [64]. To model an infinitely periodic structure along the in-plane transverse direction (equivalent to the y-direction in Fig. 3—1), periodic boundary conditions were employed. Air covered the slab in the out-of-plane transverse direction (equivalent to the x-direction in Fig. 3—1) except for small portions of silicon dioxide to cover the Mur absorbing boundaries. Energy into the simulations was provided by an initial condition in the form of a plane wave with a Gaussian profile aligned in the propagation direction. Displacements on the far side of the PnC were recorded at every time step, then Fourier transformed separately and summed up to obtain the PnC transmission in the frequency domain. The PnC transmission values were normalized by the matrix transmission, which was obtained by removing all the tungsten rods and leaving the rest of the simulation unchanged.

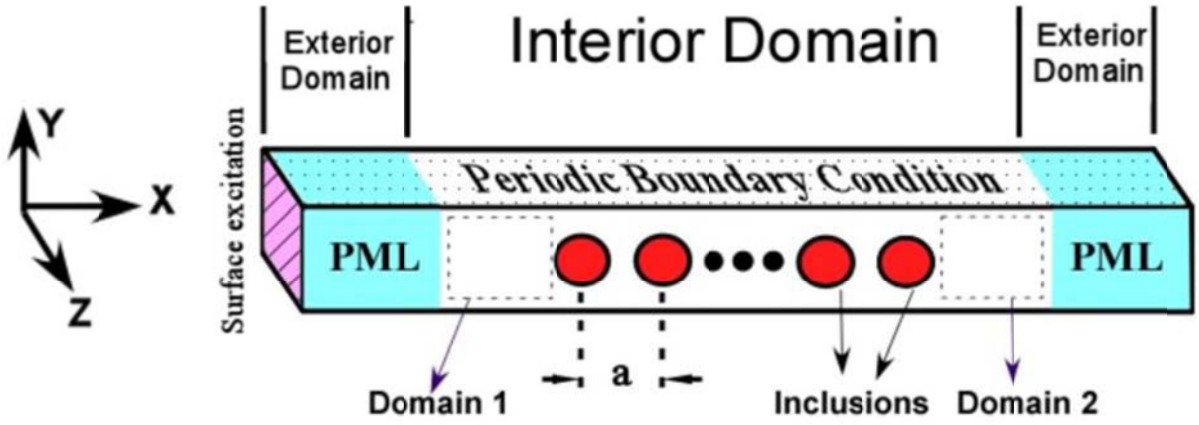

Figure 3—1: Numerical space of the 3D HFEA of the PnC.

FEM Simulations

In Fig. 3—1 the three-dimensional numerical space is illustrated. The phononic crystal consists of one row of 19 tungsten inclusions inside a silicon dioxide matrix in order to match experimental conditions in other references [8]. The lattice constant is 2.5 μm in the x and y directions and the tungsten rods have radii of 0.6 μm. The thickness of the PnC is 1.85 μm. To model an infinitely periodic structure along the y-direction, periodic boundary conditions are employed on the bottom and top nodes. In Table 3-1 the density, Young's Modulus, Poisson's ratio, and speed of sound (c) of silicon dioxide and tungsten are shown.

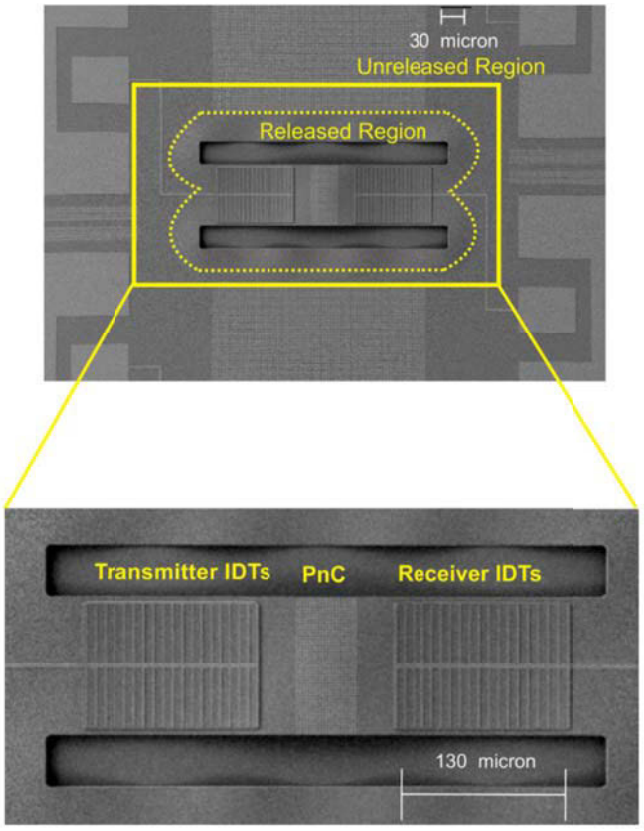

Figure 3—2: SEM image showing the top view of the PnC, transmitter, and receiver used in the experiment to measure the transmission spectrum. The yellow dashed line displays the border between the freestanding and supported regions.

The domain is divided into three regions: the interior domain comprised of the PnC enclosed by the matrix; and two exterior domains performing as perfectly matched layers (PMLs). The PMLs serve to attenuate the outgoing waves, and reflect little to no energy back into the PnC. Longitudinal waves are launched into the PnC by harmonic excitation of the nodes on the left surface of the

leftmost exterior domain, see Fig. 3—1. In essence, this method simulates waves incident from infinity into the interior domain, and scattered waves dissipate in the PMLs.

To assess the performance of the PMLs' ability to absorb energy, standing wave ratios (SWRs) between the PML/Matrix interface and the PnC's walls are computed during each analysis. By this method one can evaluate the performance of the PMLs without studying them directly. The SWR is defined in frequency domain as:

$$SWR_X = \frac{\widehat{u}_1^{\min}}{\widehat{u}_1^{\max}} \tag{3-12}$$

where $\widehat{u}_1^{\min}$ and $\widehat{u}_1^{\max}$ are minimum and maximum amplitudes of displacement along x-direction over the numerical space between the PnC and the PML. The subscript X on SWR refers to which Domain (1 or 2) is under examination, and only $\widehat{u}_1^{\min}$, and $\widehat{u}_1^{\max}$ in that domain are examined. In Domain 2, if this ratio is equal to 1, the media has only forward or outgoing waves without any wave passing along the opposite direction so the corresponding PML reflects no wave. With this definition of SWRs the PML's reflection error can be defined as:

$$Error = 1 - SWR_2 \tag{3-13}$$

In particular, the error computed in Domain 2 is calculated in each analysis to determine the portion of the scattered waves that are reflected by the PML. In addition to checking errors in the numerical space, SWRs are used to calculate the amplitude of the incident waves. With plane-wave excitation,

the incident waves in the interior domain are three orders of magnitude smaller than the applied nodal displacement at the source in the left PML. Consequently, when the $Error$ in Eq. (3-13) is negligible (in this work, a criterion of $Error$ smaller than 0.05 is set) the relative amplitude of the incident waves of Domain 1 can be determined by:

$$\hat{u}_f = \frac{\hat{u}_1^{\max}}{1+r} \tag{3-14}$$

where $\hat{u}_f$ is the amplitude of the wave traveling from the left PML and incident to the left side of the PnC. Here r is reflectivity of the PnC, and it can be computed via:

$$r = \frac{1 - SWR_1}{1 + SWR_1} \tag{3-15}$$

Computing SWR_2 shows the reflectivity of the PML/Matrix interface to justify calculation of the incident wave using Eq. (3-14). We assume both PML/Matrix interfaces have the same reflectivity. Eqs. (3-14 and 3-15) are valid for a semi-infinite medium. Therefore, at least one interface of the interior domain should have a very small reflectivity. This condition is satisfied by keeping Error, the value of Eqn. (3-13), small.

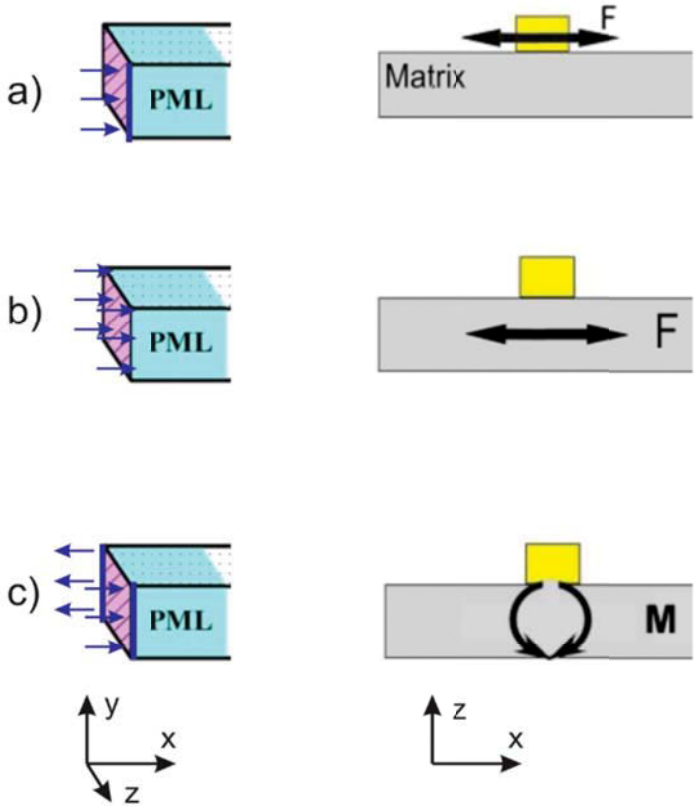

Figure 3—3: Different boundary conditions, cf. Fig.3—1, employed at far field that apply harmonic forces: (a) a combination of both flexural and extensional waves on the surface of the matrix, (b) pure extensional waves, and (c) pure flexural waves.

After determining the standing wave ratios in the numerical domain and verifying that the PMLs are performing properly, the transmission of the phononic crystals is determined. The transmission is attained by demining the amplitude of the waves incident to the PnC in Domain 1, according to Eq. (3-14), and the amplitude of the waves transmitted through the PnC in Domain 2. In this work in

presenting numerical transmissions (either HFEA or FDTD) the values lower that -43dB are neglected since they represent extremely small numerical or experimental transmission.

Table 3-1: Materials that constitute the PnC

	Tungsten	Silicon Dioxide
Density (kg/m^3)	19200	2200
Young's Modulus (GPa)	409	75
Poisson's Ratio	0.25	0.17
Sound Speed (m/s)	4615	5838

As shown in Fig. 3—2, the experiment has two sets of AlN Interdigitated Transducers (IDTs), launching and receiving acoustic waves, as well as the PnC located on a freestanding membrane between the IDTs. The set of IDTs on the left (Transmitter) launches the acoustic waves, to be detected by the set of IDTs (Receiver) on the right. All the IDTs and PnC are freestanding, and the Transmitter is electrically connected to a network analyzer. The IDTs are fabricated by deposition of a thin layer of AlN on the matrix. Only a small fraction of the power from the network analyzer is converted to acoustic energy in the Transmitter and received by the Receiver after passing through the PnC. The experimental transmission is determined by normalizing the transmission of the PnC to that of the matrix.

Extensional and Shear Excitation Forces

Deposited piezoelectric materials on the surface of the slab apply a complicated combination of extensional and shear forces. The applied force generated by a surface-mounted piezo-device can be simulated by application of an in-plane force on the surface, see Fig. 3—3a. This would lead to both extensional and flexural modes, i.e. surface acoustic waves. This type of force excitation can be decomposed into flexural and extensional components. The extensional component is simulated by applying a uniform distribution of in-plane, in-phase surface pressure, see Fig. 3—3b. This boundary condition leads to only extensional excitation or purely longitudinal waves. The flexural component is generated by applying a pair of out-of-phase line forces on the slab surfaces (Fig. 3—3c). This pair of line forces is equivalent to a moment applied to the mid-plane.

3-4 Results and Discussion

The transmission of the PnC predicted by the Harmonic FEA (HFEA) using 2D and 3D approaches are presented in Fig. 3—4a. In this plot, the 3D simulation is compared with the 2D model along with the actual experimental results previously reported by Su et al. For this 3D simulation, the PnC is excited by only the in-plane, in-phase surface pressure (referred to as "3D Extensional Mode" see Fig. 3—3b) in order to generate extensional modes. In this way, the 3D results will be comparable

to the 2D case where inherently no flexural modes are allowed. The comparison shows that the 2D and 3D HFEA models predict a similar primary bandgap. Here, the beginning and end of the bandgap are defined by a transmission of -10 dB. The predicted beginning frequency is about 80 MHz lower than the experimental prediction while the end frequency of the bandgap is 20 MHz higher. This comparison reveals that both 2D and 3D HFEA models, taking solely extensional waves into account, can accurately predict the primary phononic band gap. However, Fig. 3—4a also demonstrates that the 2D model fails to predict the experimental secondary band gap from 1180 MHz to 1390 MHz. In contrast to the 2D model, the 3D model predicts this bandgap, however its end frequency is 60 MHz smaller than the experimental value.

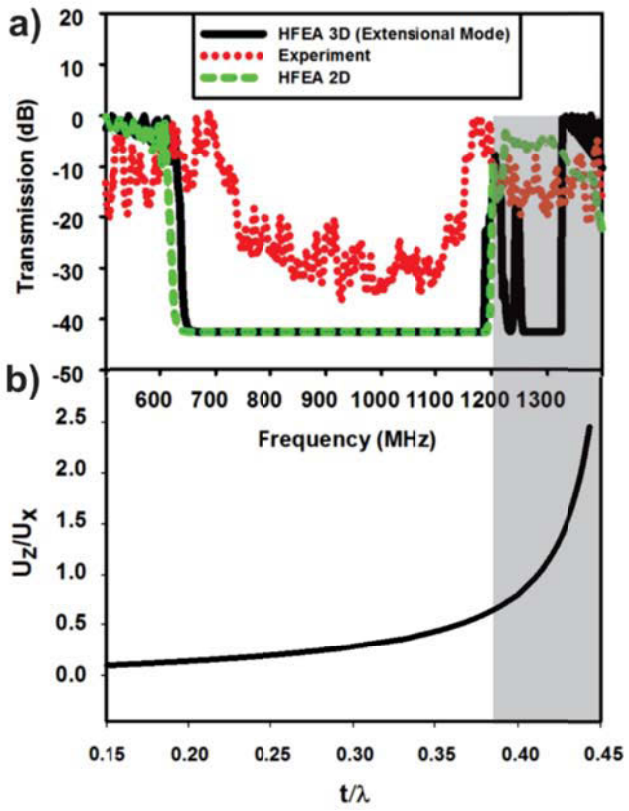

Figure 3—4: (a) Transmission spectrum based on 2D FEA (dashed green line), 3D FEA taking only extensional waves into account (black solid line), and the experiment (red dotted line). (b) Ratio of out-of-plane displacement to in-plane displacement along with wave vector versus dimensionless excitation wavelength. The gray shaded region indicates the frequencies at which the 2D and 3D finite elements analyses do not match in (a).

The discrepancy between the 2D and 3D analyses raises the question of accuracy for the 2D analysis. This question is addressed in Fig. 3—4b. In this figure the ratio of out-of-plane displacement (u_3) to the in-plane displacement (u_1) on the right side of the PnC for the Extensional Mode is depicted for a range of dimensionless frequencies as defined by the ratio of the thickness (t)

of the PnC to the wavelength (λ). The displacement ratio indicates the significance of the surface modes to the physics of the problem. The horizontal axis of Fig. 3—4b is the dimensionless frequency $\nu_0 t/c(= t/\lambda)$, which corresponds to the frequency (ν_0) of the horizontal axis in Fig. 3—4a. This dimensionless frequency is significant because it relates the extensional modes in the slab to the fundamental out-of-plane resonant mode of the slab. As seen in Fig. 3—4b, when the Extensional Mode wavelength approaches twice the slab thickness, the out-of-plane displacements are greatly excited as their excitation frequency is close to the natural frequency of the out-of-plane vibration. The shaded regions of Fig. 3-4a, b demarcates the range of t/λ where the secondary bandgap of Fig. 3—3 occurs (around 1.3 GHz). In this region, the 2D HFEA is not in agreement with the experiment or the 3D model. One notices that in the shaded box the 3D HFEA shows a ratio of out-of-plane to in-plane displacements to be between 0.7 and 2.5. These relatively high ratios indicate that the out-of-plane displacements are significant. The 2D analysis does not take the out-of-plane displacements into account and therefore cannot predict the secondary bandgap. While the 2D model requires a smaller numerical space, and as a consequence is drastically faster than the 3D model, it is only applicable for values of the dimensionless frequency that are smaller than 0.37, with smaller values being increasingly more accurate.

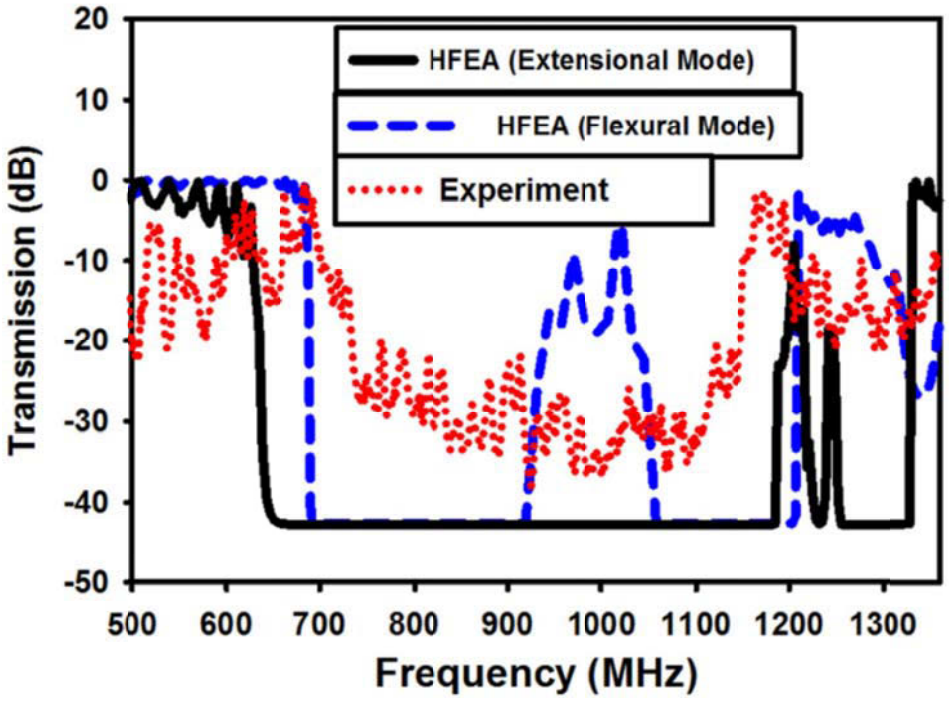

Figure 3—5: Comparison between the experimental transmission spectrum (red dotted line) with the 3D FEM assuming extensional excitation (black solid line) and flexural excitation (blue dashed line).

Even though the 3D model shown in Fig. 3—4a is considerably more accurate than a similar 2D model it still predicts the beginning frequencies of the primary and secondary bandgaps inaccurately. This is due to the use of only an extensional mode of excitation. In order to corroborate the computational results with experiments, which use surface-mounted piezodevices to excite the PnC, the phononic crystal is studied under only flexural in-plane excitation as well. For this situation, initial excitation is attained by applying a pair of in-plane out-of-phase harmonic

forces (referred to as “3D Flexural Mode” below), see Fig. 3—3c. This combination of forces applies a pure harmonic moment on the slab. In Fig. 3—5, the displacements on the surface of the slab along the x-direction are compared for extensional and flexural forces. Both the experimental results and 3D Flexural Mode analysis are in agreement at the frequency of 680 MHz for the beginning of the bandgap. However, the 3D HFEA under pure flexural excitation does not agree with the experiment at the middle of the primary bandgap, and at the secondary bandgap. The 3D Extensional Mode analysis accurately captures the secondary and a part of the primary bandgap while the 3D Flexural Mode analysis predicts the starting frequency of the band gap better. This result strongly suggests that the actual behavior of the PnC should be modeled by launching the correct combination of the flexural and extensional waves as shown in Fig. 3—3a. This is equivalent to a surface excitation. Herein this is referred to as the 3D Combined Mode.

The transmission spectrum of the PnC under Combined Mode excitation, as shown in Fig. 3-3a, is depicted in Fig. 3—6. It is also compared with the experiment and the FDTD method previously published by Su et al.[8] Here, the Combined Mode HFEA agrees with the experiment better than the 2D, 3D Flexural, and 3D Extensional Mode analyses. This model shows a shallower secondary bandgap closer to the experiment and a primary bandgap with a more accurate prediction of the bandgap’s width. Additionally, the Combined Mode HFEA lacks the unverified peak in the middle of the primary bandgap indicated by the 3D Flexural Mode analysis, see Fig. 3—5. Even though the Flexural Mode is a better match with the experiment around 700 MHz, it displays a significant peak at the middle of bandgap, which breaks the primary bandgap into two substantially smaller

bandgaps. Therefore even though at some frequencies the Flexural Mode or Extensional Mode HFEA shows an advantage over the Combined Mode, the Combined Mode is preferred overall as it is more accurate in terms of the width and depth of the bandgaps.

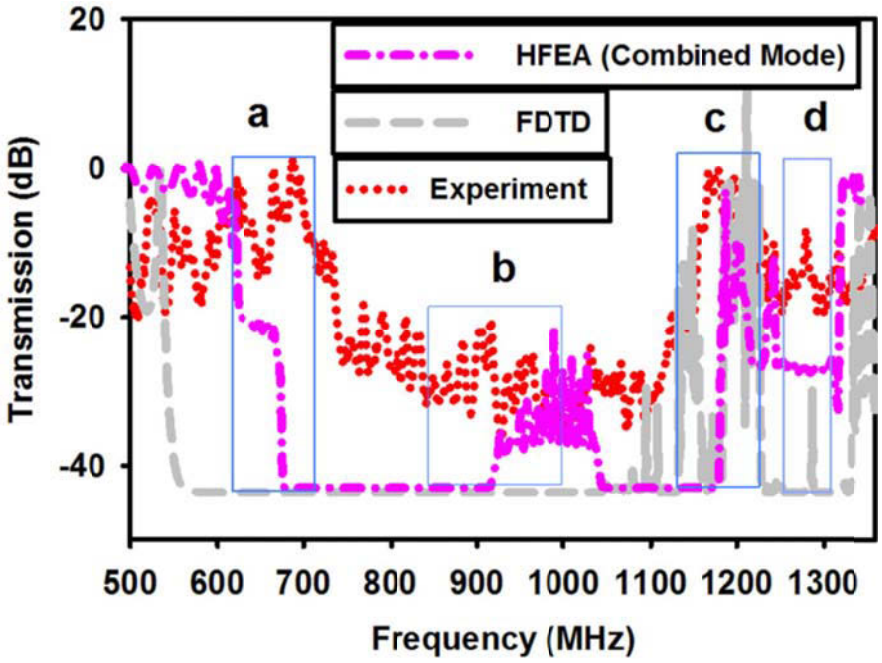

Figure 3—6: Transmission spectrum based on the experimental data (red dotted line), FDTD[8] (grey dashed line), and Harmonic FEM taking both extensional and flexural excitations into account (pink dash-dotted line). In the boxed regions, the vibrational behaviors of the PnCs are illustrated in Fig.3—7.

In comparison to the FDTD prediction of the bandgap, the Combined Mode HFEA more accurately models the behavior of the PnC from the aspects of bandgaps' widths and depths. Here the major difference between FDTD and the current model is the boundary conditions used for launching

waves. In typical FDTD implementations, launching of waves is attained by applying a Gaussian wave packet in the time domain such that only longitudinal waves can exist in the numerical space. In contrast to FDTD, the current HFEA model utilizes a boundary condition consistent with the nature of the surface-mounted piezoelectric transducer used in the experiments. Since this boundary condition is driven by force, mathematically and physically different polarizations of waves can be generated in the numerical space depending on the response of the structure. This will result in a broader range of possible wave polarizations in the HFEA numerical domain than the FDTD numerical domain with a predefined initial package of waves. This means that HFEA inherently will show the same or narrower band gap than the FDTD method due to the presence of different modes of waves.

Figures 3—7a to d show the displacement profiles of the PnC at four different frequencies (660, 900, 1190, and 1300 MHz) that have been marked by boxes in Figure 3—6 with the corresponding letters. The propagating modes depicted in Fig. 3—7 are representative of the modes propagating in the range of frequencies around the corresponding box in Fig. 3—6. The following paragraphs discuss each range of frequencies in further detail.

Since FDTD and Combined Mode HFEA do not agree at the beginning frequencies of the primary bandgap, one may suggest that the vibrational behavior of the PnC is flexural at these frequencies. In Fig. 3—7a the out-of-plane displacement contours are shown at the frequency corresponding to the box marked by the letter ‘a’ in Fig. 3—6. This frequency range is around the beginning of the

PnC's primary bandgap. The displacement contours in Fig. 3—7a indicate that flexural modes are dominant in this frequency range. As discussed, one needs to include flexural excitation in the analysis to observe such a behavior of the PnC. This confirms that due to a lack of flexural modes in this range of frequency the experimental transmission was not predicted previously[8] by FDTD.

The FDTD and Combined Mode HFEA results are in agreement with the experiment in the middle and end frequencies of the primary bandgap. This suggests a similar behavior of the PnC is simulated by both methods. In Fig. 3—7b contours of the in-plane displacements along the x-coordinate show a dominant extensional mode of vibration at the frequencies corresponding to the box 'b' in Fig. 3—6, which includes mostly longitudinal waves. This range shows the middle of the primary bandgap, which is recognized as a range of frequencies falling in the primary bandgap by both FDTD and Combined Mode HFEA. Moreover, the in-plane displacement contours corresponding to the frequencies close to the end frequency of the primary band gap (i.e. box 'c' in Fig. 3—6) are depicted in Fig. 3—7c. This plot again implies that extensional modes are dominant at the end of the primary bandgap, which includes mostly longitudinal waves. Accordingly, dominance of the extensional modes (due mostly to longitudinal waves) explains the agreement between the FDTD and the HFEA Combined Mode, as both these methods can simulate propagation of longitudinal waves well.

Even though both FDTD and HFEA Combined Mode show similar frequencies for the secondary bandgap, their depths are different. This difference suggests that the effect of flexural waves is not

dominant but non-negligible in this frequency range, see Fig. 3—6. Again, it is confirmed in Fig 3—7d, where the deformed PnC obviously shows a combination of both flexural and extensional waves. Here this plot verifies that by including the flexural excitation the HFEA Combined Mode improves the prediction of the bandgap as it is closer to the experimental results, see Fig. 3—6. Therefore, the influences of the flexural waves on transmission at high frequencies are significant as well. This study suggests that it is essential to apply both flexural and extensional excitation, i.e. surface excitation, in an effort to better understand the experimental transmission spectrum.

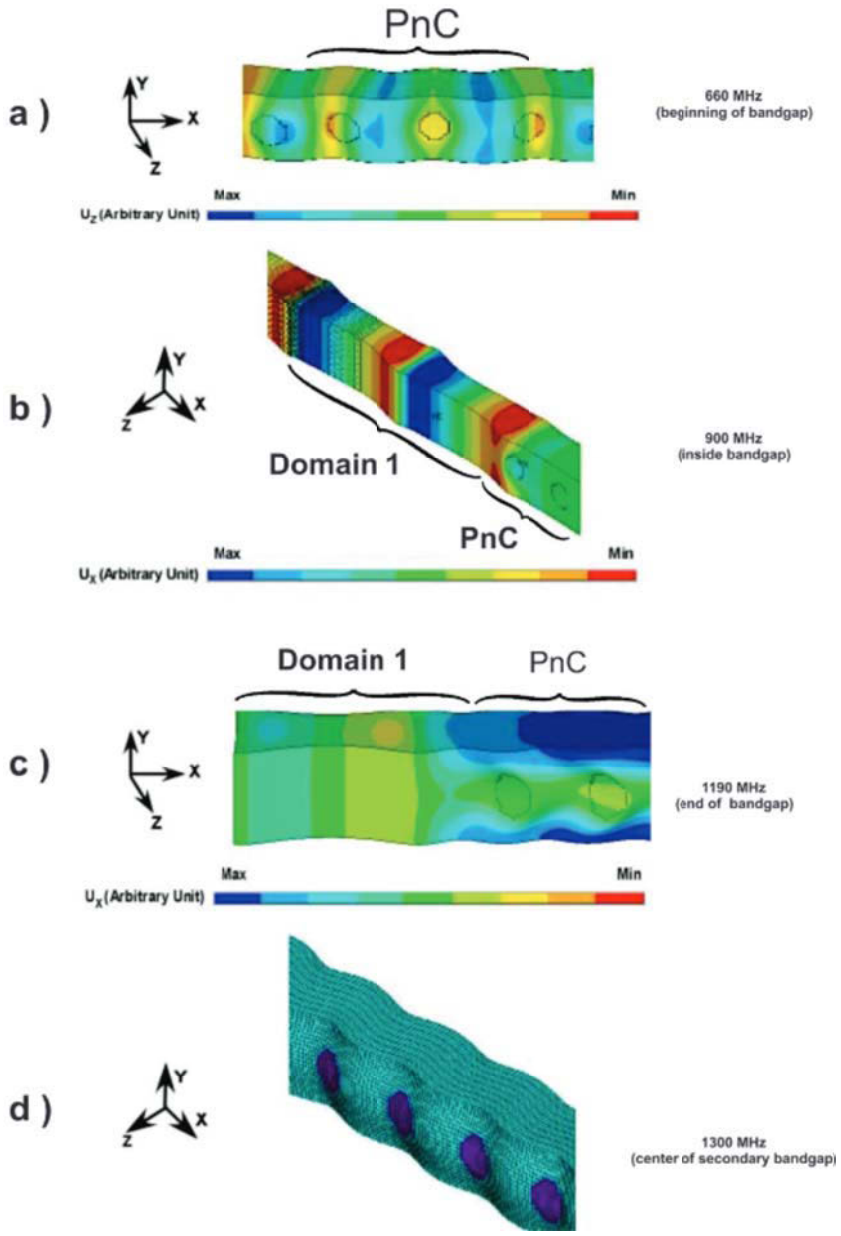

Figure 3—7: Vibrational behavior of the PnC at the frequencies boxed in Fig.3—6. (a) Out of plane displacement contours at the frequency of 660 MHz (beginning of band gap) boxed as 'a' in Fig.3— 6. (b) In-plane displacement along x-direction at frequency 900 MHz (middle of the band gap) boxed as 'b' in Fig. 3—6 . (c)

Displacement along x-direction at 1190 MHz (end frequency of primary band gap) boxed as 'c' in Fig.3— 6. (d) Deformed PnC at the middle of the secondary band gap boxed as 'd' in Fig.3—6.

A perfect match between experiment and theory is always elusive, as there are many parameters affecting the experiment, which are uncharacterized. For example, at the nanoscale, the adhesion between interfaces, frequency dependent material losses, and roughness depend on the method of fabrication. To the best knowledge of the authors, no one has studied the effect of these parameters on the transmission spectra of PnCs. To wit, around 700 MHz, there are still some discrepancies unresolved between the experiment and the theory even when the most representative boundary conditions from this study are employed (Combined Mode). These discrepancies can be associated to any of the aforementioned unknowns. This work contributes to improvement of the analysis of PnCs, in view of the current technology of the experiment, by applying examining different boundary conditions. Future works will be performed in order to better understand the effects of other parameters not currently included in these models.

3-5 Conclusion

Herein a framework for study of the transmission spectrum in PnCs was presented. The transmission spectrum of PnCs working at GHz frequencies has been studied using two and three-dimensional HFEAs. For the 3D finite element models, three different boundary conditions for launching waves

were considered: pure extensional forces (Extensional Mode), pure flexural forces (Flexural Mode), and surface excitation (Combined Mode) inspired by the actual surface-mounted piezoelectric transmitter mechanism. It was revealed that when only the Extensional Mode is considered for a 3D model, the 2D analysis leads to a similar transmission spectrum at dimensionless wavelengths (wavelength divided by thickness) smaller than 0.37. Accordingly, for this range of frequencies, the 2D analysis can be a fast and computationally less expensive alternative for the 3D analysis. However, the 3D analysis considering both flexural and extensional modes can explain the transmission spectrum more accurately for the entire range of frequencies. The comparison made between the 3D HFEA Combined Mode, FDTD, and the experiment showed that the HFEA Combined Mode considering both flexural and extensional modes explains some range of frequencies in and out of the band gap that was obscured in previous efforts. The current work showed that in this range of frequencies the flexural waves are dominant. It was also shown that surface excitation can significantly affect the PnC behavior at both low and high frequencies. This study suggests that consideration of both flexural and extensional modes in theoretical studies improves interpretation of the experimental transmission spectra.

4 Thermal Characterization

All the materials in this chapter are reproduced with permission from another report[30]. The chapter is modified version of that report. © 2013 IOP Publishing Ltd.

A technique based on suspended islands is described to measure the in-plane thermal conductivity of thin films and nano-structured materials, and is also employed for measurements of several samples with a single measurement platform. Using systematic steps for measurements, the characterization of the thermal resistances of a sample and its contacts are studied. The calibration of the contacts in this method is independent of the geometry, size, materials and uniformity of contacts. To verify the technique, two different Si samples with different thicknesses and two samples of the same SiN_x wafer are characterized on a single device. One of the Si samples is also characterized by another technique, which verifies the current results. Characterization of the two SiN_x samples taken from the same wafer showed less than 1% difference in the measured thermal conductivities, indicating the precision of the method. Additionally, one of the SiN_x samples is characterized and then demounted, remounted, and characterized for a second time. The comparison showed the change in the thermal resistance of the contact in multiple measurements could be as small as 0.2 K/μW, if a similar sample is used.

4-1 Introduction

The common designs for the dual suspended island (DSI) technique have been broadly used for measuring in-plane thermal properties of compliant samples such as nano-tubes [67, 68], nano-films[69], and nano-wires[62]. In this technique, two SiN_x islands with platinum serpentine patterns are suspended, on which the platinum patterns are integrated thermometer/heaters[70]. On one island electrical power is applied such that the heat on that side is guided through the sample connecting the island to the other island. Prior to a measurement, the sample is fastened to the islands with the aid of a Focused Ion Beam (FIB)[71] and platinum Gas Injection System (GIS). A popular method for sample placement makes use of dispersion in a solvent, which causes difficulties with reusing devices. Another issue in device reuse is that the process of fastening the sample to the platform is likely to contaminate the temperature sensors by FIB and GIS, and hence the thermal electrical properties of the sensors might change after each measurement. It is also evident that the technique of dispersing cannot work for a vast group of samples, including thin films. Another drawback of this method in its current form is that sample placement and fastening create an unknown contact resistance between the sample and device. To overcome such a limitation, recently, a method of four-probe measurement was introduced for the characterization of the contact resistance using the characterization of the sample's Seebeck Coefficient [72, 73]. In this method, a well-controlled, long and uniform contact is preferred, because of the assumptions on the heat transfer through the contact. In addition to characterization of contact resistance, it is also possible to minimize the contact resistance via co-fabrication of the sample and device [74]. However, such a

technique still requires several different devices with different samples for calibration. Furthermore, such devices cannot be reused with another sample in order to verify the repeatability of each single device or sample.

The current work demonstrates an improvement to the DSI technique such that the platforms can be re-used for multiple samples, and the platforms can accept a wider range of samples, such as thin films. This method employs a FIB, GIS, and Omniprobe systems for transferring, mounting, and demounting samples. In the enhanced platforms, a thick layer of AlN covers both islands. This layer protects the platinum sensors from changes in thermal electrical properties due to the use of FIB and GIS during the sample mounting/demounting processes. Therefore, the platform can be re-used for mounting several samples. The AlN layer also favorably decreases the maximum temperature change on each island due to its thermal conductivity being higher than that of the silicon nitride. In addition, one island is anchored to the substrate for better control over the differential temperatures of the islands. This device is demonstrated and studied in this work for the characterization of multiple samples. Reusing a platform can potentially be a new way to eliminate the systematic errors in measurement of nanosamples.

A new technique is also proposed to determine the thermal resistance of the contact between each sample and the device such that its effect can be removed from subsequent measurements. Since this technique assumes only a 1D heat transfer, it is appropriate to study the contact resistance when

the contact sample is very uneven or poor. This calibration is shown to be crucial when the samples are thin films with a lower thermal resistance comparable to that of the sample.

This work also studies the repeatability of remounting the same sample and the repeatability of the DSI platform itself. A single DSI platform is chosen for all measurements. Two different samples of Si with different thicknesses are studied and two SiN_x samples from the same wafer are studied. Furthermore, one of the SiN_x samples are demounted from the platform, remounted, and characterized again. It is shown that all the results for the SiN_x showed excellent consistency with less than 1% change in readings of the thermal resistance, and all the current experimental results for the thermal conductivity of silicon and silicon nitride samples are also in agreement with previous reports.

4-2 Fabrication

The processing for fabrication is briefly depicted in Figure 4—1, and the fabricated platform is comprised of two islands made from SiN_x, as shown in Fig. 4—2. The details for the steps of the fabrication can be found elsewhere [30]. One of the islands has no release holes, therefore after the final release in XeF_2 it will remain anchored to the Si substrate. This island is dubbed the cold island, as its temperature stays close to that of the substrate. The other island has several release holes, and therefore it is fully suspended after the final release in XeF_2; this island is called the hot island. Each island has a serpentine pattern of platinum, which acts as an integrated temperature sensor and heater. Each island has six legs made from SiN_x, and covered by platinum to provide the

electrical connections. The 1 μm thick film of AlN on each island protects the temperature sensors (*i.e.* platinum serpentine patterns) from various sources of contamination during transfers of samples. The AlN film is a dielectric (ρ = 2.1×10^{15} Ω-cm) and features a relatively high thermal conductivity of 70 W/m-K [75].

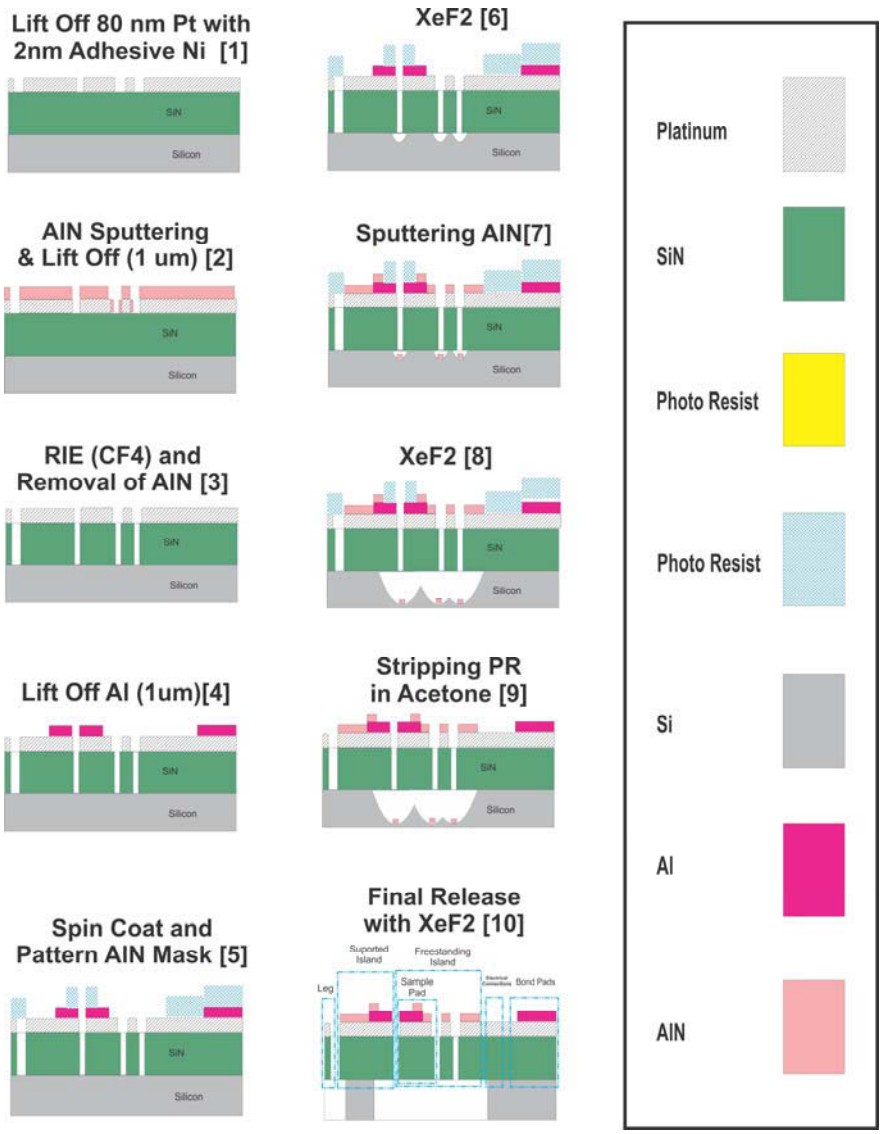

Figure 4—1: Fabrication processes for the suspended island platforms.

a)

b)

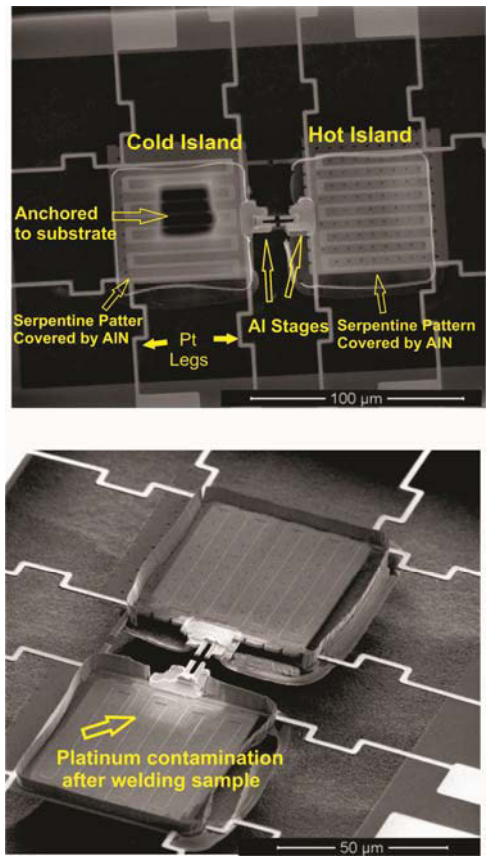

Figure 4—2: SEM images showing the platform comprised of a cold island, hot island, and two Al stages with twelve legs. a) Image taken with high voltage (30 kV) shows the cold island is anchored to the substrate while the hot island is fully suspended and each island has a platinum serpentine pattern. b) Image taken with low voltage (2 kV) shows the surface of the device. A thin layer of platinum contamination is evident after several sample welded and measured.

4-3 Theory of Operation

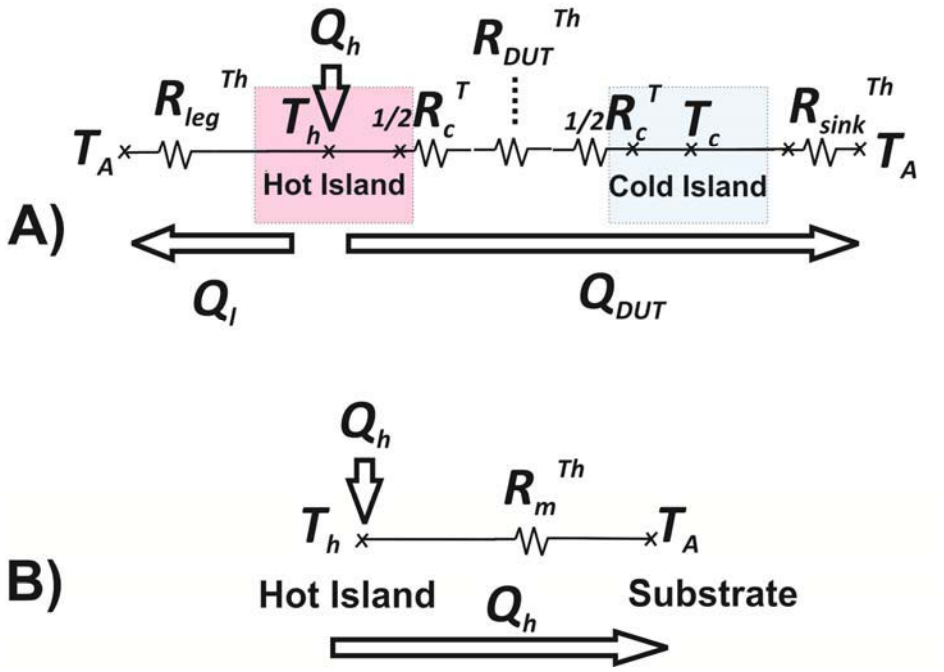

Figure 4—3: Thermal circuit of a) all the components in the platform, and b) the simplified thermal network.

The thermal circuit of a platform is depicted in Fig. 4—3a. Electrical power is applied to the heater, Q_h, resulting in temperature of T_h. This thermal energy then travels to the substrate, temperature T_a, via the Device under Test (DUT), Q_{DUT}, or via the legs of the suspended island, Q_l. The path through the DUT contains several thermal resistances before the substrate. These can be enumerated in order as a contact resistance where the DUT contacts the hot island, R_c^{Th}, the thermal resistance of the sample or DUT, R_{DUT}^{Th}, the contact resistance of the DUT to the cold island R_c^{Th} and finally a resistance between the cold island and the substrate itself, R_{sink}^{Th}. The radiation heat transfer between the sample and the ambient is in the order of 10^{-7} W, which is two orders of magnitude smaller than the power due to conduction. However, when the variation of the

temperature is small, this small radiation can be considered as a part of the leg resistance, which is calibrated in this work. Furthermore radiation can cause error in calibration of the platinum sensors [72]. In this work, a correction on the TCR calibration of sensors, about 2%, is made; this is reflected in the error bars since the emissivity constant is unknown.

Fig. 4—3a can be further simplified to combine all the resistances in the path as shown in Fig. 4—3b. Then, all the power Q_h is transferred through one equivalent resistor R_m^{Th}. Therefore, the relationship between the thermal resistance and power is:

$$T_h - T_A = Q_h R_m^{Th} \tag{4-1}$$

From this point forward, the challenge is to measure R_m^{Th} . To determine R_m^{Th}, the input power and temperatures are measured separately. Different powers are applied to the platinum serpentine heater (Q_h) and simultaneously the electrical resistance of the serpentine heater is measured. The temperature corresponds to the electrical resistance as:

$$\left(\mathrm{T_{hot}}\text{-}\mathrm{T_a}\right) = \frac{\left(\mathrm{R_h}\text{-}\mathrm{R_0}\right)}{\mathrm{R_0}\beta} \tag{4-2a}$$

$$k = \frac{1}{\alpha R_0} \tag{4-2b}$$

where k is a constant that contains α (Temperature Coefficient of Resistance or TCR) and R_o, which is the initial electrical resistance of the heater. R_h is the electrical resistance of the heater at the elevated temperature and C is an unknown constant.

Combining Eqs. (4-1) and (4-2) leads to:

$$R_h = \underbrace{\frac{R_m^{Th}}{k}}_{Slope\,(M)} Q_h + \underbrace{\frac{-C + T_a}{k}}_{Const} \tag{4-3}$$

Multiplying the slope (M) of the R_h versus Q_h curve by k thus yields $R_m{}^{Th}$. This is the general technique used to measure $R_m{}^{Th}$.

Inside $R_m{}^{Th}$ are many terms, but the end goal is to measure $R_{DUT}{}^{Th}$ to know the thermal properties of the sample in question. In order to characterize all the terms present in Fig. 4—3a the full characterization is performed in different steps. To characterize the leg resistance, measurement is initially done without a sample between the islands, as shown in Figure 4—2b. The thermal resistances at this stage are schematically shown in Figure 4—4a. To clarify, the value of $R_m{}^{Th}$ in this state (the state of cut) will be referred to by $R_{m,cut}{}^{Th}$, as shown on the right-hand side of Figure 4—4a, and the corresponding reading of the slope in Eq. (4—3) is dubbed $M_{m,cut}$.

At this same step, while there is no sample between the islands, the sink resistance, $R_{sink}{}^{Th}$, can be also determined. If power is applied to the cold island, Q_c, then the sink resistance can be determined in a manner similar to that by which R_h is determined in Eq. (4—3).

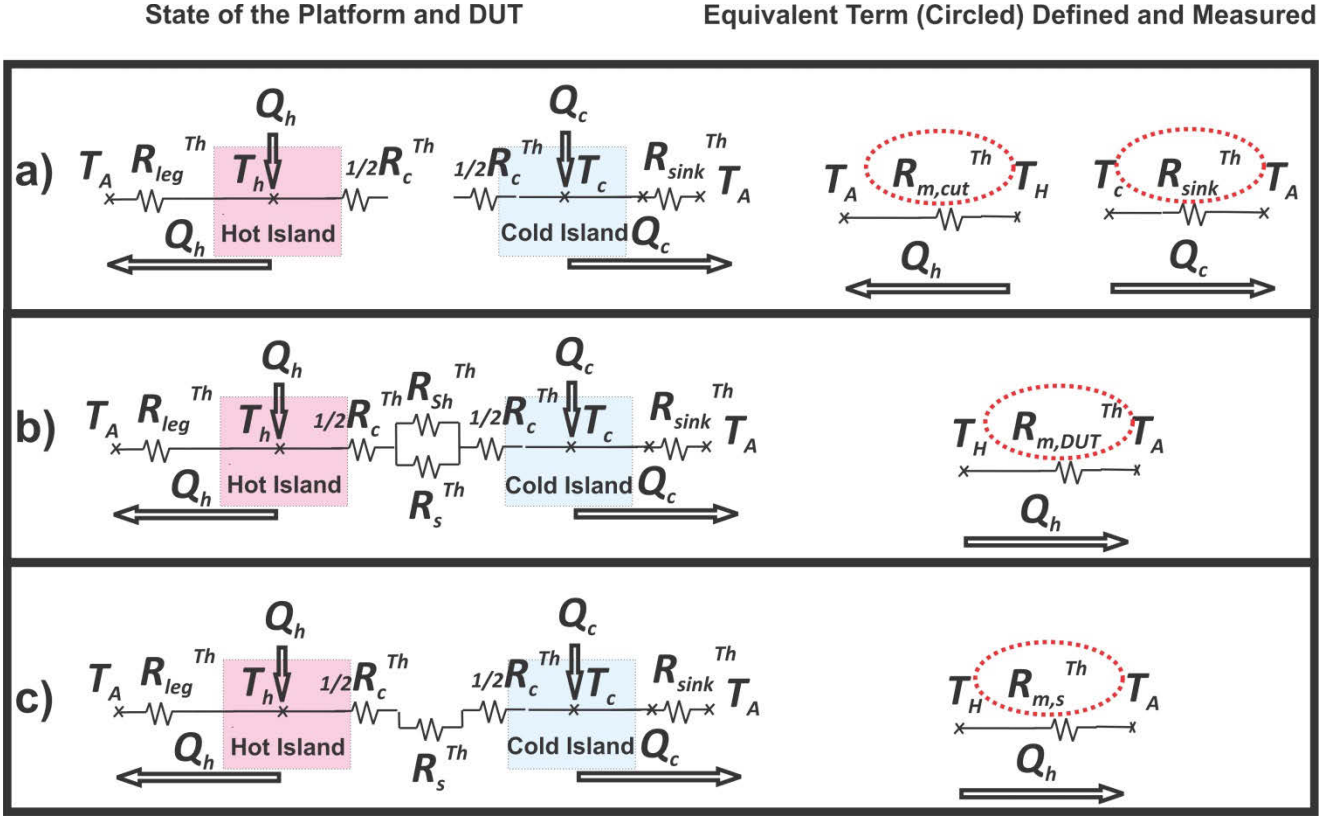

Figure 4—4: Three steps of measurement to isolate the thermal resistance of a sample from competing thermal resistances. a) When everything is cut between the hot and the cold islands the thermal resistance of the legs and of the sink can be found (state of cut). b) The sample and a 'short' connect the hot and cold islands (state of DUT). With the short between the two islands the contact resistance of the sample to the hot and cold islands can be determined. c) When the short path is removed from the bridge between the hot and cold islands (state of sample).

To evaluate R_{DUT}^{Th}, and R_c^{Th}, two more independent measurements are needed. For this purpose, the DUT is fabricated in the form of two parallel resistors from the same piece of material with a known geometric relationship. Because nano-scale samples often have idiosyncratic values of thermal

conductivity, it is important that the parallel thermal resistors be made from a single piece of material as to not incorporate additional unknowns. One such fabricated DUT is shown in Figs. 4—5 and 5—6. Fabrication of such a DUT is described later in this article. The shape of the DUT is chosen such that one of the paths has a lower thermal resistance (short path, R_{sh}^{Th}) compared to the other (the long or sample path, R_s^{Th}). Based on the geometry of the DUT, the relationship between the resistors is also known:

$$R_{\mathrm{s}}^{\mathrm{Th}} = rR_{\mathrm{sh}}^{\mathrm{Th}} \tag{4-4}$$

where r is a known parameter and depends on the geometry. Therefore the measurement of the thermal resistance between the hot island under the state of DUT is considered $R_{m,DUT}^{Th}$ as described system in Fig. 4—4b. The related slope in Eq. (4-3) is also called $M_{m,DUT}$. By cutting the short path with a FIB, the thermal resistances of the contacts and the sample under test can be determined according to Fig. 4—4c. The thermal resistance between the hot island and the ambient temperature at this point (the state of sample) is called $R_{m,s}^{Th}$. Consequently, the measured slope in Eq. (4-3) is called $M_{m,s}^{Th}$. Finally, the exact thermal resistances of the sample and contact are:

$$R_s^{Th} = \left(\frac{r+1}{r}\right)\left[\left(\frac{1}{R_{m,s}^{Th}} - \frac{1}{R_{m,cut}^{Th}}\right)^{-1} - \left(\frac{1}{R_{m,DUT}^{Th}} - \frac{1}{R_{m,cut}^{Th}}\right)^{-1}\right] \tag{4-5}$$

$$R_c^{Th} = \left(\frac{1}{R_{m,s}^{Th}} - \frac{1}{R_{m,cut}^{Th}}\right)^{-1} - R_{\sin k}^{Th} - R_s^{Th} \tag{4-6}$$

where $R_{m,s}^{Th}$, $R_{m,DUT}^{Th}$, and $R_{m,cut}^{Th}$ are three independent measurements according to the states explained in Fig. 4—4.

The uncertainties corresponding to the measured parameters of $R_{m,cut}{}^{Th}$, $R_{m,DUT}{}^{Th}$, $R_{m,s}{}^{Th}$ are assessed by repeating the measurements more than 10 times and applying the Student's t-distribution. The uncertainty on the parameter *r* and the geometry is determined by the limitations on the resolution of the SEM employed in this work.

4-4 Experimental Procedure

To measure the thermal conductivity of a DUT, the platform is characterized and then the sample and its contact resistances are measured. The characterization of a platform includes the measurement of $R_{leg}{}^{Th}$ and $R_{sink}{}^{Th}$, and the thermal electrical properties of the serpentine patterns. Next, a DUT is transferred using an Omniprobe and attached to the stages using FIB and a GIS. Finally, the sample is studied through the three aforementioned steps to attain the thermal resistance solely due to the sample.

To determine the effect of convection on the platform, curves of the electrical resistances versus power are determined at several different pressures. It is determined that for pressures below approximately 1 mTorr, negligible changes occur in the measured thermal resistance. All experimental values reported in this article were taken at a pressure of 10 μTorr or below to avoid error-inducing effects due to convection (See Fig. 4—5).

The thermal electrical behavior of the platinum is assessed using a calibrated hot plate in a high vacuum environment. For different temperatures of the hot plate, the electrical resistances are measured using a low current that does not induce self-heating for the device. Self-heating occurs when the relationship between resistance and power becomes nonlinear. The currents are also reversed and the mean of the recorded voltages and currents are used. This process leads to the study of the temperature-electrical resistance curve based on Eq. (4-2) at a low power of 10 μW. After characterizing the resistance-temperature curve the platform is tested to attain its leg resistance. To calculate the thermal resistance of the DUT, the measurement is performed by applying different powers and measuring the electrical resistances on the hot island. The temperature on the cold island remains constant even with the highest powers used.

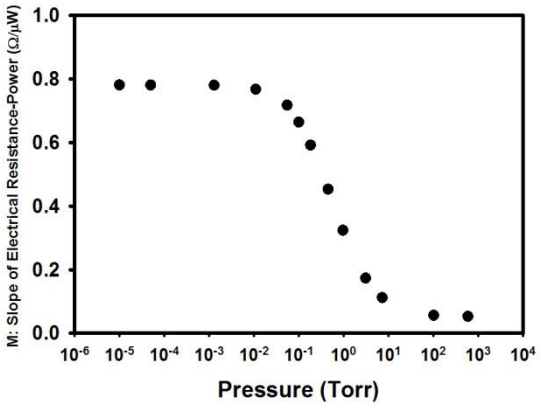

Figure 4—5: The slope of electrical resistance-power curve at different pressures. The plot shows that at pressures below 1 mTorr the value saturates.

A thin film is initially trimmed to the shape needed, and then it is transferred and welded to the hot and the cold islands. As shown in Fig. 4—6a, transferring a sample is performed by welding an Omniprobe to a part of the sample. Then it is transferred to the platform and put on the bonding stages (see Figs. 4—6b and 4—6c). While the sample is being held in place by the Omniprobe, it is welded to the stages using the FIB and GIS (see Fig. 4—6d). Finally, the Omniprobe is cut by the FIB, and the sample remains attached to the platform. All of these steps are followed in transferring any new sample to the platform, and old samples are moved away in a similar fashion.

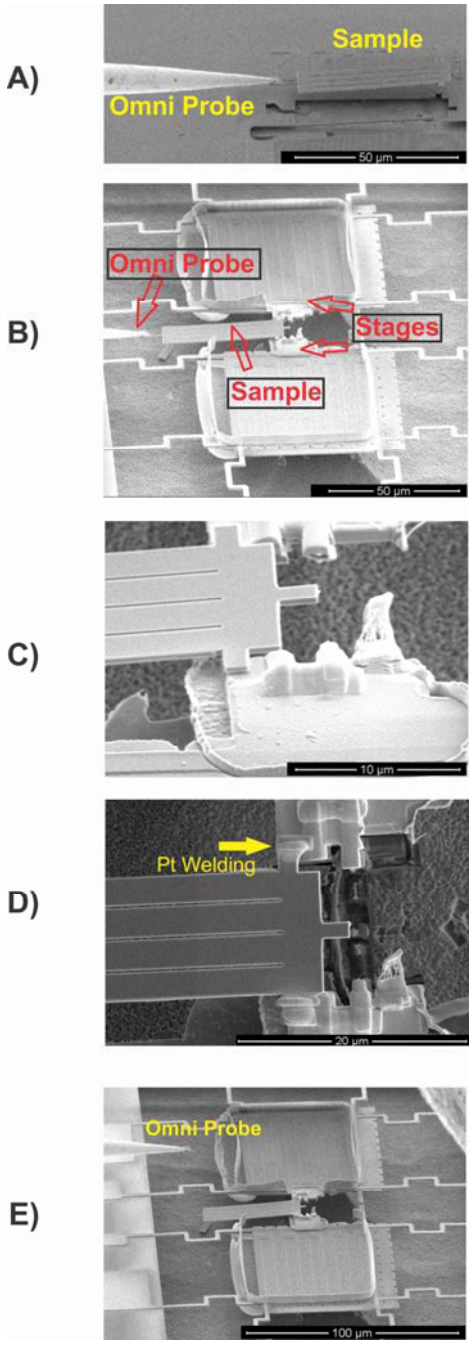

Figure 4—6: SEM images showing the experimental procedure for measurement of a typical sample. a) Cutting the DUT and welding it to the Omni Probe by FIB and GIS, b) Transferring the sample to the platform, c)

Placing the DUT on the sample pads, d) Welding the DUT to the pads, e) Detaching the Omni Probe from the sample and retracting it.

To assess the contact resistance, as explained in Section III, the DUT's configuration is that of two parallel resistors, see Fig. 4—4b. To experimentally attain this geometry, the thin film samples are transferred with a U or W shape with a short and a long path (see Figs. 4—6 and 7). The shape of the sample is chosen such that one of the paths has a considerably lower thermal resistance (short path) than the other (the long or sample path). Using the geometry of a DUT, the ratio *r* in Eq. (4-4) is determined. Figs. 4—7a and b show how to experimentally change the two thermal states of the DUT shown in Figs. 4—4b and c. To make the transition between these states, the short path is cut by the FIB after thermal measurement of the DUT. In Figure 4—7a, the DUT has both short and sample path resistances in parallel, which corresponds to the state of DUT shown in Fig. 4—4b. In Fig. 4—7b, a cut is made on the short path such that only the sample path resistance is thermally relevant. This state also corresponds to Fig. 4—4c. Finally, the corresponding thermal measurements are used in Eq. (4—5) to attain the thermal resistance of the sample.

The process of cutting and imaging using FIB can potentially change the thermal conductivity of a sample. It potentially can damage a sample by Ga^+ bombardment [10]; this damage is dependent on the sample material and the dose received by the sample. Generally, damage/contamination with Ga^+ is to be avoided. To minimize this damage, a minimal ion current of 30 pA is used for cutting. Moreover, while transferring the DUT, imaging with the FIB is also kept to a minimal time on the

order of few seconds. To evaluate if damage occurs during this process, one of the Si sample was imaged for 5 minutes at 30 pA. This is on the order of 100 times longer than a sample is typically imaged. Measurements of thermal resistance before and after this intentional damage showed no difference within the experimental error. Moreover, some additional parts of the sample were milled by the FIB and again no change in thermal resistance was detected. Accordingly, to the best knowledge of the authors this process did not induce a detectable damage to the samples in this work.

After measurements, the DUT is removed and another sample is mounted. In Figures 4—6c and 2b, it is seen that the platform presented in this article has been used for several measurements. The processes of mounting and demounting deposit a very thin layer of FIB deposited platinum on the island, as shown in Figure 4—2b, and after repeating this process, this film could theoretically change the properties of the sensors. However, because the current design features a thick layer of AlN, the thermal electrical properties of the sensors are preserved.

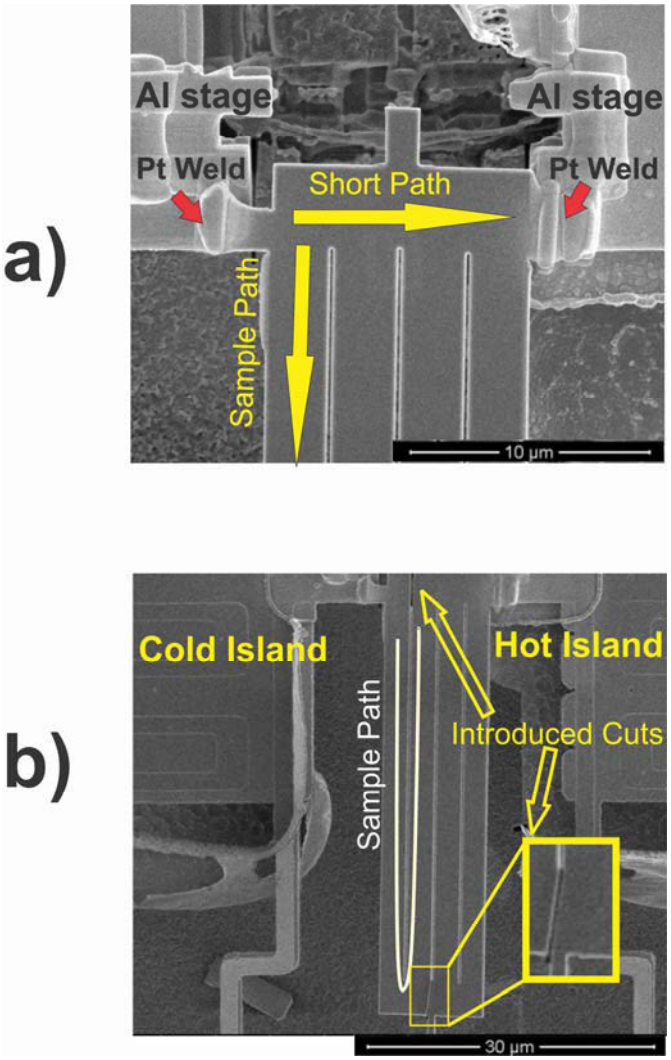

Figure 4—7: To measure the contact resistance a sample has a short and a sample path. a) The short sample path is dominant. b) After making cuts by FIB, the long (serpentine) sample path is dominant.

4-5 Results and Discussion

Four different samples are studied on a single fabricated platform: two Si films and two SiN_x films. Details of the films are as follows: one Si thin film from an SOI wafer with a thickness of 260 nm,

another Si sample with a thickness of 500 nm, and two silicon nitride samples namely $SiN_x(1)$ and $SiN_x(2)$, taken from the same wafer are thermally studied. Furthermore, $SiN_x(2)$ after the first measurement is demounted, remounted and characterized again to assess the repeatability of the process. The result for the second characterization is referred to as $SiN_x(2R)$. The silicon samples with thicknesses of 260 nm and 500 nm are doped with boron and phosphorous, exhibiting an electrical resistivity of 0.18 and 0.5 Ω-m, respectively. Additionally, the wafer for the silicon sample with a thickness of 500 nm was previously characterized in an independent effort with a different experimental method [76]. The agreement between the current measurements and the previous reports verifies the introduced technique.

In the calibration process, the TCR values of 0.00147 and 0.00149 K^{-1} are found for the hot and cold islands, respectively, and reported in Table 4-1. These values are very close to other reports of the TCR of platinum at room temperature [77], which is 0.0014 K^{-1}. They are also close to the reported range of 0.0018 K^{-1} to 0.0036 K^{-1} for the platinum serpentine patterns in other work[67]. Differences between the reported TCR values and the current work are likely due to the effects of the thickness of the films, adhesive layer of Ni, purity of the deposited platinum, stress in the film, and variation in temperature. The summary of the calibration , presented in Table 4-1, is used for the subsequent calculations.

Table 4-1: Summary of the characterization results for the hot and cold islands used in this work.

	Number of Tests Repeated	k (K/Ω)	α (K^{-1})	Uncertainty of k and α
Hot Island	12	0.933	0.00147	±2%
Cold Island	12	0.828	0.00149	±0.5%

The results for the three samples measured in this work are reported in Table 4-2. These values are in agreement with previous reports. The thermal conductivity attained for the amorphous LPCVD SiN_x (i.e. $SiN_x(1)$) is measured 2.85 W/mK, which is very close to 3 W/mK previously reported for 500 nm-thick SiN_x [78]. The thermal conductivity of the Si slab with the 260 nm thickness is measured 72 W/mK. This value agrees with the previously reported thermal conductivity for silicon ranging from 70 to 100 W/mK [79, 80]. The 500 nm thick silicon slab has a measured thermal conductivity of 97 W/mK. The sample was taken from a wafer previously characterized in another work [76] that measured a thermal conductivity of 104 W/mK on average. The small difference between the measurements can be attributed to the small inherent difference between the density of defects on different areas of a wafer, small geometric differences between samples, and the errors in the measurement techniques.

Another important result in Table 4-2 is the measured contact resistance. The contact resistance values for the silicon samples are within 25% of one another. The area of contact and quality of the Pt weld appear to be similar. Thus, it seems reasonable to assume that the contact resistance would

be on the same order of magnitude. However, the discrepancy is 0.4 (K/μW), and making an assumption that the contact resistance for one sample would be the same for another is erroneous. The contact resistances in this work are also on the same order of the magnitude of the results reported elsewhere[73], even though the similarities between the samples and methods in the current and that work are minimal. In Table 4-2, it can be seen that the contact resistances can be greater than the thermal resistance of the sample. However using the framework presented, they can be accounted for in the thin films studied. Overall, Table 4-2 shows that, using this framework, different samples with very large thermal contacts can successfully be characterized, and consistent results are attained after reusing the platform.

Table 4-2: Summary of measurements on three different samples

	$M_{m,cut}^{Th}$ (Ω/μW)	$M_{m,DI}^{Th}$ (Ω/μW)	M_{ms}^{Th} (Ω/μW)	R_s^{Th} (K/μW)	R_c^{Th} (K/μW)	r	k(W/mK)
SiNx(1) 1000 nm thick	0.971±0.06%	0.884±0.3%	0.933±0.3%	12.33±10%	9.92±4%	14	2.85±11%
Si 260 nm thick (100)	0.971±006%	0.691±0.3%	0.791±0.8%	1.67±10%	2.25±3%	28	72±11%
Si 500 nm thick (100)	0.971±0.06%	0.642±0.06%	0.769±0.03%	1.80±3%	1.82±3%	21	97±4%

The contact resistance cannot be controlled ideally in the processes of depositing Pt with the GIS. However, it is calibrated accurately, and the technique is independent of the type of material, geometry, quality of welding, etc. According to the results it is typically higher than 1 K/μW. This value is on the same order of thermal resistance of the actual Si sample. This provides estimations to

the thermal resistance of the contacts. By measuring several known samples it is proven that a contact resistance, as large as that of the sample, can be calibrated out, and consistent results are attained.

Repeatability of the characterization of a unique sample was also studied. For this purpose another sample of silicon nitride, $SiN_x(2)$, was characterized twice. This sample had a different geometry (see Fig. 4—8b) from that of $SiN_x(1)$. This sample was characterized with the aforementioned steps and then demounted, remounted and characterized again, see Fig. 4—9a to 4—9d. The remounted sample is dubbed $SiN_x(2R)$, and the results are reported in Table 4-3.

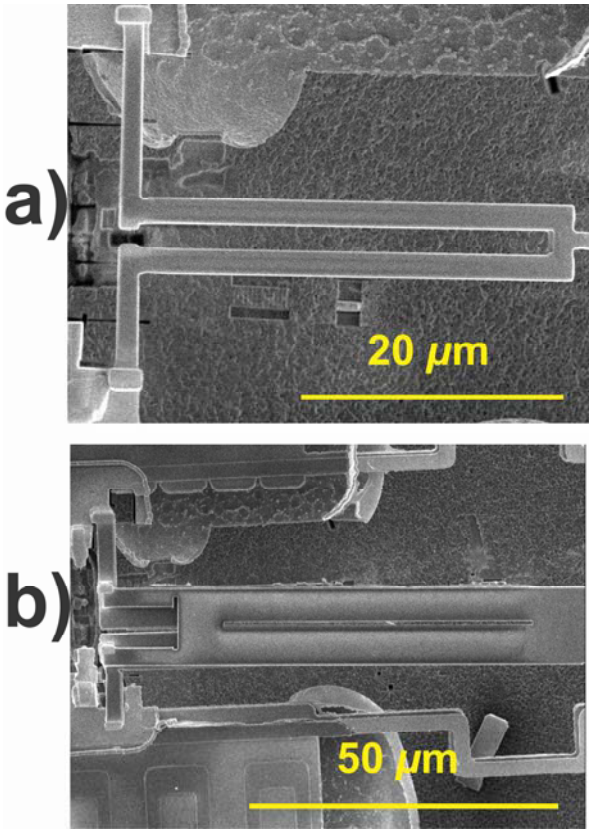

Figure 4—8: Samples of SiN_x from the similar wafer with different geometries a) The first measurment of silicon nitride $SiN_x(1)$, b) the second sample of silicon nitride $SiN_x(2)$ which is mounted and measured twice.

Before transferring the $SiN_x(2)$, an extension to the stage is made by transferring and welding a Si sample to the Al stage on the platform. After that the $SiN_x(2)$ is transferred and welded on the intermediate the Si stage. This stage makes the contact resistance more complicated but in this framework all the unfavorable resistances in the sample resistance are taken into account. Fig 4—7b, shows the $SiN_x(2)$ sample connected to the platform through the Si stage. This figure shows the state of DUT before the measurement of R_{DUT}^{Th}. The welding between the Si stage and $SiN_x(2)$ at

this point is shown in Fig. 4—8a. The summaries of the $SiN_x(2)$ sample after full characterization are reported in Table 4-3. Fig. 4—8b shows the process of demounting $SiN_x(2)$ by cutting the edge of the welded area. Fig. 4—8c also shows the same area when the sample $SiN_x(2)$ is fully demounted and the bare Si stage is evident. Fig. 4—8d shows the same sample welded again on the Si stage on a different location. At this point the SiN_x sample is the same sample namely $SiN_x(2)$ previously at the state of the sample (see Fig.4—4c), and now it is remounted on the stage, which is called $SiN_x(2R)$. Thermal resistance of $SiN_x(2R)$ is characterized again and reported in Table 4-3 to be compared with the previous results before demounting.

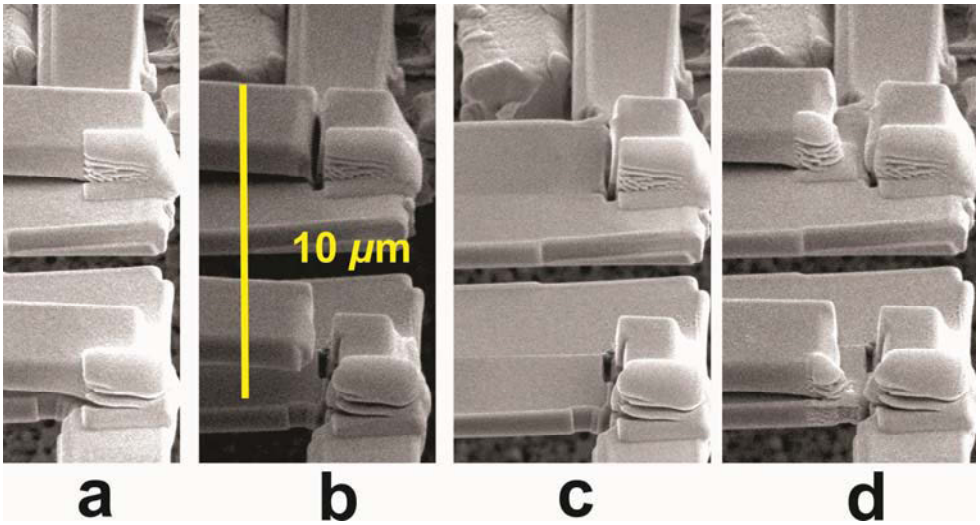

Figure 4—9: The welding joint of the sample $SiN_x(2)$ when: a) the sample is initially mounted, b) the sample is detached from the stage, c) the sample is fully demounted, d) the sample is mounted on the stage again at a slightly different position.

Table 4-3: Summary of measurements on SiNx with repetition of the measurement

	$M_{m,cut}^{Th}$ (Ω/μW)	$M_{m,DUT}^{Th}$ (Ω/μW)	M_{ms}^{Th} (Ω/μW)	R_s^{Th} + (K/μW)	R_s^{Th} (K/μW)	R_c^{Th} (K/μW)	k(W/mK)
SiNx(2) 1 μm thick	0.987±0.3%	0.872±0.3%	0.9304±0.3%	14.47±3%	7.37±3%	7.102±3%	23 2.85±3%
SiNx(2R) 1 μm thick	0.987±0.3%	NA[1]	0.9299±0.2%	14.33±3%	NA[2]	6.96±3%[3]	NA[1] 2.80±3%[4]

[1]: Since in the second step for the $SiN_x(2)$ the short path in the DUT is already cut, measurements on R_{DUT}^{Th} and r are not applicable in the second characterization (i.e SiNx(2R)).

[2]: In the second measurement only $R_s^{Th}+ R_c^{Th}$ can be measured directly.

[3]: Considering R_s^{Th} unchanged from SiN_x (2) to SiN_x (2R), based on the readings in this step R_c^{Th} is calculated.

[4]: Considering R_c^{Th} unchanged from SiN_x (2) to SiN_x (2R), based on the readings in this step the thermal conductivity is calculated.

Even though $SiN_x(1)$ and $SiN_x(2)$ have different geometries (see Figs. 4—8a, 4—8b) both show the same thermal conductivity of 2.85 (W/μK) according to Table 4-2 and Table 4-3. This is an expected result since both samples are taken from the same wafer. The sample $SiN_x(2R)$ is already at the state of sample, and its R_{DUT}^{Th} cannot be remeasured again. Therefore one unknown is missing and both R_s^{Th} and R_c^{Th} cannot be characterized directly. However measurement at this state can directly result in $R_s^{Th}+ R_c^{Th}$. The comparison made between the $SiN_x(2)$ and $SiN_x(2R)$ shows

that the sums of the resistances (R_s^{Th}+ R_c^{Th}) are 14.47 K/μW and 14.33 K/μW, respectively. These measurements show a difference about 1.4%, which is smaller than 2% error bar on the measured values. At this point it is unknown whether the source of difference is the contacts or actual changes in the sample due to processing. However it is evident that the sum of these errors combined is about 1% to 2%. Therefore for the same sample of $SiN_X(2)$ the thermal resistances are repeatable after remounting within the reported error bar.

One reasonable assumption is that the thermal resistance of sample paths of $SiN_x(2)$ and $SiN_x(2R)$ are the same, but the contact resistances are different. Under this assumption, the contact resistance of the $SiN_x(2R)$ can be calculated as well , see Table 4-3. Now the comparison shows about 0.2 K/μW difference (3%) in the thermal resistance of the contacts. This difference is observed between the contacts depicted in Figs. 4—9a and 4—9d. This comparison indicates the order of repeatability for mounting a unique sample on the same platform. Arguably, one might assume the contact resistance is unchanged and recalculate the thermal conductivity. Using this assumption, the thermal conductivity is 2.8 (W/mK), as reported in Table 4-3. This new value again shows less than 2% difference with the previous calculations of the thermal conductivity of silicon nitride. It indicates that even if all the erroneous effects of unrepeatability are projected into the thermal conductivity measurement, the reading is still valid within the reported error bar. The change in the contact resistances when different samples are studied is about 0.6 W/μK (according to Table 4-2), much greater than the case of the remounting the same sample (0.2 W/μK according to Table 4-3). It is an

indication that the properties of a thermal contact on this platform depends strongly on the materials and the geometry rather than the amount of Pt deposited to form a contact.

4-6 Conclusion

A microfabricated device and the corresponding technique were introduced to measure the thermal conductivity of thin films with the aid of a focused ion beam, a micro-probe manipulator (Omniprobe), and a gas injection system. The device was based on a previously conceived technique wherein silicon nitride suspended islands are utilized. In this technique, the thin film sample was cut using the focused ion beam, transferred by the Omniprobe to the device, and fastened to the device by the deposition of Pt using the gas injection system and FIB. A framework was introduced and employed to characterize unknown thermal resistances of the contacts between the sample and the device. Four different samples were thermally characterized on the same device and the results were consistent with measurements performed using other techniques previously reported. Remeasurement of different samples from the same wafer showed less than a percent difference in the thermal conductivities. One of the samples was also mounted, characterized, demounted, remounted and characterized again to evaluate the repeatability of the process of welding and measurement. A change of 0.2 K/μW in the thermal conductivity of the contact was observed, which indicates an acceptable degree of repeatability of the process of transferring. It was observed that if different Si samples are mounted the change in the thermal resistance of the contacts can be as great as 0.6 K/μW. The comparison between different measurements proved that the

technique is repeatable, and precise; the platform is reusable with consistent results even when the erroneous thermal resistance of the contacts was greater than that of the sample.

5 Remarks on thermal characterization

Pt deposited by focused ion beam (FIB) is a common material used for attachment of nanosamples, repair of integrated circuits, and synthesis of nanostructures. Despite its common use little information is available on its thermal properties. In this work, Pt deposited by FIB is characterized thermally, structurally, and chemically. Its thermal conductivity is found to be substantially lower than the bulk value of Pt, 7.2 W/m-K vs. 71.6 W/m-K at room temperature. The low thermal conductivity is attributed to the nanostructure of the material and its chemical composition. Pt deposited by FIB is shown, via aberration corrected TEM, to be a segregated mix of nanocrystalline Pt and amorphous C with Ga and O impurities. Ga impurities mainly reside in the Pt while O is homogeneously distributed throughout. The Ga impurity, small grain size of the Pt, and the amorphous carbon between grains are the cause for the low thermal conductivity of this material. Since Pt deposited by FIB is a common material for affixing samples, this information can be used to assess systematic errors in thermal characterization of different nanosamples. This application is also demonstrated by thermal characterization of two carbon nanofibers and a correction using the reported thermal properties.

All the materials in this chapter are reproduced with permission from another report [81]. The chapter is a modified version of that report. © 2015 IOP Publishing Ltd.

5-1 Introduction

Deposition of metals or insulators by focused ion beam (FIB) has been a technique utilized for more than two decades. This technique has been proven to deposit a line width of deposition as small as 100nm [82] for ion assisted chemical vapor deposition of different materials such as gold [83], platinum [71], tungsten [84] and SiO_2 [82]. Even though the technique is relatively expensive, it is very useful due to its ability to deposit different materials in sophisticated three-dimensional structures [82, 85]. At high resolution with a beam spot size as small as 5-7nm [86], this technique can open even more opportunities for nanofabrication.

Platinum is one of the more typically deposited materials due to its relatively high deposition yield [84]. FIB deposited platinum is commonly used to prepare micro/nanosamples for use: in analytical instruments [43, 87] , to fix or 'weld' a sample to a testing apparatus [88], or as a protective layer [87]. When the goal of Pt deposition is for fixing or protecting a sample, the deposition yield becomes a substantial portion of the total cost. Accordingly the deposition yield of platinum and its line width resolution have been studied previously [71, 84].

In addition to the aforementioned applications, FIB deposition of Pt is also applicable in the integrated circuit (IC) industry. Examples of its use are: repairing photolithographic masks [89], frequency tuning of resonators [90], and repairing IC chips [91]. Due to its use in these applications the electrical properties of platinum deposited by FIB were also recently studied [71, 92] . These

studies showed that the electrical resistivity of the FIB deposited platinum is more than three orders of magnitude higher than the bulk value [84], which was attributed to the high amount of carbon in the platinum film [71, 93].

Increasingly, platinum deposited by FIB or e-beam is used for the characterization of nano-materials. One new application is attaching nano/micro samples to MEMS devices for the characterization of thermo-physical properties such as thermal conductivity [67]. Numerous studies using this technique of 'micro-welding' show the growing importance of this application [68, 94-97]. Although researchers have studied the thermal conductivity of nano/micro structures affixed to measurement devices by FIB deposited platinum [15, 98], the thermal conductivity of these FIB deposited platinum films is still uncharacterized. A direct measurement of the thermal conductivity for FIB deposited platinum has the potential to remove or reduce erroneous effects in many measurements involving this material for the purpose of micro-welding [67, 95, 98].

In addition to the previous applications for the platinum deposited by FIB, it is very promising for fabrication of new nanomaterials and metamaterials. For instance three dimensional phononic crystals with spacing of few nm is predicted to feature extremely enhanced thermo-physical properties [99]. Furthermore, fabrication of metamaterials such as photonic crystals with Pt has been demonstrated, which requires nano-resolution fabrication [100]. However, to engineer such micro/nanostructures fabricated from the FIB deposited platinum, its thermal properties must be characterized.

In this work, the thermal conductivity of Pt deposited by FIB is characterized, its correlation with the Pt nano-structure is discussed, and its effect on the accuracy of other measurements is demonstrated. For thermal characterization, a general method is employed to measure the thermal conductivity of FIB deposited materials. The general technique utilizes suspended SiN_x membranes [67]. In the current study, the in-plane thermal resistance of a SiN_x thin film is characterized before and after deposition of platinum in three steps. Determining the thermal conductivity of the FIB deposited platinum is based on an analysis of the change in thermal resistance of a sample after deposition of the material. Results are interpreted through examination of the FIB deposited platinum's material composition, atomic structure, grain size, and prior reports. Finally, in order to demonstrate the utility of the aforementioned results, two carbon nano-fibers are affixed using the FIB deposited Pt and thermally characterized; this is a very common method employed by many investigators [30, 67, 68, 94, 95, 97]. This case study demonstrates the erroneous effects of FIB deposited Pt on the thermal characterization of carbon nanofibers. This approach can be used to verify the accuracy of the aforementioned studies as well as future ones on thermal properties of nanofibers, nanotubes, and nanostructured samples.

5-2 Measurement Technique

The thermal conductivity of a sample is determined using a 1-D technique wherein the sample is placed between a hot and a cold island [30, 67, 98]. The authors' rendition of this technique allows

measurement of different micro/nano structures on a single platform, which minimizes systematic errors. Details of this technique can be found elsewhere [30]. An example of the measurement platform used for this technique is shown in Figure 5-1. The two SiN_x membranes have platinum serpentine patterns acting as both heaters and temperature sensors. A SiN_x sample is transferred to the platform with the aid of an Omniprobe, and it is then micro-welded in place with FIB deposited platinum. Note that this initial deposition of platinum does not affect the final measurement since its effect is accounted for in the calibration process [30]. Next, its thermal resistance is measured under vacuum. The platform used for characterization is the same platform previously used by the authors to characterize two silicon films (500 nm and 260 nm thick) and a silicon nitride thin film. This platform has also been used in other work by the authors to measure the thermal resistance of a 1D Phononic Crystal [98].

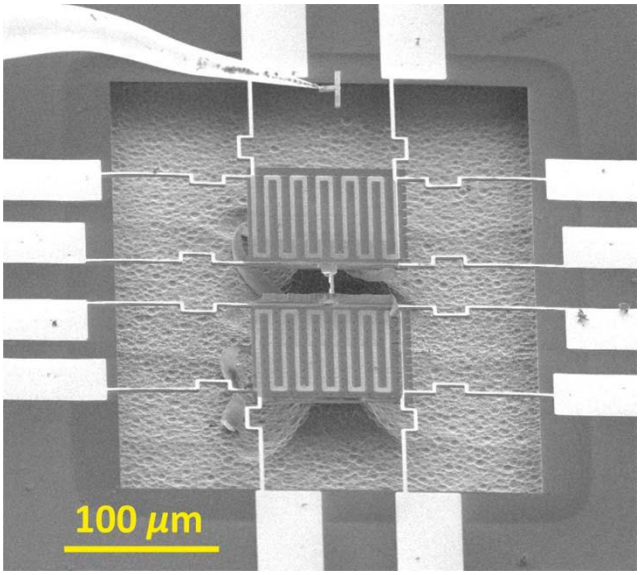

Figure 5—1: A typical platform for measuring a sample's thermal resistance. It is comprised of two platinum serpentine patterns (heater/sensors) with a sample placed between them. An Omniprobe™ (needle in upper left-hand corner) is used for precise placement of the sample.

Figure 5—2a shows a U-shaped sample of silicon nitride transferred and attached to the platform. Both the thermal resistance of the contacts between the sample and the device and the thermal resistance of the U-Shape sample are measured separately. In this first step the thermal resistance of the transferred SiN_x sample is measured, and its thermal conductivity is calculated to be 2.9 W/m-K. This thermal conductivity value is similar to results reported in the authors' prior work [30] and consistent with other reports [78]. In the second step 1100 nm of FIB deposited platinum is deposited on a portion of the silicon nitride sample, see Figures 5—2 b and c. Figure 5—2b shows

the part of the SiN_x sample being exposed to FIB for deposition of Pt. For consistency, each platinum deposition used a 30kV accelerating voltage and a nominal 30 pA current. The actual current was measured to be 290 pA using a faraday cup. The key parameters of the current and voltage chosen in this work provide patterning with a good compromise between the resolution and yield in deposition of platinum. The precursor for the FIB deposited platinum was $(CH_3)_3Pt(C_pCH_3)$. At the end of Step 2, the thermal resistance of the sample is measured again and the contribution of the SiN_x sample with 20 μm of its length covered with 1100 nm of FIB deposited platinum is assessed. In step three a 500 nm thick layer of FIB deposited platinum is placed on top of the initial 1100 nm layer. At the end of this step, two distinct layers of platinum are observed on the SiN_x sample, see Figure 5—2c. Once again the thermal resistance of the sample on the characterizing platform is measured, and the thermal resistance attributed to the bar consisting of SiN_x and two Pt layers is calculated. The results from these three steps are used to study the contribution of the FIB deposited platinum to the sample's thermal resistance.

A TEM sample of FIB deposited platinum is prepared and examined in two different TEMs. The TEM sample is prepared using the FIB/lamella technique [101]. It was subsequently inspected using an FEI Image Corrected Titan G^2 60-300ST and Titan G^2 60-300CT. The Image Corrected Titan G^2 60-300ST was used to take aberration corrected images of the FIB deposited platinum to inspect its atomic structure. A Titan G^2 60-300CT equipped with an EDS and GIF Tridiem^{TM} was used to create elemental maps of the FIB deposited platinum.

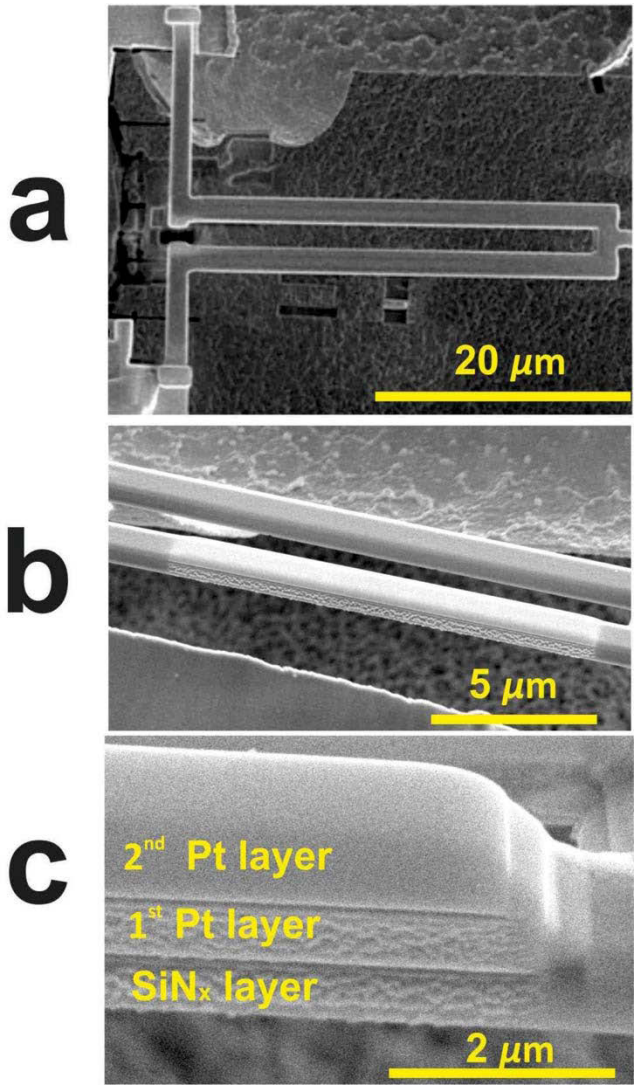

Figure 5—2: a) The U-shaped silicon nitride sample placed on the platform in step 1, b) Platinum being deposited on 20 μm length of SiN_x with a 1100 nm thickness in step 2, c) Side view of the final sample at the end of step 3 where two distinct layers are present: FIB deposited platinum (2 layers) and the SiN_x substrate (part of the U-shaped structure).

5-3 Characterization and Discussion

In the first step (Figure 5—2a) a thermal resistance of 3.42 K/μW for SiN_x is measured when there is no Pt present. This value corresponds to a thermal conductivity of 2.9 W/mK for SiN_x, which is confirmed in other investigations [30]. In the second step (Figure 5—2b), 1100 nm platinum is deposited by FIB, and the thermal resistance of the sample decreases to 1.84 K/μW. If the interface between SiN_x and the deposited platinum is perfectly conductive, it could be expected that the thermal resistance of the sample is the sum of two thermal resistors in parallel. However, since they are dissimilar materials (SiN_x / FIB deposited Pt), it is assumed that there is an unknown interfacial resistance. A possible damage due to the Ga^+ impinging on SiN_x in the beginning of the deposition contributes to this interfacial resistance. In the third step (Figure 5—2c) a second layer of platinum is deposited. The thermal resistance drops again; this time to 1.16 K/μW. Since the interface, at this stage, is between similar materials (*i.e.* FIB deposited platinum/FIB deposited platinum), the interfacial thermal resistance between the films present in steps 2 and 3 is considered negligible. Therefore it is assumed that the layer of platinum added in Step 3 acts as a thermal-resistor in parallel with the composite sample comprised of SiN_x and the platinum present in the end of step 2. The irregularities in the shape of the added Pt (length and cross sectional area), and the uncertainty in the measurement of the thermal resistance of the added Pt both contribute to the uncertainty in the calculated thermal conductivity. Using these assumptions the thermal conductivity of the FIB deposited platinum added in Step 3 is calculated to be 7.2 ± 40% W/m-K.

Boundary resistance between SiN_x and Pt in this work is another parameter useful future reference. To estimate it a finite element analysis (FEA) is used. The simulation is performed using ANSYS which features a 3D model with cubic 8 nodes elements with about a million degrees of freedom. In the FEA three different layers of a SiN, a 20 nm thick unknown material serving the function of boundary resistance, and the FIBed Pt with the thickness reported in Step 3. Thermal conductivities of the Pt and SiN are opted as the values measured in the previous step. The thermal conductivity of the unknown interfacial material was a fit parameter to match the exact thermal conductivity measured in the final stage. This fit parameter with the thickness of the layer is used to calculate the boundary resistance. Furthermore slight irregularities on the edges are employed the numerical model to include effects of Pt overspill by FIB. Using the limits of the measured thermal conductivity of the FIB deposited platinum and a finite element analysis the interfacial resistance between deposited material and the silicon nitride is estimated to range from 0.05×10^{-6} to 1×10^{-6} (Km^2/W). In the initial stage of the FIB exposure the materials milled is negligible comparing with the 1 micron thickness of SiN. Accordingly damaging the surface by FIB mainly contributes to this high boundary resistance rather than the calculated thermal conductivity of Pt.

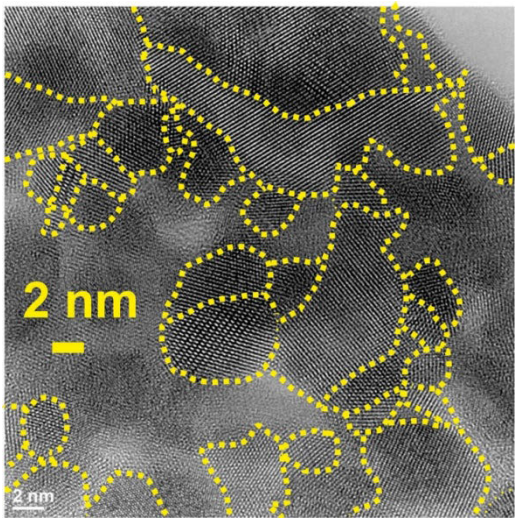

Figure 5—3: Aberration corrected TEM image of the Pt deposited by FIB shows a polycrystalline structure and an amorphous phase. The polycrystalline structure is Pt with an average grain size of 4 nm and the amorphous structure is primarily carbon.

The thermal conductivity of the Pt deposited by FIB is substantially lower than platinum's bulk value of 71 W/m-K [77] and the thin film value of 30 W/m-K for platinum deposited by thermal evaporation [77]. Clearly, a possible reason for the discrepancy could be the high amount of carbon and gallium in the deposited material [71]. Moreover, prior work suggested that the platinum deposited by FIB is amorphous [71]. To better understand the reasons for the low thermal conductivity of the film, a film of FIB deposited platinum was also studied by aberration corrected TEM, see Figure 5—3. In this figure the yellow dashed line indicates the borders of the nanocrystals.

Although an amorphous structure was previously suggested for this material [71] in some earlier reports, TEM images gathered in this work display a polycrystalline structure with an average grain size of approximately 4 nm based on statistical analyses [102]. Such a nanocrystaline structure is consistent with the newer work reporting on Pt deposited by E-beam [103], and FIB [104]. The size of the grains are also in agreement with some reports that observed nanocrystaline structures [105] with a size ranging 8 to less than 3 nm [106]. This grain size is much smaller than the typical grain size of 25 nm in other deposited Pt thin films [107]. The figure also indicates 0.23 nm (111) interplanar spacing, which is consistent with the previous reports for platinum [108]. From this figure it is not immediately clear if Ga and C are present. It should be noted that there are areas in Figure 5—3 that are amorphous, which are found to be carbon in the subsequent TEM study.

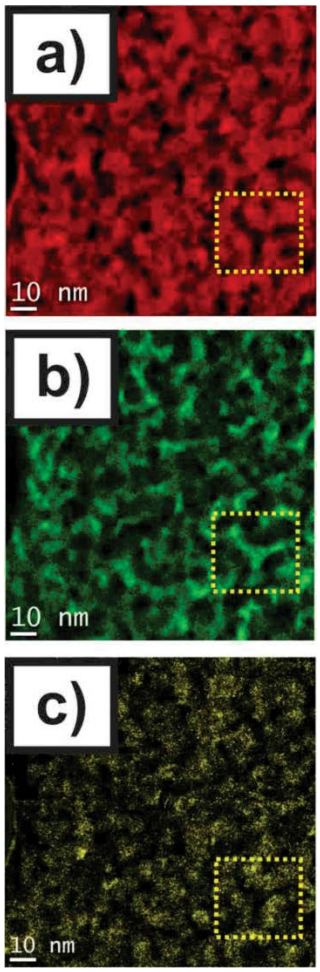

Figure 5—4: Elemental mapping of the sample indicating a) Pt in red, b) C in green, and c) Ga in yellow.

In Figure 5—4 an EDS map of a sample is shown for the FIB deposited Pt. According to this TEM study, the sample shows signatures of Pt, C, Ga, and O which is in agreement with previous reports [71]. Each element was present in the following amounts: 64.1±3.1 at.% Pt, 22.6±7.7 at.% C, 7.38±4.2 at.% Ga, and 4.87±4.1 at.% O. The content of Pt is observed to be higher and the Ga concentration to be lower than the earlier report [71], possibly due to a different precursor pressure. However the atomic fractions , observed in this work, are closer to the more recent work carried out

in a similar dual FIB/SEM platform [106] reporting 45-55 at.% C, 40-50 at.% Pt, 5-7 at.% Ga, and 5 at.% O. We noticed that the actual measured current in our work is 290 pA which is higher than expected nominal current of 30pA in common with the Ref. [106]. Accordingly the difference between this and the aforementioned reports can be attributed to a different FIB's current.

Figures 5—4a, b, and c show the maps of the elements Pt, C, and Ga respectively. The O map is not shown because the amount is too low and the map indicates a fairly homogenous distribution of the element. Comparing Figures 5—4a and b, it can be seen that layers of carbon are present between the platinum phases. A box made of a dashed yellow line is used as a reference to facilitate this comparison. In the yellow box of Figure 5—4a one can see the black 'T-shaped' background showing the absence of Pt, which corresponds to the green 'T-shaped' area showing carbon in Figure 5—4b. Furthermore, by comparing aberration corrected images with EDS maps it was found that the areas with Pt correspond to the crystalline areas and the amorphous areas correspond to the C. Having a heterogeneous mixture such as this will undoubtedly contribute to the lower thermal conductivity of the FIB deposited film. This phase could also contribute to the lower electrical conductivity of the FIB deposited platinum previously reported to be more than three orders of magnitude lower than that of bulk platinum [84].

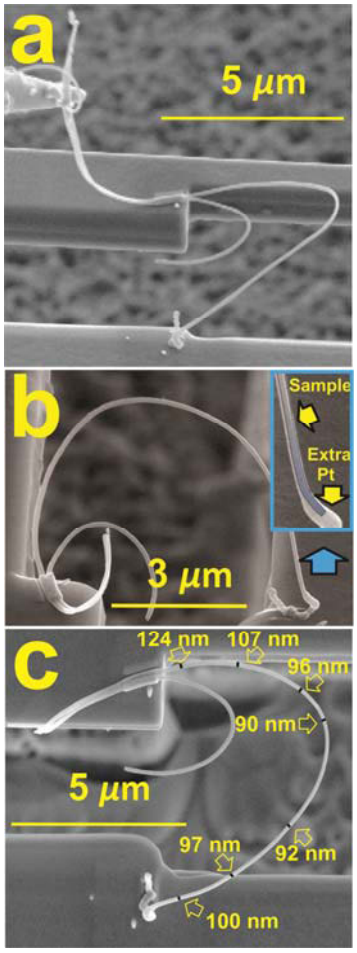

Figure 5—5: Extra deposited Pt after fixing a carbon nanofiber a) the fiber is transferred by a micro manipulator and being welded by Pt deposition, b) the micro manipulator moved away and nanofiber is fully fixed on the measuring stages (the enhanced inset magnifies the fiber and the welded region where additional Pt is deposited on the sample), c) the variation of the diameter of nanofiber shows the additional unwanted Pt deposited on the nanofiber.

The vast reduction in the electrical conductivity, as noted in previous studies [71, 92] , and thermal conductivity from this study is understandable considering the volume of amorphous carbon located

between the nano-crystalline Pt. Combining the observations of the relatively small grain size of platinum and the amorphous phase of carbon between the boundaries of the grains, the thermal conductivity is expected to be lower than the typical thermal conductivity of 30 W/m-K in regular Pt thin films [77] due to increased scattering in the material. The small amount of Ga and O impurities in Pt will undoubtedly contribute to this reduction as well.

The authors note that one may be tempted to estimate the thermal conductivity of the FIB deposited Pt film based on the Weidemann-Franz Law [109]. However the Lorentz number for bulk or nanofilm platinum typically varies from 2.5 to 6 $\times$ 10^{-8} ($W\Omega/K^2$) [110], and the lower reported electrical resistance of the FIB deposited platinum is 400 $\mu\Omega$-cm [84]. This data results in a thermal conductivity estimate below 0.1 W/mK, which experimentally does not appear to be accurate. The basic assumption of the Weidemann-Franz Law is the negligible contribution of the material's lattice [111], which does not appear to be accurate in this case. Therefore, a direct measurement, such as the one made in this study, is preferable to an estimation solely based on theoretical contribution of electrons to the heat transfer.

Knowing the thermal conductivity of platinum deposited by this process can be used to estimate the amount of thermal resistance (or conductivity), which is due to the FIB, deposited Pt. This is especially important for measurements where the FIB deposited platinum is used for attaching micro/nano samples [67, 95]. The information can also be used in heat transfer considerations, when FIB deposited Pt is used for repairing IC chips or for the engineering of new meta-materials such as

phononic crystals. Further study of the grain size and atomic structure of the FIB deposited Pt could be used to optimize the key parameters involved in the process such as substrate material, ion beam current, and accelerating voltage in view of the aforementioned applications.

5-4 Case Study on Carbon Nanofibers

In order to illustrate the impact of the thermal characterization of the Pt deposited in the micro-welding process, carbon nanofibers are thermally characterized. A carbon nanofiber with diameter of 80 nm and length of 12.5 μm (See Figure 5—5) is transferred with a mico-manipulator and affixed by FIB deposited Pt. Details for the processing of the nanofiber used can be found elsewhere [112, 113], and transferring and affixing of nanofibers is a common process for thermal characterization [30, 67, 68, 95, 97, 98].

Figure 5—5a shows the sample being welded to the measurement stages with FIB deposited Pt while it is held by the micro-manipulator. The stages are connected to two measuring islands with Pt sensors for measurement of the thermal resistance. The measuring islands here are the same ones addressed in the Measurement Technique Section, and used for characterization of the FIB deposited Pt. A minimal amount of material is FIB-deposited to minimize contamination of the sample as shown in Figure 5—5b and the inset of Figure 5—5b. Only small areas around the ends of the sample, in touch the stages, are exposed for deposition of Pt. However, a small amount of Pt is inevitably deposited on the other areas of the sample. This creates cone shape areas towards the ends

of the fiber where it is affixed to the stages as is evident in Figures 5—5b, inset of 5b, and c. This phenomenon of over-spraying Pt is due to a complex nature of Pt deposition by secondary particles in an area larger than the primary zone of the focused ions [114]. Therefore a secondary larger zone for the Pt deposited by secondary particles which are not expected to damage the effective length of the sample. The similar phenomenon of the over-sprayed Pt is observable in other work [96, 115], but its erroneous effect has not been quantified.

In Figure 5—5c the diameter of the nanofiber after micro-welding is shown at different positions. Here the cone-shape of the sample due to the added FIB deposited Pt is more pronounced. The diameter of the nanofiber was 80 nm initially, but after deposition of FIB deposited Pt the diameter of the sample is increased up to 50% towards the ends of the fiber. This added FIB deposited Pt can potentially have a considerable erroneous effect on the measurement depending on the diameter and thermal resistance of the sample.

To quantify the erroneous effects of the FIB deposited Pt on the thermal characterization of 1-D nanostructures, a nanofiber that has been previously affixed using FIB deposited Pt, is thermally characterized as shown in Figure 5—5. If one neglects any contribution from the added platinum the thermal conductivity of the nanofiber is calculated to be 45 W/mK. SEM images of the nanofiber are in Figures 5—5a-c. This is equivalent to assuming the interfacial resistance between Pt and the sample is extremely high. However it is more plausible to assume that the FIB deposited Pt

contributes to the thermal conductance as well. To study this effect we first assume that the sample is divided into *n* pieces in series. Therefore, the overall thermal conductivity becomes:

$$R = \sum_{m=1..n} \Delta R_m \tag{5-1}$$

Where *R* is the total thermal conductivity and ΔR_m is the thermal resistance of the *m*th piece, and *n* is the total number of divisions. In the limit of the highest thermal contribution of Pt, the two parts of Pt and nanofiber can be assumed two parallel resistors in each piece therefore:

$$\Delta R_m = \left(\left(\frac{L/n}{A_{nf}^m \kappa_{nf}} \right)^{-1} + \left(\frac{L/n}{A_{pt}^m \kappa_{pt}} \right)^{-1} \right)^{-1} \tag{5-2}$$

where L/n is the length of each small piece. A_{nf}^m and A_{pt}^m are the cross-sectional areas of the Pt and nanofiber, and the κ_{nf} and κ_{pt} are the corresponding thermal conductivities. Noticing the fact that A_{nf}^m and κ_{nf} are constant, simplifying Eq. (5-2) leads to:

$$R = \left(A_{nf}\kappa_{nf}\right)^{-1} \sum_{m=1..n} L/n \left(1 + A_{pt}^m \kappa_{pt} / A_{nf}^m \kappa_{nf}\right)^{-1} \tag{5-3}$$

In the limit of a large *n*, Eq. (5-3) converges into an integral:

$$R = \left(A_{nf}\kappa_{nf}\right)^{-1} \int_0^L \frac{1}{1+r} dl \tag{5-4.1}$$

$$r = \frac{A_{Pt}\kappa_{Pt}}{A_{nf}\kappa_{nf}} \tag{5-4.2}$$

The ratio *r* defines the ratio of the cross sectional thermal conductances of the Pt and the nanofiber sample. When this ratio vanishes there is no contribution from the FIB deposited platinum and:

$$R_{nf} = \frac{L}{A_{nf} k_{nf}} \tag{5-5}$$

which is the thermal resistance of the nanofiber only. The error is defined as:

$$\frac{\Delta R}{R} = \frac{R_{nf} - R}{R} \tag{5-6}$$

For relatively small values of *r* (e.g. < 0.1):

$$\frac{\Delta R}{R} = \left(\frac{V_{pt} \kappa_{pt}}{V_{nf} \kappa_{nf} - V_{pt} \kappa_{pt}} \right) \tag{5-7}$$

where *V* is the volume. Using Eqns. (5-5 to 5-7), the dimensions (depicted in Figure 5—5c), and the thermal conductivity of FIB deposited Pt (characterized in this work) the thermal conductivity of the sample changes from 45 W/mK to 42 W/mK. A second (more amorphous) nanofiber sample is also studied. The second nanofiber featured length and average diameter of 8.8 μm and 96 nm respectively. Using the same consideration about the deposited platinum after the correction the thermal conductivity varies from 1.6 W/mK to 1.35 W/mK. The new values are the lower limit considering the Pt contribution. This approach shows a range of 7.1% and 19% in systematic errors due to the added Pt for micro-welding of the carbon nanofibers. Evidently the higher thermal resistance of the sample exacerbates the erroneous effect. It must be noted that this correction only corresponds to the systematic error due to the thermal contribution of the added FIB deposited Pt,

which has not been characterized and considered previously. In addition to this systematic error due to the Pt added to the sample, other random or systematic sources of errors in contacts [97] and the technique are still possible which have been studied [72] and are not the subject of this work. A similar approach can be followed in previous or future work on the thermal characterization of different nano samples to attain more accurate results by considering the systematic erroneous effect of the FIB deposited Pt used to affix samples.

5-5 Conclusion

In this work the thermal conductivity and the crystalline structure of platinum deposited by FIB was studied. An ion voltage of 30 kV and a current of 30 pA was used for deposition. The study showed that the thermal conductivity of the platinum is 7.2 ± 40% W/mK, which is notably lower than the thermal conductivity of a pure thin film of platinum estimated at 30 W/mK and the bulk value of 71.6 W/mK. TEM imaging of the sample identified impurities of C, Ga and O in agreement with previous work. Despite previous efforts indicating an amorphous structure for FIB deposited Pt, the sample was observed to contain polycrystalline Pt with small grain sizes of 4 nm. Amorphous C was observed to lie between the nano-crystalline Pt, while a smaller amount of Ga was present in the Pt grains. O was homogeneously distributed throughout the structure. The low thermal conductivity of the FIB deposited Pt can be attributed to combination of these effects which leads to a higher level of scattering in the material. This information can be utilized in thermal characterization of nano-

samples, since Pt is a very common material for affixing such samples to MEMS platforms. To demonstrate this application, two micro fibers were characterized and the thermal contribution of the Pt was considered as systematic error. It was shown that neglecting the effects of the FIB deposited Pt could lead to a considerable error in reported measurements of the thermal conductivity of nanostructures.

6 Coherent Boundary Scattering of Phonons at Room Temperature

Almost all physical processes produce heat as a byproduct, making heat one of the most abundant forms of energy. Thermoelectric systems are among the few technologies that can convert heat directly into electricity, using the Peltier effect [116]. The performance of thermoelectric devices is gauged by the dimensionless thermoelectric figure of merit $ZT=(S^2\sigma\kappa^{-1})T$; where S, σ, κ, and T are the Seebeck coefficient, electrical conductivity, thermal conductivity, and temperature respectively. While Si-based semiconductors typically have very favorable power factors ($S^2\sigma$) [117-119] making them attractive for chip cooling and scavenging applications, their large phonon-dominated κ has prevented their use in TE systems. One approach is to use porosity to scatter phonons and hence reduce their contribution to κ [31, 120]. However, there is a limit beyond which an increased porosity with corresponding small pore separation would lead to increased electron scattering and inadvertently reduce σ.

All the materials in this chapter are reproduced with permission from another report [33]. This chapter is a modified version of that article. © 2015 Mcmillan Publishers Limited. Contribution of the author SA in that article was fabrication the measurement platform, conducting the experimental measurements, processing the measured experimental data, contributing to the discussion and preparing a majority of the supplementary materials. For additional information readers are encouraged to refer to other works [33, 34]. SA also acknowledges the contribution of the other equally contributing author DG as well as all the co-authors.

6-1 Introduction

Recently, it has been proposed that coherent boundary scattering in phononic crystals (PnCs) with relatively large feature sizes (≥100nm) may hold the key to solving this problem by scattering phonons with minimal influence on electrons [13, 17, 32]. As phonons traverse such a lattice, they can undergo two types of scattering processes: simple particle-like incoherent scattering as a result of encountering a boundary; and wave-like coherent Bragg [4] scattering due to the periodic geometry of the artificial lattice of air holes. Here, coherence implies that the phonon phase is preserved and that scattering from material boundaries exhibits at least some measure of specularity. Practically, this can have profound implications because while incoherent boundary scattering depends only on the shape, size, and separation of the holes, coherent boundary scattering additionally depends on the symmetry and geometry with which these holes are distributed. Thus, the existence of coherent scattering would enable further reduction of the thermal conductivity of the underlying material without the need for additional boundaries (e.g. more air holes) by simply optimizing the PnC geometry. While coherent phonon boundary scattering has been observed at low temperatures (30K-150K) in 1D superlattices [121], it has yet to be observed and verified in 2D or 3D PnCs, let alone at room temperature.

Thus, the possibility of coherent phonon boundary scattering in Si-Air PnCs at room temperature has generated widespread debate in the literature, given the relatively small wavelength of the phonon population dominating the thermal transport [17, 31, 122-125]. Experimentally, however,

the thermal conductivity (κ) of PnC samples has consistently been measured to be significantly lower than that of an unpatterned film [13, 31, 32, 124, 125], even after taking into account the combination of material removal and simple incoherent boundary scattering [13, 32, 124]. This suggests that another κ reduction mechanism, possibly coherent boundary scattering, must be taking place. The controversy was heightened by the discovery that ~50% of the thermal phonons in Si have mean free paths (MFPs) from 100nm up to 1μm [126], which was recently verified experimentally [127]. Since it is logical to assume that a phonon remains coherent over its MFP, we suggest here that the MFP, rather than wavelength, should be used to determine whether or not a large enough fraction of the phonon population could travel sufficient distances while maintaining phase to experience the PnC lattice periodicity and thus undergo coherent boundary scattering.

Several methods exist for calculating κ that assume partially coherent and partially incoherent phonon boundary scattering [17, 31, 122, 124, 125]. In particular, Hao, *et al.*[122], used Monte Carlo simulations combined with frequency-dependent phonon MFPs [126] to study phonon transport in a 2D square-lattice PnC, and concluded that phonon size effects caused by the periodic arrangement of the holes can be remarkable even when the hole size and spacing are much greater than the average phonon MFP. Tang, *et al.* [31] suggested the possibility of a "necking effect" for phonons with MFPs longer than the smallest dimension of the lattice. Dechaumphai, *et al.* [128] used an approach where phonons with MFPs longer than the minimum feature size (distance between adjacent holes) were treated coherently as waves and were modeled using a finite-difference time-domain technique, while phonons with MFPs smaller than the minimum feature size

were treated as particles and their transport modeled by the Boltzmann transport equation, taking into account only incoherent boundary scattering. Their study found some agreement with recent experimental work on nano-scale PnCs [32], highlighting the importance of zone folding, however the model failed to reproduce the cross-plane data [13] possibly because of the lack of lattice periodicity in that direction. Conversely, Jain, *et al.* [123] argued that a major deficiency in the previous models is their 2D nature, and proposed a full 3D model. Room temperature Monte Carlo simulations accounting for purely incoherent boundary scattering via the Boltzmann transport equation were used. The apparent agreement between theory and experiment [123] led the authors to conclude the absence of any coherent phonon boundary scattering. Although the incoherent nature of the model should have made it insensitive to propagation direction and scatterer geometry, the model was surprisingly deficient in reproducing the κ measured for unperforated slabs and the cross-plane PnC [13] direction, raising doubts that incoherent boundary scattering is solely responsible for the experimentally observed κ reduction in such PnCs. Thus, the matter of coherent versus incoherent phonon boundary scattering at room temperature remains an open question, and begs for a control experiment isolating the two scattering mechanisms to enables their independent quantification.

In this communication, we focus on PnCs formed by the induction of air holes in a Si matrix with minimum feature sizes ≥100nm. To delaminate the incoherent and coherent phonon scattering mechanisms, we present an experiment that fixes the incoherent boundary scattering component and systematically varies the coherent component. We also introduce a hybrid thermal conductivity

model that accounts for partially coherent and partially incoherent phonon boundary scattering, to enable the accurate prediction of thermal conductivity reduction in such structures. We observe excellent agreement between this model and the experimentally measured data, suggesting that significant room temperature coherent phonon boundary scattering does indeed occur.

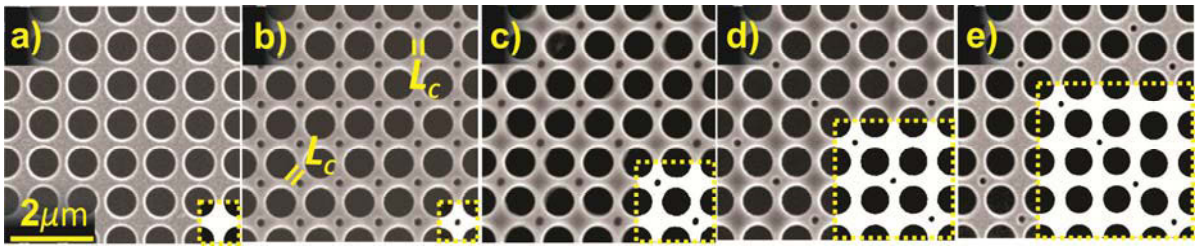

Figure 6—1: SEM image of the fabricated PnC structures. All samples were fabricated to have a periodicity $a = 1100\text{nm}$, thickness $h = 366\text{nm}$ and a chosen critical dimension $L_c = 250$ nm . Highlighted in white is the unit cell of each supercell lattice: (a) SC, (b) 1x1, (c) 2x2, (d) 3x3 and (e) 4x4.

6-2 Theoretical Frame Work

The phonon contribution to thermal conductivity in the structures of interest in this study can be modeled based on the Callaway-Holland formulation [18], given by:

$$\kappa = f(\phi)\cdot\frac{1}{6\pi^2}\sum_j\int_q \frac{\hbar^2\omega_j^2(q)}{k_B T^2}\frac{\exp\left[\frac{\hbar\omega_j(q)}{k_B T}\right]}{\left(\exp\left[\frac{\hbar\omega_j(q)}{k_B T}\right]-1\right)^2}v_j^2(q)\tau_j(q)q^2 dq \tag{6-1}$$

where $\hbar$ is the reduced Planck constant, f is a function accounting for the sample porosity (ϕ), q is the wave vector, $\omega(q)$ is the phonon dispersion, k_B is the Boltzmann constant, T is the phonon temperature, $v(q)=\partial\omega(q)/\partial q$ is the phonon group velocity, $\tau(q)$ is the scattering lifetime of the phonons, and the summation is over all phonon modes. In Si, the phonon scattering lifetime is dominated by Umklapp, impurity, and incoherent boundary scattering, which are given by [129]

$\tau_{Umklapp,j}^{-1}=BT\omega_j^2(q)\exp[C/T]$, $\tau_{impurityj}^{-1}=D\omega_j^4(q)$, and $\tau_{boundary,j}^{-1}=Ev_j(q)/L$, respectively, where L is the effective sample length and is a measure of the average distance between boundaries [13, 18, 130, 131]. The constants *B*, *C*, *D*, and *E* measure the fractional influence of these different types of scattering mechanisms in a given sample, and are determined by fitting Eq. (6-1) to measured bulk Si data. Other thermal conductivity models highlighting different treatments of anharmonic Umklapp phonon scattering were also considered. In highly porous samples, L can be replaced by the sample minimum feature size or critical dimension L_c [31, 120] (Fig. 6—1), this corresponds to the maximum possible incoherent boundary scattering, or the incoherent scattering limit. The three scattering times are related to the total phonon scattering life time in Eq.(6-1) via Matthiessen's rule:

$$\frac{1}{\tau_j(q)}=\frac{1}{\tau(q)_{umklapp,j}}+\frac{1}{\tau(q)_{impurity,j}}+\frac{1}{\tau(q)_{boundary,j}} \tag{6-2}$$

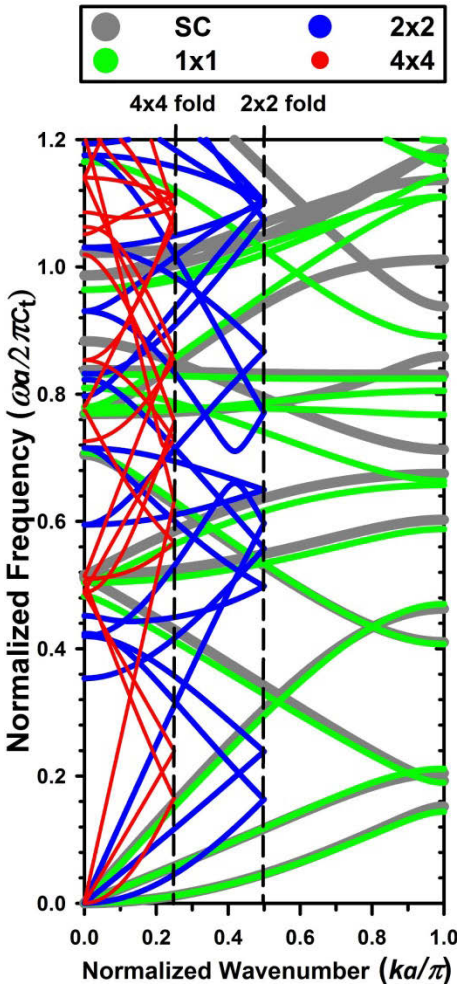

Figure 6—2: Coherent zone folding due PnC patterning in Fig. 6—1: PWE calculated dispersions for the various *nxn* supercell lattices: SC (gray), 1x1 (green), 2x2 (blue) and 4x4 (red). The 3x3 supercell lattice was intentionally left out for clarity. The black dashed lines represent the respective Brillouin zone edges.

In this formulation, assuming a sufficiently large sample thickness [132-135] and feature sizes [123], if coherent boundary scattering were absent, the Si phonon dispersion would remain basically unaltered before and after the PnC patterning and fixing L_c would lead to a constant incoherent boundary scattering limit. We thus set out to realize an experiment where the geometry of the PnC lattice is varied while L_c is kept constant. Previous electrical conductivity measurements on these and similar samples indicate that the impurity concentration remains practically unchanged before and after the PnC patterning [124]. The basis of our experiment is a simple PnC composed of a 2D simple cubic (SC) array of air holes in a Si slab with a designed periodicity $a = 1100\text{nm}$, thickness $t = 366\text{nm}$ and a chosen critical dimension $L_c = 250$ nm. Smaller interpenetrating holes, with dimensions chosen to keep L_c constant, are then introduced at the center of the unit cell to create a series of lattices whose unit cell is now a composite supercell, as shown in Fig. 6—1. These interpenetrating PnCs range from what is termed a 1x1 supercell, where the smaller hole is introduced at the center of every SC unit cell, to a 4x4 supercell that has four smaller holes added per every 16 SC unit cells. With this arrangement, the 1x1 supercell lattice has a unit cell size equal to that of the SC lattice but with the added smaller hole at the center, while the various *n*x*n* supercell lattices have unit cell sizes that are n^2-times (n = 1, 2, 3, 4) that of the SC lattice. Thus, if phonon coherence persists through the scattering process, the Brillouin zone length of an *n*x*n* supercell is *n*-times smaller when compared to that of the original SC lattice, yielding *n*-times folded dispersion. This is real folding, brought about by the actual periodicity of the underlying lattice (see Fig. 6—2), as opposed to artificial folding created by choosing an arbitrarily large unit cell when calculating its

dispersion. Figure 6—2 shows the computed phonon dispersion using the plane wave expansion (PWE) technique[17]. Implicit in this calculation is the assumption that phase information is retained throughout the entire spectrum. Examining Fig. 6—2, it is clear that there is considerable deviation among the bands of the various supercell lattices, ranging from increased band curvature to band movement and even the introduction of new bands. To this extent, if these dispersions were to be theoretically unfolded, the various supercell bands would not overlay one another. This means that if coherent scattering is indeed taking place, there would be substantial deviation in group velocity and the density of phonon states across the various supercell lattices. This would manifest itself as a measurable systematic difference in κ as n increases that exceeded the combined influence of incoherent boundary scattering and the added porosity resulting from the introduction of the smaller holes.

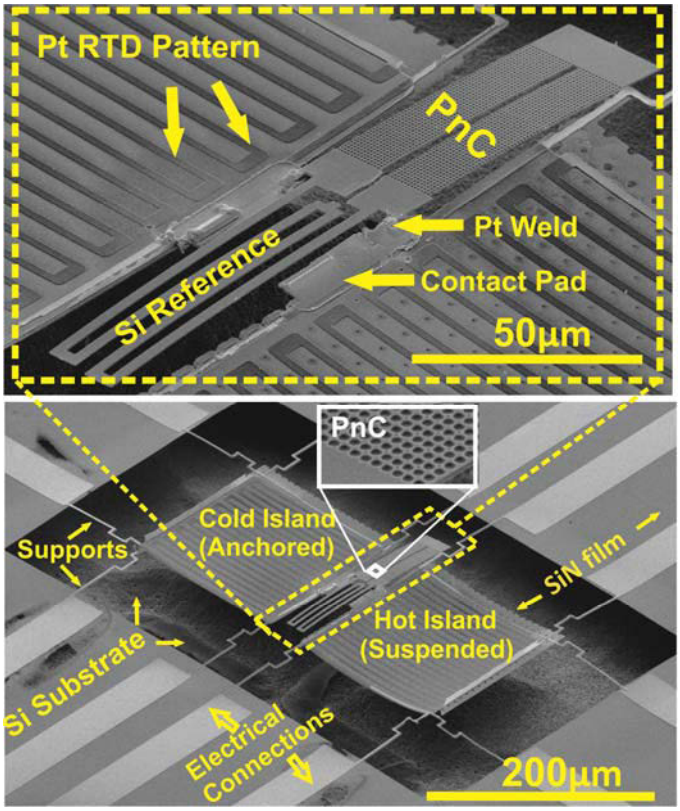

Figure 6—3: **SEM images of a measurement platform used in this work for the κ experiments; RTD: resistive temperature detector.**

6-3 Sample Preparation and Measurement

Focused ion beam (FIB) milling with Ga^+ ions (Supplementary Method) was used to fabricate the PnC samples. Extreme caution was taken to avoid the contamination of the Si samples with any spurious Ga^+ ions by using a sacrificial mask layer, which in addition to later etching of the samples resulted in the elimination of any added surface roughness due to the fabrication process (see the

Methods Section). The κ of various supercell samples was measured using a suspended island technique [30] (Fig. 6—3), where a sample is mounted between two thermally isolated islands. By increasing the temperature of one island relative to the other and measuring the applied power and resulting temperature difference, the κ of the samples can be deduced [30, 67, 94]. Fabricated samples were attached to the suspended islands using a pick-and-place approach. Successive cuts using the FIB were employed to systematically calibrate out any unknown thermal resistances (*e.g.* contact resistance, leg resistance, etc.) and uniquely determine the thermal resistivity of the PnC supercell samples relative to that of an unpatterned Si slab of the same thickness. A detailed description of the process along with a quantification of the associated errors is given in Supplementary Method.

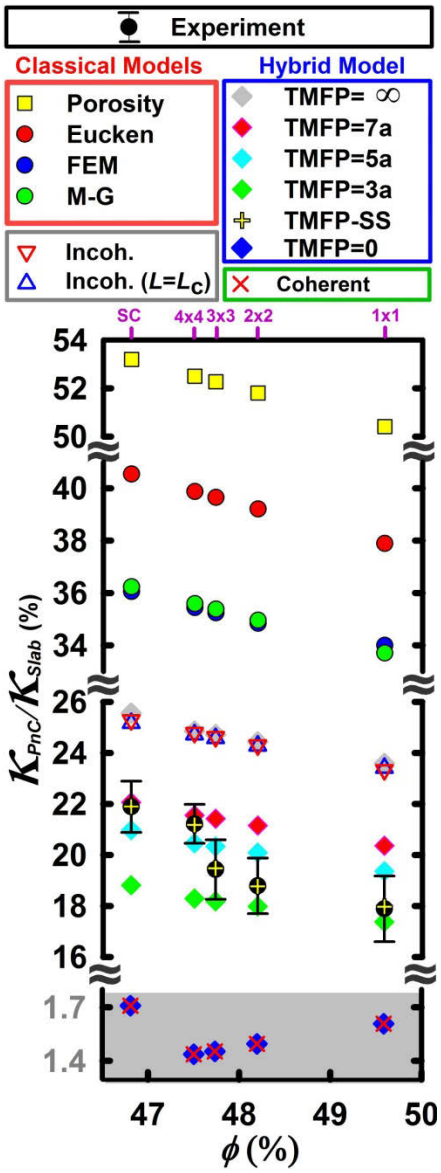

Figure 6—4: The measured κ of the simple cubic (SC) and the 1x1, 2x2, 3x3, and 4x4 supercell PnC samples, along with the predicted values using various models described in detail in the text.

Figure 6—4 shows a plot of the measured (black circles with error bars) κ of the various PnC lattices (κ_{PnC}) of Fig. 6—1 normalized to that of an unpatterned Si slab (κ_{Slab}) of the same thickness versus the sample porosity, ϕ. A discontinuity in the slope can be distinctively identified, suggesting a competition between two phenomena with opposing trends accompanied by a discrete

transition. The results are compared with various theoretical model predictions ranging from simplistic porosity models to complex hybrid continuum-lattice dynamics models in order to explain the observed behavior.

6-4 Measurements versus Traditional Thermal Conductivity Models

First, a series of classical mean-field models are evaluated. The yellow-squares represent the expected normalized κ due to simple material removal, obtained by using $f(\phi) = 1 - \phi$ in Eq. (6-1). As expected, this severely underestimates the observed reduction in κ, as it neglects the pore (air hole) shape and surface area, accounting only for its volume. Analytical porosity models that take into account the added boundaries due to the pore shape and surface area are also evaluated. The red-circles represent the results of the Eucken model [136] $f(\phi) = (1 - \phi)/(1 + \frac{2}{3}\phi)$, while green-circles represent those of the Maxwell-Garnett (M-G) model [137] $f(\phi) = (1 - \phi)/(1 + \phi)$. Despite the complexity in the derivation of these models, they still largely underestimate the experimentally measured κ_{PnC} reduction. This suggests that the reduction is not simply due to the porosity of the samples. Also shown on the plot are the results obtained from finite element method (FEM) simulations of the PnC samples using ANSYS® [138] (blue-circles). It is worth noting the excellent agreement between the M-G model and the FEM simulation results, lending more credibility to the M-G formulation over Eucken's when accounting for porosity effects on the length scales considered here.

Next, we include the effects of incoherent scattering by retaining the M-G factor in (1), using bulk Si dispersion, and accounting for the relative positions of the PnC boundaries (holes) through the choice of the value of L. One possibility is to simply use L_c to ascertain the incoherent scattering limit (blue-triangles). Since this is the smallest physically-meaningful value of L, it corresponds to the maximum possible reduction from models assuming solely incoherent scattering and actually predicts a larger reduction in conductivity than that predicted by Ref. [13], which argues in favor of purely incoherent scattering. There, the effective sample characteristic length L_{eq} is seen to be consistently larger than L_c by more than 100nm for each corresponding sample. However, the choice of $L = L_c$ treats all of the samples identically and is insensitive to the increase in the number of boundaries with the supercell order *n*. Thus, we also consider an alternate model for deducing an order-dependent sample size L. Noting that phonon scattering events by the in-plane air hole boundaries and the cross-plane sample surface-boundaries are stochastic rather than mutually exclusive, a Matthiessen's rule-type approach can be used to separate their influence as $1/\tau_{boundary,j} = 1/\tau_{cross-plane,j} + 1/\tau_{in-plane,j}$, with $\tau_{cross-plane,j} = t/v_j(q)$. The in-plane component can be evaluated using an order-dependent effective sample size L_n, obtained by geometrically averaging over the relative in-plane boundary separations in a given sample[18] with $\tau_{in-plane,j} = L_n/v_j(q)$. Alternately, each PnC sample can be viewed as a combination of *n*(*n-1*) SC unit cells and *n* 1x1 unit cells. A boundary scattering lifetime associated with each type can then be calculated by averaging over the relative boundary separations in each unit cell and then combining using Matthiessen's rule: $1/\tau_{in-plane,j} = (n-1)/(n\tau_{SC}) + 1/(n\tau_{1\times1})$. The results of both approaches were found to be almost

identical and are depicted by the red triangles in Fig. 6—4. It is worth noting the agreement between the limiting case of $L = L_c$ and independently treating the in-plane and cross-plane incoherent scattering. Inspecting Fig. 6—4, however, it is evident that even at maximum incoherent scattering the results still considerably underestimate the observed κ reduction in rate and magnitude and do not reproduce the slope discontinuity, suggesting that an additional scattering mechanism with an opposing trend (increasing with *n* and decreasing with ϕ) is possibly present.

Consequently, the expected κ reduction was calculated assuming purely coherent (wave-like) phonon boundary scattering from the PnC holes, plotted as red-x's in Fig. 6—4. Here, the PnC dispersion (a zoom-in of which is shown in Fig. 6—2) is used for, $\omega(q)$ which implicitly accounts for the existence of the air holes; hence we set $f(\phi) = 1$ in Eq. (6-1). Incoherent scattering from the surface boundaries of the sample was still accounted for by setting $L = t$. A total of over 46,000 modes were used in the calculation of the PnC dispersion [17]. It is worth noting here that this method is quite accurate for the acoustic phonon branches but to a lesser degree for the optical branches. However, the latter are estimated to contribute at most about 3.5% of the overall κ in bulk Si prior to any reduction [126, 127] due to patterning. While our treatment clearly overestimates the reduction in κ due to the PnC patterning and exaggerates the dispersion effects of the PnCs on the acoustic branches, it is worth noting the reversal of the trend in $\kappa_{PnC}/\kappa_{Slab}$ versus ϕ(and *n*), consistent with our expectations from Fig. 6—2.

6-5 Hybrid Thermal Conductivity Model

The results of these approaches indicate that a model that assumes partially coherent and partially incoherent boundary scattering is needed. The dilemma is in how to determine what portion of the phonon population undergoes coherent versus incoherent boundary scattering off of the PnC lattice holes. Since it is reasonable to expect a phonon to remain coherent over its MFP, one suggestion is to use the MFP to discern the scattering mechanism. We thus propose a model that incorporates frequency dependent phonon MFPs in Si [126, 127] and introduce the concept of a Threshold-MFP (TMFP) that is essentially a measure of the phonon minimum coherence length. Phonons possessing a MFP above the designated TMFP value are able to sample the periodicity of the lattice and undergo coherent boundary scattering by the PnC, thus exhibit a modified Si dispersion due to the PnC lattice, while phonons possessing a MFP below it do not "see" the periodicity and thus undergo only incoherent boundary scattering and follow the unmodified Si dispersion. Therefore, the incoherent and coherent boundary scattering contributions to κ_{PnC} are individually weighed by the fractional portion of the phonon population based on their MFPs with respect to the TMFP. Given the absence of a direct way to experimentally measure the coherence length of phonons, we use the thermal conductivity measurement itself as a gauge for this determination. The TMFP is thus incorporated as a free parameter used to tune the model against the experimental measurements. While we acknowledge that a transition between coherent and incoherent boundary scattering should be gradual, there exists no practical theoretical foundation that allows us to gradually relax the preservation of the phonon phase as the mean free path decreases (frequency increases) when we

calculate the PWE-based PnC dispersion. The diamonds in Fig. 6—4 represent the results of five choices of the TMFP value. Note that our hybrid model correctly reproduces the limiting cases matching the purely-coherent scattering calculation at TMFP = 0 (blue-diamonds) and the incoherent scattering case at TMFP = ∞ (gray-diamonds), including the reversal of the trends between both cases, thus lending credence to the model (Supplementary Note 3[33]). It is particularly interesting that the hybrid model agrees well with the experimental data when the TMFP is large enough to cover 3-5 lattice periods, as this is similar to the literature-accepted bounds [3, 4, 8, 16, 139-141] for the fewest and largest number of periods needed to observe PnC behavior.

It is instructive to point out that the bounding TMFP values listed in Fig. 6—4 represent a population average over all supercell samples, which is a gross approximation as the TMFP is likely to be geometry (supercell) dependent. To this end, the yellow pluses in Fig. 6—4 represent the sample-specific TMFPs, designated TMFP-SS. Inspection of the TMFP-SS values show that the 1x1 supercell and the SC lattices are characterized by the smallest and largest TMFP-SS values respectively, and hence the largest and smallest respective fractions of coherently boundary scattered phonons. This is to be expected, since the 1x1 supercell lattice has the largest areal density of scatterers, and hence on average requires that phonons traverse much shorter distances before encountering a boundary scattering event as compared to the SC case. Thus on average, for coherent boundary scattering to occur, it would be necessary to conserve phase information over much shorter distances (shorter times) in the 1x1 case as compared with the SC case. Thus this condition is likely to be met by a larger fraction of phonons in the 1x1, and a comparatively much smaller

portion of the phonon population in the SC case. Indeed, one can easily show that the number of equidistant scatters per unit cell is $4(n+1)/n$, in which case SC represents the limit as $n \to \infty$.

Furthermore, the location of the slope discontinuity between the 4x4 and 3x3 experimental points can also be explained based on the calculated TMFP-SS values (Supplementary Notes 3 and 4 [33]). According to Ref. 16, which uses a density functional theory approach to study heat transport in Si, it is clear that there exist certain heavily-populated phonon modes that dominate over other less-populated ones (Fig. 6 in Ref. [126]). More specifically, that work identifies several distinct MFP bands that result collectively in a nonlinear increase in the accumulation function; a range beyond 10μm, and two bands starting around 7.9μm and 4.3μm that are of particular interest. Examining our reported TMFP-SS values, it is seen that the TMFP-SS for the 1x1, 2x2, and 3x3 supercells are about or less than 4.3μm, while both the SC and 4x4 supercells are found to be much larger than that value (approaching 7μm). Since by definition the TMFP-SS is the cutoff value per sample for the MFP beyond which a significant portion of the population undergoes coherent scattering, its value can be used to mark (on average) which of the dominant states the supercell phonon population predominantly belongs to or is influenced by.

Finally, we wish to point out that while it is tempting to try to attribute the decrease in thermal conductivity of the supercell samples to the added surface boundaries of the interpenetrating holes, the added surface area is actually a false indicator of the effect of the added boundaries and would yield contradictory conclusions.

6-6 Discussion

In this article, we present evidence that coherent scattering of phonons can indeed take place in 2D PnCs with submicron features including the first, to our knowledge, room temperature experimental observation of this phenomenon in such lattices. We also introduced the concept of a threshold mean free path in conjunction with a hybrid theoretical model, where the incoherent and coherent contributions to thermal conductivity are weighted according to the fractional portion of the phonon population mean free paths relative to that threshold. Although the periodicity of the PnC samples is large compared to the average phonon wavelength, our results indicate that a significant portion of the phonon population remains coherent even after undergoing several scattering events. From a different perspective, since there is no direct way to measure the coherence length, our approach has enabled us to use the thermal conductivity as a macroscopic metric for inferring the average phonon coherence length in our PnC samples. It is imperative to realize that the coherence length deduced here is an average over the total population, whereas the actual coherence length of individual phonons is likely both frequency- and geometry-dependent. Our results reinforce the suggestions of coherent phenomena indeed taking place in PnC samples, as postulated by Yu, *et al.* [32] and Dechaumphai, *et al.* [128] It also highlights the importance of accurately calculating the frequency-dependent phonon mean free path.

This work may hold the key to unprecedented TE performance through further suppression of phonon transport in porous samples with no added influence on electron propagation, by simply

arranging the pores in an optimal PnC geometry. While the coherent PnC effects seen here represent a small yet significant fraction of the overall thermal conductivity reduction, their presence at room temperature is extremely encouraging. Given that a more pronounced effect is expected at lower temperatures, the impact to TE cooling could be profound. We point out that this PnC technology is applicable to all semiconductor materials, and could result in a net gain in ZT for any material that is limited by a large κ and that has a thermal conductivity that is dominated by phonon, rather than electron, transport.

6-7 Methods

The realization of the aforementioned control experiment requires the ability to accurately control the fabricated PnC dimensions. To accomplish this, we used focused ion beam (FIB) milling with Ga^+ ions to fabricate the supercells proposed in Fig. 6—1.

FIB Milling of the Phononic Crystal Samples

To avoid obtaining erroneous results, three risks had to be addressed and mitigated, namely: (1) varying cross-sectional dimensions due to using a Gaussian beam of ions leading to uncontrolled variation of the porosity, (2) the uncontrolled implantation of Ga^+ ions in and around the PnC holes and in turn an unquantifiable random impurity scattering, and (3) the added surface roughness and

the thin damage ring of amorphous Si that is associated with milling of the air holes due to the sputtering and re-deposition of Si atoms.

The first and second issues were completely eliminated by the use of a sacrificial mask layer of a material that has a lower sputtering yield than Si (Supplementary Method). The fabrication process of the structures shown in Fig. 6—1 yielded near-vertical sidewalls with less than a 3^{o} measured slant angle. The average dimensional variation in L_c was found to be about 5nm. Furthermore, the use of a sacrificial layer coupled with sample post-processing and etching removed almost all of the contaminating Ga^{+} ions.

Roughness Considerations

After sample post-processing, etching, and removal of the protective mask layer, a change in the surface roughness of the samples is not observed. We inspected the PnC hole-sidewalls using high-resolution transmission electron microscopy (See Chapter 2). The measured RMS roughness value at the boundary of the PnC holes was found to be ~1nm. Details of this study and the effects of roughness are reported elsewhere.

Finally, the damage ring along the perimeter of the PnC hole due to FIB milling is removed during the final step of processing when HF acid is used to release the device [42]. Additionally, it should be noted that the damage ring thickness is on the order of 10nm [40] and is independent of the sizes

of the holes or the beam dwell time. Measurements of the diameters of the holes were made after the removal of this damage ring. To verify the dimensions of the fabricated PnC samples, SEM images covering the entire area of each sample were taken. Image recognition software was then used to determine the average dimensions reported above. The result is in excellent agreement with the target dimensions, with a large hole diameters of 845nm±6nm, a smaller hole diameter of 211nm±6nm, and a critical length of 250nm±5nm.

CONCLUSION

This study demonstrated that due to the novel fabrication techniques at micro/nanoscale PnCs are emerging as a new class of material to be employed in MEMS and NEMS in the upcoming decades. Such materials will have promising applications in further enhancing the performance and shrinking the dimensions of microresonators, and electromechanical filters applicable in RF communications and some sensitive detectors. They also offer very interesting applications in engineering of thermal conductivity of single crystalline materials while minimally affecting their electrical proprieties. Such applications are realized with targeting an optimal periodicity and the consequential size effect, which can reduce the thermal conductivity substantially more than electrical conductivity reduction. This can be achieved by engineering of the group velocities of phonons with certain mean free paths, and bandgaps for some phonons with certain wavelengths in a coherent picture, in addition to the common method of incoherent boundary scattering of phonons. To master this technique some challenges that need to be met are the limited computational power to simulate the bandstructure of extremely large supercells, and fabrication techniques with extreme control on the dimensions and roughness of three-dimensional PnCs. Very promising applications of such optimized PnCs are fabrication of nanostructured single crystalline Si or SiC as a thermoelectric material. A cost effective method for mass production of such thermoelectric PnCs will allow

integration of Si based optoelectronic and electronic devices with thermoelectric devices at micro scale. If this challenge is technologically and cost effectively met, the industry of microprocessors and some low temperature particle detectors will be revolutionized with emerging fully electrical micro heat engines on chip.

References

[1] M. S. Kushwaha*, et al.*, "Acoustic Band-Structure of Periodic Elastic Composites," *Physical Review Letters,* vol. 71, pp. 2022-2025, Sep 27 1993.

[2] M. S. Kushwaha*, et al.*, "Theory of Acoustic Band-Structure of Periodic Elastic Composites," *Physical Review B,* vol. 49, pp. 2313-2322, Jan 15 1994.

[3] I. El-Kady*, et al.*, "Phononic band-gap crystals for radio frequency communications," *Applied Physics Letters,* vol. 92, Jun 9 2008.

[4] R. H. Olsson and I. El-Kady, "Microfabricated phononic crystal devices and applications," *Measurement Science & Technology,* vol. 20, Jan 2009.

[5] R. H. Olsson*, et al.*, "Microfabricated VHF acoustic crystals and waveguides," *Sensors and Actuators a-Physical,* vol. 145, pp. 87-93, Jul-Aug 2008.

[6] R. H. Olsson*, et al.*, "Micromachined bulk wave acoustic bandgap devices," *Transducers '07 & Eurosensors Xxi, Digest of Technical Papers, Vols 1 and 2,* pp. U162-U164, 2007.

[7] C. M. Reinke*, et al.*, "Realization of optimal bandgaps in solid-solid, solid-air, and hybrid solid-air-solid phononic crystal slabs," *Applied Physics Letters,* vol. 98, Feb 7 2011.

[8] Y. M. Soliman*, et al.*, "Phononic crystals operating in the gigahertz range with extremely wide band gaps," *Applied Physics Letters,* vol. 97, Nov 8 2010.

[9] Y. M. Soliman*, et al.*, "Effects of release holes on microscale solid-solid phononic crystals," *Applied Physics Letters,* vol. 97, Aug 23 2010.

[10] D. F. Goettler*, et al.*, "Realization of a 33 GHz phononic crystal fabricated in a freestanding membrane," *Aip Advances,* vol. 1, Dec 2011.

[11] P. E. Hopkins*, et al.*, "Phonon considerations in the reduction of thermal conductivity in phononic crystals," *Applied Physics a-Materials Science & Processing,* vol. 103, pp. 575-579, Jun 2011.

[12] P. E. Hopkins*, et al.*, "Origin of reduction in phonon thermal conductivity of microporous solids," *Applied Physics Letters,* vol. 95, Oct 19 2009.

[13] P. E. Hopkins*, et al.*, "Reduction in the Thermal Conductivity of Single Crystalline Silicon by Phononic Crystal Patterning," *Nano Letters,* vol. 11, pp. 107-112, Jan 2011.

[14] S. Alaie*, et al.*, "Finite Element Analysis of a Phononic Crystal at Gigahertz Frequencies," *Proceedings of the Asme International Mechanical Engineering Congress and Exposition 2010, Vol 13,* pp. 389-393, 2012.

[15] S. Alaie*, et al.*, "Effects of flexural and extensional excitation modes on the transmission spectrum of phononic crystals operating at gigahertz frequencies," *Journal of Applied Physics,* vol. 113, Mar 14 2013.

[16] D. Goettler*, et al.*, "Realizing the frequency quality factor product limit in silicon via compact phononic crystal resonators," *Journal of Applied Physics,* vol. 108, Oct 15 2010.

[17] C. M. Reinke*, et al.*, "Thermal conductivity prediction of nanoscale phononic crystal slabs using a hybrid lattice dynamics-continuum mechanics technique," *Aip Advances,* vol. 1, Dec 2011.

[18] M. G. Holland, "Analysis of lattice thermal conductivity," *Physical Review,* vol. 132, pp. 2461-2471, 15 Dec. 1963.

[19] L. N. Yang*, et al.*, "Reduction of Thermal Conductivity by Nanoscale 3D Phononic Crystal," *Scientific Reports,* vol. 3, p. 1143, Jan 31 2013.

[20] M. G. Baboly, *et al.*, "The effect of stiffness and mass on coupled oscillations in a phononic crystal," *Aip Advances,* vol. 3, Nov 2013.
[21] S. Mohammadi, *et al.*, "High-Q micromechanical resonators in a two-dimensional phononic crystal slab," *Applied Physics Letters,* vol. 94, Feb 2 2009.
[22] F. C. Hsu, *et al.*, "Reducing support loss in micromechanical ring resonators using phononic band-gap structures," *Journal of Physics D-Applied Physics,* vol. 44, Sep 21 2011.
[23] T. R. Lin, *et al.*, "Enhanced acousto-optic interaction in two-dimensional phoxonic crystals with a line defect," *Journal of Applied Physics,* vol. 113, Feb 7 2013.
[24] S. Mohammadi and A. Adibi, "Waveguide-Based Phononic Crystal Micro/Nanomechanical High-Q Resonators," *Journal of Microelectromechanical Systems,* vol. 21, pp. 379-384, Apr 2012.
[25] F. F. Liu, *et al.*, "On the Performance and Sensitivity Limit of Mass Sensing with Optomechanical Oscillation," *2013 Conference on Lasers and Electro-Optics (Cleo),* 2013.
[26] F. F. Liu, *et al.*, "Sub-pg mass sensing and measurement with an optomechanical oscillator," *Optics Express,* vol. 21, pp. 19555-19567, Aug 26 2013.
[27] K. Abbas, *et al.*, "Use of Radiation Pressure to Calibrate Sub Micro-Newton Forces and Damping Ratios," *Proceedings of the Asme International Mechanical Engineering Congress and Exposition (Imece 2010), Vol 10,* pp. 57-61, 2010.
[28] K. Abbas, *et al.*, "Design and characterization of a low temperature gradient and large displacement thermal actuators for in situ mechanical testing of nanoscale materials," *Journal of Micromechanics and Microengineering,* vol. 22, Dec 2012.
[29] A. K. Mousavi, *et al.*, "Nonlinear Approach for Strain Energy Release Rate in Micro Cantilevers," *Proceedings of the Asme International Mechanical Engineering Congress and Exposition (Imece 2010), Vol 10,* pp. 51-56, 2010.
[30] S. Alaie, *et al.*, "Microfabricated suspended island platform for the measurement of in-plane thermal conductivity of thin films and nanostructured materials with consideration of contact resistance," *Review of Scientific Instruments,* vol. 84, Oct 2013.
[31] J. Tang, *et al.*, "Holey Silicon as an Efficient Thermoelectric Material," *Nano Letters,* vol. 10, pp. 4279-4283, 2010.
[32] J. K. Yu, *et al.*, "Reduction of thermal conductivity in phononic nanomesh structures," *Nature Nanotechnology,* vol. 5, pp. 718-721, Oct 2010.
[33] S. Alaie, *et al.*, "Thermal transport in phononic crystals and the observation of coherent phonon scattering at room temperature," *Nature Communications,* vol. 6, Jun 2015.
[34] D. Goettler, "INVESTIGATING THE EXISTENCE OF COHERENT PHONON SCATTERING IN SILICON USING PHONONIC CRYSTALS," Ph.D., Mechancial Engineering, University of New Mexico, Albuquerque, 2013.
[35] K. R. Williams, *et al.*, "Etch rates for micromachining processing - Part II," *Journal of Microelectromechanical Systems,* vol. 12, pp. 761-778, Dec 2003.
[36] H. O'Mara, Hunt, *Hnadbook of Semiconductor Silicon Technology*. Park Ridge: Noyes, 1990.
[37] M. F. Russo, *et al.*, "Trench formation and lateral damage induced by gallium milling of silicon," *Applied Surface Science,* vol. 255, pp. 828-830, Dec 15 2008.
[38] Z. C. Leseman, *et al.*, "Experimental measurements of the strain energy release rate for stiction-failed microcantilevers using a single-cantilever beam peel test," *Journal of Microelectromechanical Systems,* vol. 16, pp. 38-43, Feb 2007.
[39] M. P. de Boer, "Capillary adhesion between elastically hard rough surfaces," *Experimental Mechanics,* vol. 47, pp. 171-183, Feb 2007.

[40] D. S. Ko*, et al.*, "Effective removal of Ga residue from focused ion beam using a plasma cleaner," *Ultramicroscopy,* vol. 107, pp. 368-373, Apr-May 2007.
[41] Y. Drezner*, et al.*, "Characterization of damage induced by FIB etch and tungsten deposition in high aspect ratio vias," *Journal of Vacuum Science & Technology B,* vol. 29, p. 011026, Jan 2011.
[42] C. Anandan and R. H. Williams, "Investigation of Hf Etched Hydrogenated Amorphous-Silicon Surfaces by X-Ray Photoelectron-Spectroscopy," *Semiconductor Science and Technology,* vol. 5, pp. 265-268, Mar 1990.
[43] L. A. Giannuzzi and F. A. Stevie, "A review of focused ion beam milling techniques for TEM specimen preparation," *Micron,* vol. 30, pp. 197-204, Jun 1999.
[44] I. H. Song*, et al.*, "Smoothing dry-etched microstructure sidewalls using focused ion beam milling for optical applications," *Journal of Micromechanics and Microengineering,* vol. 17, pp. 1593-1597, Aug 2007.
[45] M. Sigalas and E. N. Economou, "Band-Structure of Elastic-Waves in 2-Dimensional Systems," *Solid State Communications,* vol. 86, pp. 141-143, Apr 1993.
[46] S. C. S. Lin*, et al.*, "Acoustic beamwidth compressor using gradient-index phononic crystals," *Journal of Physics D-Applied Physics,* vol. 42, Sep 21 2009.
[47] J. H. Sun and T. T. Wu, "Analyses of mode coupling in joined parallel phononic crystal waveguides," *Physical Review B,* vol. 71, May 2005.
[48] G. Wang*, et al.*, "One-dimensional phononic crystals with locally resonant structures," *Physics Letters A,* vol. 327, pp. 512-521, Jul 12 2004.
[49] J. S. Jensen, "Topology optimization problems for reflection and dissipation of elastic waves," *Journal of Sound and Vibration,* vol. 301, pp. 319-340, Mar 20 2007.
[50] J. O. Vasseur*, et al.*, "Experimental and theoretical evidence for the existence of absolute acoustic band gaps in two-dimensional solid phononic crystals," *Physical Review Letters,* vol. 86, pp. 3012-3015, Apr 2 2001.
[51] D. G. Zhao*, et al.*, "Peculiar transmission property of acoustic waves in a one-dimensional layered phononic crystal," *Physica B-Condensed Matter,* vol. 390, pp. 159-166, Mar 1 2007.
[52] N. Gomopoulos*, et al.*, "One-Dimensional Hypersonic Phononic Crystals," *Nano Letters,* vol. 10, pp. 980-984, Mar 2010.
[53] M. I. Hussein*, et al.*, "Multiobjective evolutionary optimization of periodic layered materials for desired wave dispersion characteristics," *Structural and Multidisciplinary Optimization,* vol. 31, pp. 60-75, Jan 2006.
[54] M. Saad, H. , *Elasticity, Theory, Applications, and Numerics*: Elsevier, 2005.
[55] A. Khelif*, et al.*, "Complete band gaps in two-dimensional phononic crystal slabs," *Physical Review E,* vol. 74, Oct 2006.
[56] M. I. Hussein and I. El-Kady, "Special Topic: Selected Articles from Phononics 2011: The First International Conference on Phononic Crystals, Metamaterials and Optomechanics, 29 May-2 June 2011, Santa Fe, New Mexico, USA Preface," *Aip Advances,* vol. 1, Dec 2011.
[57] R. Lammering, "Observation of Piezoelectrically Induced Lamb Wave Propagation in Thin Plates by Use of Speckle Interferometry," *Experimental Mechanics,* vol. 50, pp. 377-387, Mar 2010.
[58] J. C. Hsu and T. T. Wu, "Efficient formulation for band-structure calculations of two-dimensional phononic-crystal plates," *Physical Review B,* vol. 74, Oct 2006.
[59] V. Laude*, et al.*, "Full band gap for surface acoustic waves in a piezoelectric phononic crystal," *Physical Review E,* vol. 71, Mar 2005.
[60] X. Y. Zhang*, et al.*, "Evidence of surface acoustic wave band gaps in the phononic crystals created on thin plates," *Applied Physics Letters,* vol. 88, Jan 23 2006.

[61] R. B. Hentarski, Ignaczak, J., *Mathematical Theory of Elasticity*: Taylor & Francis, 2004.
[62] U. Basu and A. K. Chopra, "Perfectly matched layers for time-harmonic elastodynamics of unbounded domains: theory and finite-element implementation," *Computer Methods in Applied Mechanics and Engineering,* vol. 192, pp. 1337-1375, 2003.
[63] F. Ihlengurg, *Finite Element Analysis of Acoustic Scattering*: Springer Press, 1998.
[64] M. M. Sigalas and N. Garcia, "Theoretical study of three dimensional elastic band gaps with the finite-difference time-domain method," *Journal of Applied Physics,* vol. 87, pp. 3122-3125, Mar 15 2000.
[65] T. A. Laursen, *omputational Contact and Impact Mechanics: Fundamentals of Modeling Interfacial Phenomena in Nonlinear Finite Element Analysis*: Springer, 2002.
[66] A. Inc., *Theory Reference*: (ANSYS release 9.0, 2004), 2004.
[67] L. Shi*, et al.*, "Measuring thermal and thermoelectric properties of one-dimensional nanostructures using a microfabricated device (vol 125, pg 881, 2003)," *Journal of Heat Transfer-Transactions of the Asme,* vol. 125, pp. 1209-1209, Dec 2003.
[68] C. H. Yu*, et al.*, "Thermal conductance and thermopower of an individual single-wall carbon nanotube," *Nano Letters,* vol. 5, pp. 1842-1846, Sep 2005.
[69] M. T. Pettes*, et al.*, "Influence of Polymeric Residue on the Thermal Conductivity of Suspended Bilayer Graphene," *Nano Letters,* vol. 11, pp. 1195-1200, Mar 2011.
[70] S. Sadat*, et al.*, "High resolution resistive thermometry for micro/nanoscale measurements," *Review of Scientific Instruments,* vol. 83, Aug 2012.
[71] T. Tao*, et al.*, "Focused Ion-Beam Induced Deposition of Platinum," *Journal of Vacuum Science & Technology B,* vol. 8, pp. 1826-1829, Nov-Dec 1990.
[72] A. L. Moore and L. Shi, "On errors in thermal conductivity measurements of suspended and supported nanowires using micro-thermometer devices from low to high temperatures," *Measurement Science & Technology,* vol. 22, Jan 2011.
[73] A. Mavrokefalos*, et al.*, "Four-probe measurements of the in-plane thermoelectric properties of nanofilms," *Review of Scientific Instruments,* vol. 78, Mar 2007.
[74] B. L. Zink*, et al.*, "Measurement of thermal conductivity of thin films with a Si-N membrane-based microcalorimeter," *Review of Scientific Instruments,* vol. 76, Feb 2005.
[75] S. R. Choi*, et al.*, "Thermal conductivity of AlN and SiC thin films," *International Journal of Thermophysics,* vol. 27, pp. 896-905, May 2006.
[76] K. Bongsang*, et al.*, "Thermal conductivity manipulation in lithographically patterned single crystal silicon phononic crystal structures," in *Ultrasonics Symposium (IUS), 2011 IEEE International*, 2011, pp. 1308-1311.
[77] X. Zhang*, et al.*, "Thermal and electrical conductivity of a suspended platinum nanofilm," *Applied Physics Letters,* vol. 86, Apr 25 2005.
[78] R. Sultan*, et al.*, "Thermal conductivity of micromachined low-stress silicon-nitride beams from 77 to 325 K," *Journal of Applied Physics,* vol. 105, Feb 15 2009.
[79] M. Asheghi*, et al.*, "Temperature-dependent thermal conductivity of single-crystal silicon layers in SOI substrates," *Journal of Heat Transfer-Transactions of the Asme,* vol. 120, pp. 30-36, Feb 1998.
[80] Y. S. Ju and K. E. Goodson, "Phonon scattering in silicon films with thickness of order 100 nm," *Applied Physics Letters,* vol. 74, pp. 3005-3007, May 17 1999.
[81] S. Alaie*, et al.*, "Thermal conductivity and nanocrystalline structure of platinum deposited by focused ion beam," *Nanotechnology,* vol. 26, Feb 27 2015.

[82] S. Reyntjens and R. Puers, "Focused ion beam induced deposition: fabrication of three-dimensional microstructures and Young's modulus of the deposited material," *Journal of Micromechanics and Microengineering,* vol. 10, pp. 181-188, Jun 2000.
[83] G. M. Shedd*, et al.*, "Focused Ion-Beam Induced Deposition of Gold," *Applied Physics Letters,* vol. 49, pp. 1584-1586, Dec 8 1986.
[84] J. Puretz and L. W. Swanson, "Focused Ion-Beam Deposition of Pt Containing Films," *Journal of Vacuum Science & Technology B,* vol. 10, pp. 2695-2698, Nov-Dec 1992.
[85] S. Matsui*, et al.*, "Three-dimensional nanostructure fabrication by focused-ion-beam chemical vapor deposition," *Journal of Vacuum Science & Technology B,* vol. 18, pp. 3181-3184, Nov-Dec 2000.
[86] Y. Q. Fu*, et al.*, "Characterization of focused ion beam induced deposition process and parameters calibration," *Sensors and Actuators A-Physical,* vol. 88, pp. 58-66, Jan 20 2001.
[87] F. A. Stevie*, et al.*, "Application of focused ion beam lift-out specimen preparation to TEM, SEM, STEM, AES and SIMS analysis," *Surface and Interface Analysis,* vol. 31, pp. 345-351, May 2001.
[88] M. P. Manoharan and M. A. Haque, "Role of adhesion in shear strength of nanowire-substrate interfaces," *Journal of Physics D-Applied Physics,* vol. 42, p. 095304, May 7 2009.
[89] A. J. DeMarco and J. Melngailis, "Lateral growth of focused ion beam deposited platinum for stencil mask repair," *Journal of Vacuum Science & Technology B,* vol. 17, pp. 3154-3157, Nov-Dec 1999.
[90] S. Enderling*, et al.*, "Characterization of frequency tuning using focused ion beam platinum deposition," *Journal of Micromechanics and Microengineering,* vol. 17, pp. 213-219, Feb 2007.
[91] T. Tao*, et al.*, "Focused Ion-Beam Induced Deposition of Platinum for Repair Processes," *Journal of Vacuum Science & Technology B,* vol. 9, pp. 162-164, Jan-Feb 1991.
[92] D. Brunel*, et al.*, "Characterization of ion/electron beam induced deposition of electrical contacts at the sub-mu m scale," *Microelectronic Engineering,* vol. 88, pp. 1569-1572, Jul 2011.
[93] K. A. Telari*, et al.*, "Characterization of platinum films deposited by focused ion beam-assisted chemical vapor deposition," *Journal of Vacuum Science & Technology B,* vol. 20, pp. 590-595, Mar-Apr 2002.
[94] P. Kim*, et al.*, "Thermal transport measurements of individual multiwalled nanotubes," *Physical Review Letters,* vol. 87, p. 215502, Nov 19 2001.
[95] D. Y. Li*, et al.*, "Thermal conductivity of individual silicon nanowires," *Applied Physics Letters,* vol. 83, pp. 2934-2936, Oct 6 2003.
[96] T. K. Hsiao*, et al.*, "Observation of room-temperature ballistic thermal conduction persisting over 8.3 mu m SiGe nanowires," *Nature Nanotechnology,* vol. 8, pp. 534-538, Jul 2013.
[97] C. H. Yu*, et al.*, "Thermal contact resistance and thermal conductivity of a carbon nanofiber," *Journal of Heat Transfer-Transactions of the Asme,* vol. 128, pp. 234-239, Mar 2006.
[98] S. Alaie*, et al.*, "MEASUREMENT OF IN-PLANE THERMAL CONDUCTIVITY USING SUSPENDED SiNx ISLANDS," presented at the IMECE2012, Houston, Texas, USA, 2012.
[99] F. Yang and C. Dames, "Mean free path spectra as a tool to understand thermal conductivity in bulk and nanostructures," *Physical Review B,* vol. 87, Jan 31 2013.
[100] H. A. Chen*, et al.*, "Structuring a TiO2-Based Photonic Crystal Photocatalyst with Schottky Junction for Efficient Photocatalysis," *Environmental Science & Technology,* vol. 44, pp. 451-455, Jan 1 2010.
[101] J. Mayer*, et al.*, "TEM sample preparation and FIB-induced damage," *Mrs Bulletin,* vol. 32, pp. 400-407, May 2007.

[102] D. Brandon and W. D. Kaplan, *Microstructural Characterization of Maetrials*: John Wiley and Sons, 1999.
[103] X. X. Ke*, et al.*, "Low-dose patterning of platinum nanoclusters on carbon nanotubes by focused-electron-beam-induced deposition as studied by TEM," *Beilstein Journal of Nanotechnology,* vol. 4, pp. 77-86, Feb 4 2013.
[104] J. M. De Teresa*, et al.*, "Origin of the Difference in the Resistivity of As-Grown Focused-Ion- and Focused-Electron-Beam-Induced Pt Nanodeposits," *Journal of Nanomaterials,* 2009.
[105] Z. M. Liao*, et al.*, "Quantum interference effect in single Pt(Ga)/C nanowire," *Applied Physics Letters,* vol. 87, Oct 31 2005.
[106] R. M. Langford*, et al.*, "Reducing the resistivity of electron and ion beam assisted deposited Pt," *Microelectronic Engineering,* vol. 84, pp. 784-788, May-Aug 2007.
[107] M. C. Salvadori*, et al.*, "Platinum and gold thin films deposited by filtered vacuum arc: morphological and crystallographic grain sizes," *Surface & Coatings Technology,* vol. 200, pp. 2965-2969, Feb 8 2006.
[108] A. Feoktistov*, et al.*, "TEM and HREM study of 3D silicon and platinum nanoscale assemblies in dielectric opal matrix," *Semiconductor Science and Technology,* vol. 16, pp. 955-960, Dec 2001.
[109] N. W. Ashcroft and N. D. Mermin, *Solid State Physics*, 1st ed.: Brooks/Cole Cenage Learning, 1976.
[110] X. Zhang*, et al.*, "Experimental studies on thermal and electrical properties of platinum nanofilms," *Chinese Physics Letters,* vol. 23, pp. 936-938, Apr 2006.
[111] G. V. Chester and A. Thellung, "The Law of Wiedemann and Franz," *Proceedings of the Physical Society,* vol. 77, p. 1005, 1961.
[112] M. A. Atwater*, et al.*, "Accelerated growth of carbon nanofibers using physical mixtures and alloys of Pd and Co in an ethylene-hydrogen environment," *Carbon,* vol. 49, pp. 1058-1066, Apr 2011.
[113] M. A. Atwater*, et al.*, "The effect of powder sintering on the palladium-catalyzed formation of carbon nanofibers from ethylene-oxygen mixtures," *Carbon,* vol. 48, pp. 1932-1938, Jun 2010.
[114] P. Chen*, et al.*, "The complex mechanisms of ion-beam-induced deposition," *Japanese Journal of Applied Physics,* vol. 47, pp. 5123-5126, Jun 2008.
[115] S. Y. Lee*, et al.*, "Thermal conductivity measurements of single-crystalline bismuth nanowires by the four-point-probe 3-omega technique at low temperatures," *Nanotechnology,* vol. 24, May 10 2013.
[116] G. A. Slack, *CRC Handbook of Thermoelectrics*. Boca Raton, FL: CRC Press, 1995.
[117] F. Salleh*, et al.*, "Seebeck Coefficient of Ultrathin Silicon-on-Insulator Layers," *Applied Physics Express,* vol. 2, p. 071203, 2009.
[118] J. A. Martinez*, et al.*, "Enhanced thermoelectric figure of merit in SiGe alloy nanowires by boundary and hole-phonon scattering," *Journal of Applied Physics,* vol. 110, pp. 074317-6, 2011.
[119] X. H. Wang*, et al.*, "Thermoelectric properties of SiC thick films deposited by thermal plasma physical vapor deposition," *Science and Technology of Advanced Materials,* vol. 4, pp. 167-172, March 2003.
[120] D. Song and C. Gang, "Thermal conductivity of periodic microporous silicon films," *Applied Physics Letters,* vol. 84, pp. 687-689, 2 February 2004.
[121] M. N. Luckyanova*, et al.*, "Coherent Phonon Heat Conduction in Superlattices," *Science,* vol. 338, pp. 936-939, November 16, 2012 2012.

[122] Q. Hao, *et al.*, "Frequency-dependent Monte Carlo simulations of phonon transport in two-dimensional porous silicon with aligned pores," *Journal of Applied Physics,* vol. 106, pp. 114321-10, 2009.
[123] A. Jain, *et al.*, "Phonon transport in periodic silicon nanoporous films with feature sizes greater than 100 nm," *Physical Review B,* vol. 87, p. 195301, 2013.
[124] K. Bongsang, *et al.*, "Thermal conductivity manipulation in single crystal silicon via lithographycally defined phononic crystals," presented at the Micro Electro Mechanical Systems (MEMS), 2012 IEEE 25th International Conference on, 2012.
[125] I. El-Kady, *et al.*, "Phonon Manipulation with Phononic Crystals," Sandia National Laboratories2012.
[126] K. Esfarjani, *et al.*, "Heat transport in silicon from first-principles calculations," *Physical Review B,* vol. 84, p. 085204, 2011.
[127] K. T. Regner, *et al.*, "Broadband phonon mean free path contributions to thermal conductivity measured using frequency domain thermoreflectance," *Nature Communications,* vol. 4, p. 1640, 2013.
[128] E. Dechaumphai and R. Chen, "Thermal transport in phononic crystals: The role of zone folding effect," *Journal of Applied Physics,* vol. 111, pp. -, 2012.
[129] G. Chen, *Nanoscale Energy Transport and Conversion: A Parallel Treatment of Electrons, Molecules, Phonons, and Photons*. New York City, NY: Oxford University Press, 2005.
[130] Z. Zhu, *et al.*, "Assessment of the Holland model for silicon phonon-phonon relaxation times using lattice dynamics calculations," *Journal of Applied Physics,* vol. 113, pp. -, 2013.
[131] J. Zou and A. Balandin, "Phonon heat conduction in a semiconductor nanowire," *Journal of Applied Physics,* vol. 89, pp. 2932-2938, 2001.
[132] A. J. H. McGaughey, *et al.*, "Size-dependent model for thin film and nanowire thermal conductivity," *Applied Physics Letters,* vol. 99, pp. -, 2011.
[133] K. E. Goodson and Y. S. Ju, "HEAT CONDUCTION IN NOVEL ELECTRONIC FILMS," *Annual Review of Materials Science,* vol. 29, pp. 261-293, 1999.
[134] W. Liu and M. Asheghi, "Phonon–boundary scattering in ultrathin single-crystal silicon layers," *Applied Physics Letters,* vol. 84, pp. 3819-3821, 2004.
[135] W. Liu and M. Asheghi, "Thermal conduction in ultrathin pure and doped single-crystal silicon layers at high temperatures," *Journal of Applied Physics,* vol. 98, pp. -, 2005.
[136] A. Eucken, "Forschung auf dem Gebiete des Ingenieurwesens," ed Dusseldorf, Ausgabe B: VDI Verlagg m.b.h., 1932, p. 3/4 VDI Forschungsheft 353.
[137] C.-W. Nan, *et al.*, "Effective thermal conductivity of particulate composites with interfacial thermal resistance," *Journal of Applied Physics,* vol. 81, pp. 6692-6699, 1997.
[138] ANSYS® Academic Research, ANSYS, Inc., http://www.ansys.com/.
[139] M. Ziaei-Moayyed, *et al.*, "Silicon carbide phononic crystal cavities for micromechanical resonators," *2011 IEEE 24th International Conference on Micro Electro Mechanical Systems (MEMS 2011),* pp. 1377-13811381, 2011.
[140] Y. Pennec, *et al.*, "Tunable filtering and demultiplexing in phononic crystals with hollow cylinders," *Physical Review E (Statistical, Nonlinear, and Soft Matter Physics),* vol. 69, pp. 46608-1-6, April 2004.
[141] J. O. Vasseur, *et al.*, "Absolute forbidden bands and waveguiding in two-dimensional phononic crystal plates," *Physical Review B (Condensed Matter and Materials Physics),* vol. 77, pp. 085415-1-15, 15 February 2008.